# Spectroscopic Studies of Charge Dynamics in Non-Fullerene Organic Solar Cells

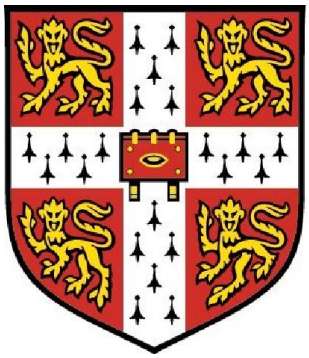

Ture Fabian Hinrichsen

Emmanuel College

University of Cambridge

This dissertation is submitted for the degree of

*Doctor of Philosophy*

September 2019

*If we knew what we were doing, it wouldn't be called research, would it?*

Often attributed to Albert Einstein

# Spectroscopic Studies of Charge Dynamics in Non-Fullerene Organic Solar Cells

Ture Fabian Hinrichsen

Emmanuel College, University of Cambridge

Organic solar cells (OSCs) are a promising technology for emission-free electricity supply. However, low power conversion efficiencies and poor device stabilities have so far prevented widespread commercial applications. Remarkable progress has been made recently by the development of non-fullerene electron acceptor materials. They benefit from good tunablity of energy levels, as well as greater thermal and photochemical stability, and remarkable power conversion efficiencies of up to 16.5 % have been achieved. Furthermore, they have shown efficient charge separation with negligible energy loss, overcoming one of the crucial limitations of fullerene based OSCs.

Here, we present a study on the charge generation, separation, and recombination dynamics of non-fullerene solar cells. We investigate the model system P3TEA:SF-$PDI_2$ via pump-probe spectroscopy and time-resolved photoluminescence spectroscopy. We find ultrafast charge generation, as well as regeneration of singlets via charge recombination. Additionally, we observe slow ($\sim 100$ ps) and thermally activated charge separation from vibrationally relaxed charge transfer exciton (CTE) states. To directly track the CTE population, we employ pump-push-probe spectroscopy. Our results suggest that singlet excitons, CTE states, and free charges form an equilibrium, with reversible interconversion between them. These systems are therefore not limited by the need to provide excess energy to overcome the Coulomb binding energy. Thus, future efforts to improve efficiencies should focus on removing energy offsets and irreversible processes, such as non-radiative recombination.

Furthermore, we study PBDB-T:ITIC, a material that was used in the first non-fullerene cell that exceeded 10 % efficiency. We find that the charge generation occurs on a $\sim 10$ ps timescale, several orders of magnitude slower than in efficient fullerene-based systems. Additionally, we identify two different pathways for non-radiative decay: triplet generation in the polymer and trap-assisted charge recombination.

# Declaration

*This dissertation is the result of my own work and includes nothing which is the outcome of work done in collaboration except as declared in the Preface and specified in the text. The use of the first person plural is strictly a matter of style.*

*It is not substantially the same as any that I have submitted, or, is being concurrently submitted for a degree or diploma or other qualification at the University of Cambridge or any other University or similar institution. I further state that no substantial part of my dissertation has already been submitted, or, is being concurrently submitted for any such degree, diploma or other qualification at the University of Cambridge or any other University or similar institution.*

*It does not exceed 60,000 words in length.*

- Ture F. Hinrichsen

# Acknowledgements

I would like to thank everyone who made the research presented in this work possible. First and foremost, I am very grateful to Dr Akshay Rao for his generous financial and non-financial support and insightful supervision. His enthusiasm for science and never-ending repertoire of ideas have been very encouraging and his efforts to create a good work environment have made a large difference to my experience. I would also like to thank Professor Sir Richard Friend for sharing his deep scientific insights and supporting our project. I owe special thanks to Dr Andreas Jakowetz and Dr Alexandre Cheminal for teaching me the secrets of non-linear optics and spectroscopy. I am also grateful to everyone else who deepened my knowledge in helpful discussions, among them Dr Christoph Schnedermann, Dr Jooyoung Sung, Dr David Paleček, Dr Matt Menke, and Dr Alexander Gillett.

Furthermore, I would like to thank my collaborators, without whom this work wouldn't have been possible. The project presented in Chapters 4 and 5 is the result of a collaboration with Dr Phillip Chow and co-workers from the Hong Kong University of Science and Technology. Samples were prepared by Dr Shangshang Chen and Professor Henry Yan. Additional measurements were conducted by Dr Phillip Chow, Dr Christopher Chan, Chao Ma, Xinhui Zou and Professor Kam Sing Wong. In particular, they measured the temperature dependent pump-probe spectra presented in Chapter 4.3.3, the photoluminescence spectra and decays presented in Chapter 4.4, and the data shown in the appendix as indicated in the figure captions. In Cambridge, Dr David Paleček, and Dr Alexander Gillett helped with the pump-push-probe measurements under my instructions. The ideas presented and the conclusions drawn from the data are the result of meetings and discussions between Professor Sir Richard Friend, Dr Phillip Chow, Dr Akshay Rao, and me.

The project presented in Chapter 6 is the result of a collaboration with the group of Dr Feng Gao from Linköping University. Samples were provided by Dr Deping Qian and Yuming Wang. The ideas presented and the conclusions drawn from the data are the result of discussions between Dr Akshay Rao and me.

I am grateful to the Winton Programme for the Physics of Sustainability, the Engineering and Physical Sciences Research Council, and the European Research Council for funding the research of this group.

Additionally, I would like to thank Dr Jooyoung Sung, Jesse Alardice, and Hope Bretscher for providing corrections to this thesis, and especially Dr Christoph Schnedermann for his advice, suggestions, and ultrafast corrections.

However, the success of a PhD does not only depend on academic support. I would therefore like to thank everyone in the Rao group for creating an atmosphere that is simultaneously fun and productive. You made me enjoy coming to the office even in the frustrating times. There are some people who deserve special mention: Thank you Hope for your support especially in the final weeks. May we continue to join forces in the fight for better science. Thank you Arya for making the office a brighter place in so many ways. Thank you Raj for the many trusting conversations. Thank you Limeng for sharing reflections on life goals amidst stormy seas. Thank you Jesse for being a kind and helpful deskmate. Thank you Jooyung and Antonis for a great trip with lots of ice cream and deep discussion over delicious pizza. Thank you Johannes and Jasmine for all the travelling experiences. Oh we all should raise a glass... Thank you Leah for your trust and your advice when I doubted everything. Thank you Sam for the great holidays. Thank you Maxim for the visit that started it all. Thank you Florian for being my coding master. Thank you Pete for the many discussions on science and policy. And thank you to everyone else who helped me out, trained me, answered my questions, laughed with me, taught me new things, or just had coffee with me on the Maxwell terrace.

And finally, I would like to express my deepest gratefulness to my parents. Thank you for sharing this journey with me and cheering from the sideline, for always having my back. You fuelled my curiosity from my early childhood on and never got tired of my questions on how the world works. You sent me out into the world and encouraged me to explore. Thank you for everything you gave me.

# List of Publications

1. **Ture F. Hinrichsen**, Deping Qian, Yuming Wang, Alexandre Cheminal, Feng Gao, and Akshay Rao. "Trap-assisted electron recombination in an efficient non-fullerene organic solar cell with low voltage loss".

   *In preparation*

2. Philip C. Y. Chow*, **Ture F. Hinrichsen***, Christopher C. S. Chan, David Paleček, Alexander Gillett, Shangshang Chen, Xinhui Zou, Chao Ma, Kam S. Wong, Richard H. Friend, He Yan, and Akshay Rao. "Long-lived and disorder-free charge transfer states enable endothermic charge separation in efficient non-fullerene organic solar cells".

   *Under review*

   * These authors contributed equally

3. Andreas C. Jakowetz, **Ture F. Hinrichsen**, Laura Ascherl, Torben Sick, Mona Calik, Florian Auras, Dana D. Medina, Richard H. Friend, Akshay Rao, and Thomas Bein. "Excited-State Dynamics in Fully Conjugated 2D Covalent Organic Frameworks" *Journal of the American Chemical Society*, 141(20):11565-11571, June 2019.

4. Limeng Ni, Uyen Huynh, Alexandre Cheminal, Tudor H. Thomas, Ravichandran Shivanna, **Ture F. Hinrichsen**, Shahab Ahmad, Aditya Sadhanala, and Akshay Rao. "Real-Time Observation of Exciton–Phonon Coupling Dynamics in Self-Assembled Hybrid Perovskite Quantum Wells" *ACS Nano*, 11(11):10834-10843, October 2017.

# Contents

# List of Figures

## LIST OF FIGURES

# Acronyms

**CTE** charge transfer exciton

**EA** electroabsorption

**EQE** external quantum efficiency

**GSB** ground state bleach

**HOMO** highest occupied molecular orbital

**LUMO** lowest unoccupied molecular orbital

**NFA** non-fullerene acceptor

**OPV** organic photovoltaics

**OSC** organic solar cell

**PCE** power conversion efficiency

**PIA** photoinduced absorption

**PL** photoluminescence

**PP** pump-probe

**PPP** pump-push-probe

**SE** stimulated emission

# Chapter 1

# Introduction

Climate change is one of the biggest challenges humanity is facing today. Urgent action is needed to limit global warming and its devastating consequences, such as severe weather events, widespread loss of agriculture, and large scale water scarcity. Simultaneously, progress in the fight against poverty and globally rising living standards continue to increase the world's energy demands. Meeting these needs while reducing greenhouse gas emission is a significant policy challenge.

Directly converting sunlight into electricity is one of the most promising technologies to achieve this goal. Solar cells now provide almost 7 % of the UK's electricity [1]. The vast majority of the cells are based on Silicon, accounting for 95 % of worldwide production in 2017 [2]. Silicon solar cells are a mature technology, with a record efficiency of 26.1 % for a non-concentrator single layer of monocrystalline Silicon [3, 4]. However, Silicon offers little mechanical and optical flexibility and requires highly-specialised production lines to ensure its quality for solar applications.

Solar cells based on organic molecules are ideally suited to address the shortcomings of silicon solar cells. These organic solar cells (OSCs) could potentially be produced at extremely low cost via roll-to-roll printing [5, 6], are light-weight, and can be produced on flexible substrates, enabling highly-flexible modules or integration into consumer products such as back-packs. Furthermore, they can be semi-transparent, allowing the use in windows or as window blinds. However, their efficiencies have long remained below 10 %, far below the efficiencies of

silicon solar cells. An additional problem is their lack of photochemical and thermal stability, which quickly reduces their efficiencies even further in operation, preventing widespread commercial application.

Within the last three years, however, remarkable progress has been made in increasing efficiencies of OSCs up to $\sim 16\,\%$ [3, 7]. This progress has mainly been driven by the development of non-fullerene acceptor molecules, as described below, and has sparked new interest into organic photovoltaics as a potentially commercially viable technology.

The fundamental component of OSCs is a blend of at least two types of molecules. When absorbing light, these molecules can transfer electrons from the 'donor' to the 'acceptor' molecules. For a long time, efficient acceptors were based on fullerene molecules, spheres formed of 60 carbon atoms. However, these molecules do not absorb large parts of the sun's spectrum and have stability issues, as mentioned above. In contrast, the recently developed non-fullerene OSCs have a tuneable absorption spectrum and exhibit improved stability [8].

Despite decades of research, the generation of photocurrent in OSCs is not fully understood. The energy of the absorbed light has to be converted to electricity efficiently before the molecules return to their initial state and release the energy as heat. To generate an electrical current, electrons have to be separated from the positively charged nuclei of the molecules. One area of debate is whether some part of the voltage of the cell has to be sacrificed to overcome the Coulomb binding that works against this separation. Another active research area is charge recombination. If electrons encounter molecules with missing electrons before being extracted at the electrical contacts, they can reform neutral molecules and thus not contribute to the current. Here we investigate these processes in non-fullerene OSC.

In this work we use absorption and emission spectroscopy, both steady-state and time-resolved, to study charge generation, separation, and recombination in non-fullerene OSCs.

In Chapter 2 we describe the theoretical background of organic semiconductors and provide a literature review of the physics of OSCs. We focus on the factors that limit solar cell efficiencies and the current debates about the charge separation mechanism. In Chapter 3 we describe the experimental methods we used in our study, with particular attention to pump-probe (PP) spectroscopy.

In Chapter 4 we describe our investigation into the charge dynamics of the model non-fullerene system P3TEA:SF-$PDI_2$. We find evidence for either a hybridisation of the singlet exciton and charge transfer exciton (CTE) states or an ultrafast formation of CTEs, and a second slower component of exciton dissociation. For charge separation we find that it occurs on a timescale of $\sim$100 ps, indicating thermally activated separation from vibrationally relaxed CTE states. This is supported by temperature dependent PP measurements. Additionally, we find that random encounters of free charges can reform singlet states, which provides further evidence that CTEs and singlet excitons are interacting closely.

In Chapter 5 we describe how we used pump-push-probe (PPP) spectroscopy to further investigate the role of CTE states in the processes described above. We begin by identifying the different components present in our PPP spectra, and find a signal that is proportional to the CTE population. With this signal we probe how the CTE population evolves after the initial excitation of the sample. We find that even after most of the initial charge separation has occurred, the proportion of bound charges decreases only slowly. This leads us to propose that the molecules repeatedly transition between singlets excitons, CTE states, and free charges, forming a thermodynamic equilibrium.

In Chapter 6 we describe our study of PBDB-T:ITIC, another highly efficient non-fullerene blend. We show that despite the high efficiency, the charge generation is slow ($\sim$ 10 ps). Furthermore, we show that triplets are generated in the polymer and that charges can recombine via trap states. Both of these processes are likely to increase non-radiative recombination, leading to losses in efficiency.

In Chapter 7 we summarise our results and discuss additional research avenues that would elucidate these questions further.

# Chapter 2

# Background

In this work we investigate the dynamics of electronic states in organic photovoltaics, in particular the generation, separation, and recombination of charges. Both the processes studied and the spectroscopic methods employed involve absorption and emission of photons and transitions between different electronic states in organic semiconductors. This chapter aims to provide an overview of the theoretical background necessary to understand the experimental results, and an overview of the relevant literature. The first section focuses on the quantum mechanical foundations of the states and transitions involved. It roughly follows the excellent book "Electronic Processes in Organic Semiconductors" [9], where a more detailed discussion can be found. The second section describes the physics of organic solar cells (OSCs), including recent developments in materials design, the factors limiting their efficiency, and current debates about the mechanisms behind charge separation and recombination.

## 2.1 Photophysics of Organic Semiconductors

### 2.1.1 Molecular Orbitals and Electronic States

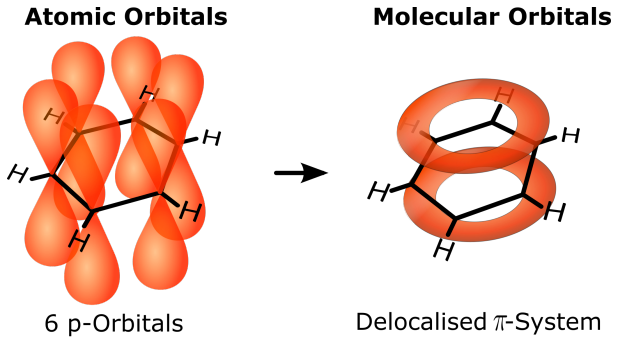


Figure 2.1: Delocalised molecular orbitals of Benzene. The atomic orbitals of the six carbon atoms form a delocalised $\pi$-molecular orbital. *Figure by Vladsinger/Wikimedia under CC BY-SA 3.0 and GFDL license [10].*

In this work we study the optical and electronic processes in organic molecules. These molecules mostly consist of electronically bound carbon atoms (C) surrounded by hydrogen (H), and often include other light atoms such as nitrogen (N), oxygen (O), florine (F), or sulphur (S). If the molecule consists of many repeating subunits it is referred to as a *polymer*. Of particular interest are *conjugated* molecules or polymers, where electrons are delocalised over multiple bonds. When describing electronic processes in these molecules it is important to distinguish between molecular orbitals and electronic states. Molecular orbitals are one-electron wavefunctions, whereas electronic states describe multi-electron configurations of molecules and account for interaction between electrons.

One way of obtaining molecular orbitals is to use atomic orbitals as a basis. These are solutions to the time-independent Schrödinger equation for a single electron surrounding a nucleus (*hydrogen-like atomic orbitals*). For organic semiconductors the $p$-orbitals of carbon atoms are especially important. Linear combinations of atomic orbitals can then be used to form molecular orbitals as approximate solutions for the multi-atom Schrödinger equation. For example, if we consider two carbon atoms with outer electrons in $p$-orbitals, a molecular orbital can be constructed by a linear combination of one orbital from each atom.

If the $p$-orbitals are orientated along the axis between the atoms, the resulting molecular orbital is referred to as a $\sigma$-orbital; if the $p$-orbitals are perpendicular to the axis, the molecular orbital is a $\pi$-orbital. This is also possible for larger molecules consisting of many atoms. One example is a benzene ring, formed by six carbon atoms. In this case the carbon atoms are pairwise connected by $\sigma$-bonds. The remaining six $p$-orbitals perpendicular to the plane of the bonds form a $\pi$-system of electrons that are delocalised over the whole ring (Figure 2.1). These delocalised $\pi$ electrons are responsible for the remarkable optical and electrical properties of organic semiconductors, and molecules containing them are referred to as *conjugated systems*.

Following the calculation of molecular orbitals, the electrons from the initial atoms are distributed over the molecular orbitals with the lowest energy. Of particular importance for optical transitions and electronic transport are the highest occupied molecular orbital (HOMO) and the lowest unoccupied molecular orbital (LUMO). The theoretically calculated energies of these molecular orbitals can be approximately related to experimentally accessible parameters as follows: The energy of the HOMO represents the energy needed to remove an electron from the molecule, the *ionisation potential*. The energy of the LUMO represents the energy gained when adding an electron to the molecule, the *electron affinity*.

To describe electronic processes in organic semiconductors it is often essential to move beyond this description of the energy levels available for electrons in a molecule, and consider the overall energy of a molecule when its electrons are in a particular configuration. For example, exciting one electron from the HOMO to the LUMO can be described as moving the molecule from its ground state to an excited state. However, the energy of this excited state is lower than the energy difference between HOMO and LUMO. This is due to the reorganisation of the molecule in this new electronic configuration, with an electron missing in the HOMO orbital compared to the ground state. It is useful to treat these missing electrons as positive quasi-particles: *holes*. The lowering of the excited state energy can than be described in terms of a Coulomb attraction between the electron in the LUMO and the hole in the HOMO. This coulombically bound electron-hole pair can in turn be described as a quasi-particle, the *exciton*, which

is useful for example for describing transport phenomena in devices. The difference between the HOMO-LUMO gap and the energy of the lowest excited state is referred to as the *exciton binding energy*. If electrons and holes are not on the same molecule, for example following charge transfer as discussed in Section 2.2.3, they are sometimes referred to as *polarons*. This term describes not only the individual electron or hole, but includes the Coulomb interaction with neighbouring molecules and the resulting reorganisation.

Another important interaction between electrons that is not considered in the simple picture of molecular orbitals is the effect of the electron spin. When calculating the spin wavefunction for the two particle system, four eigenstates to the corresponding quantum mechanical operators are found: One state where the electron in the HOMO and the hole in the LUMO have antiparallel spin, resulting in an overall spin of zero; and three states where electron and hole have parallel spin, resulting in an overall spin of $\hbar$ (usually stated as 'spin 1' in units of $\hbar$). The three configurations with parallel spin are referred to as a *triplet* state, in contrast to the *singlet* state with antiparallel spin. In organic semiconductors the energy of the triplet state is lower than the energy of the singlet state, due to the exchange interaction. This energy difference, the exchange energy, has experimentally been found to be close to 0.7 eV in many conjugated polymers [11]. The behaviour of triplet states in organic semiconductors can differ substantially from singlet states [12]. As discussed in Section 2.2.5, controlling their energetics and dynamics could be crucial for the development of efficient OSCs.

### 2.1.2 Vibrational States and Potential Energy Surfaces

Thus far we have only considered the energetic states of electrons, without explicitly considering movement of nuclei in the molecules. This is based on the *Born-Oppenheimer approximation* that electrons move much faster than nuclei due to their vastly different mass. A common approach to calculate energies of electronic states is to fix the distance between nuclei and then calculate the energy configuration of the electrons. This can be repeated for each internuclear distance $r$. For two atoms this leads to the Morse potential (Figure 2.2), which has a fixed

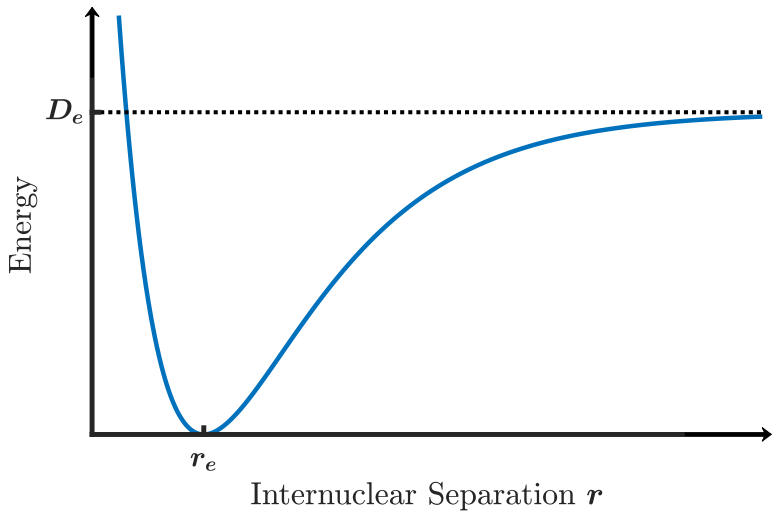


Figure 2.2: The Morse potential: potential energy of two atoms depending on the separation of their nuclei. It increases exponentially for distances smaller than the equilibrium internuclear separation $r_e$, and asymptotically approaches the dissociation energy $D_e$ for large separations.

value at a large separation ($r \to \infty$), increases exponentially as the nuclei approach each other ($r \to 0$), and has a minimum at an equilibrium distance where Coulomb attraction and repulsion of electrons and nuclei are balanced. Near the equilibrium distance the Morse potential can be approximated by the harmonic oscillator potential. A quantum mechanical treatment of these oscillations in the internuclear distance leads to a set of vibrational states that are equidistant in energy, with corresponding vibrational wavefunctions.

Molecules consisting of multiple atoms can be treated as coupled oscillators. Their vibrations can than be simplified to normal modes, which are collective movements such as a stretching of carbon bonds along the polymer backbone or breathing modes of phenyl rings (a group of carbon atoms forming a hexagon). The positions of the nuclei are then considered as one point in the multidimensional coordinate system of the normal mode coordinates $Q_i$. To obtain the potential energy surface in this coordinate system, the lowest energy electronic wavefunction can be calculated for each nuclear position. In practice it is often sufficient to consider only the normal modes that are most relevant for the states and transitions of interest, and the potential energy is displayed as a curve along

one of these normal mode coordinates. Since these curves depend on the electron wavefunctions they are different for each electronic state. In the simplest case the energy curve of the first excited states is shifted upwards and towards a larger $Q$, reflecting the higher electronic energy and an increased average nuclear distance.

### 2.1.3 Radiative Transitions

One of the most important ways molecules interact with the environment is through absorption or emission of light. Understanding these processes is not only crucial for utilising organic molecules in optoelectronic devices such as solar cells or light emitting diodes, but also for using spectroscopic techniques to study these molecules. These radiative transitions can be treated by quantum mechanical perturbation theory. Here, the interaction of the molecular states with photons is considered by adding a new perturbing Hamiltonian $\hat{H}'$ to the original Hamiltonian of the molecular system. This allows to treat the effect of photon interactions as a small correction to the molecular states calculated previously. It is then possible to derive an expression for the transition rate $k_{if}$ between an intial state with the wavefunction $\Psi_i$ and a final state with the wavefunction $\Psi_f$, which is termed *Femi's golden rule* [9]:

$$k_{if} = \frac{2\pi}{\hbar} \left| \langle \Psi_f | \, \hat{H}' \, | \Psi_i \rangle \right|^2 \rho_f, \tag{2.1}$$

where $\rho_f$ is the density of the final states. In the case of radiative transitions, the appropriate pertubation Hamiltonian is the electric dipole operator $\hat{H} = e\hat{\boldsymbol{r}}$, with the elementary charge $e$ and the position operator $\hat{\boldsymbol{r}}$. We consider three components of the molecular wavefunctions: an electronic wavefunction that depends on the spatial locations of the electrons $\mathbf{r}$ and nuclei $\mathbf{R}$, $\Psi_{el} = \Psi_{el}(\mathbf{r}, \mathbf{R})$; a spin wavefunction that depends on the spins $\alpha, \beta$ of the electrons, $\Psi_{spin} = \Psi_{spin}(\alpha, \beta)$; and a vibrational wavefunction $\Psi_{vib} = \Psi_{vib}(\mathbf{R})$. This yields

$$k_{if} = \frac{2\pi}{\hbar} \left| \langle \Psi_{el,f} \Psi_{spin,f} \Psi_{vib,f} | \, e\hat{\boldsymbol{r}} \, | \Psi_{el,i} \Psi_{spin,i} \Psi_{vib,i} \rangle \right|^2 \rho_f \tag{2.2}$$

$$= \frac{2\pi}{\hbar} \left| \langle \Psi_{el,f} | \, e\hat{\boldsymbol{r}} \, | \Psi_{el,i} \rangle \right|^2 \left| \langle \Psi_{spin,f} | \, | \Psi_{spin,i} \rangle \right|^2 \left| \langle \Psi_{vib,f} | \, | \Psi_{vib,i} \rangle \right|^2 \rho_f. \tag{2.3}$$

The last step is possible since the vibrational and the spin wavefunctions do not depend on $\mathbf{r}$. Approximating the wavefunction as a product of it's three component neglects interactions between them, which is based on the Born-Oppenheimer approximation in the case of the electronic and the vibrational wavefunction. Under these assumptions, radiative transition rates are proportional to a product of three factors (equation 2.3): an electronic, a vibrational, and a spin factor. As we will discuss in detail in the following, these factors give rise to a set of selection rules governing the transition probabilities.

**The electronic factor:** There are three considerations when analysing the integral $|\langle\Psi_{el,f}|\, e\hat{\boldsymbol{r}}\, |\Psi_{el,i}\rangle|$, also referred to as the *transition dipole moment*: Firstly, the dipole operator has odd parity (its sign is flipped by spacial inversion). If the initial and final states have the same inversion symmetry, the integral therefore evaluates to zero. Since the ground state wavefunction of most molecules is symmetric (even parity, *gerade*), only states of odd parity (*ungerade*) are accessible by the absorption of photons in the ground state. Transitions between states of the same parity are said to be *symmetry forbidden*. Excited states that are not accessible via radiative transitions are sometimes referred to as *dark states*. Secondly, the integral value increases with increasing overlap of initial and final wavefunctions. This increases the probability of radiative transitions between states on the same molecule as compared to transitions involving multiple molecules, for example the charge transfer exciton (CTE) states described in Section 2.2.3. Thirdly, the integral increases when the wavefunctions extend over a large area. This leads to a stronger absorption for more delocalised states, for example when adding repeat units in conjugated molecules.

**The vibrational factor:** The square of the integral $|\langle\Psi_{vib,f}\,|\,\Psi_{vib,i}\rangle|$ is referred to as the *Franck-Condon factor*, $F$. It shows that the transition probability depends on the overlap between the vibrational wavefunctions of initial and excited state. This is often called the *Franck-Condon principle* and is schematically shown in Figure 2.3a. Following an excitation into a higher vibrational state of the first electronic excited state, the molecule thermally relaxes to the lowest vibrational state on a timescale of one picosecond. The inverse of the radiative transition rate, referred to as the *radiative lifetime*, is typically of the order of

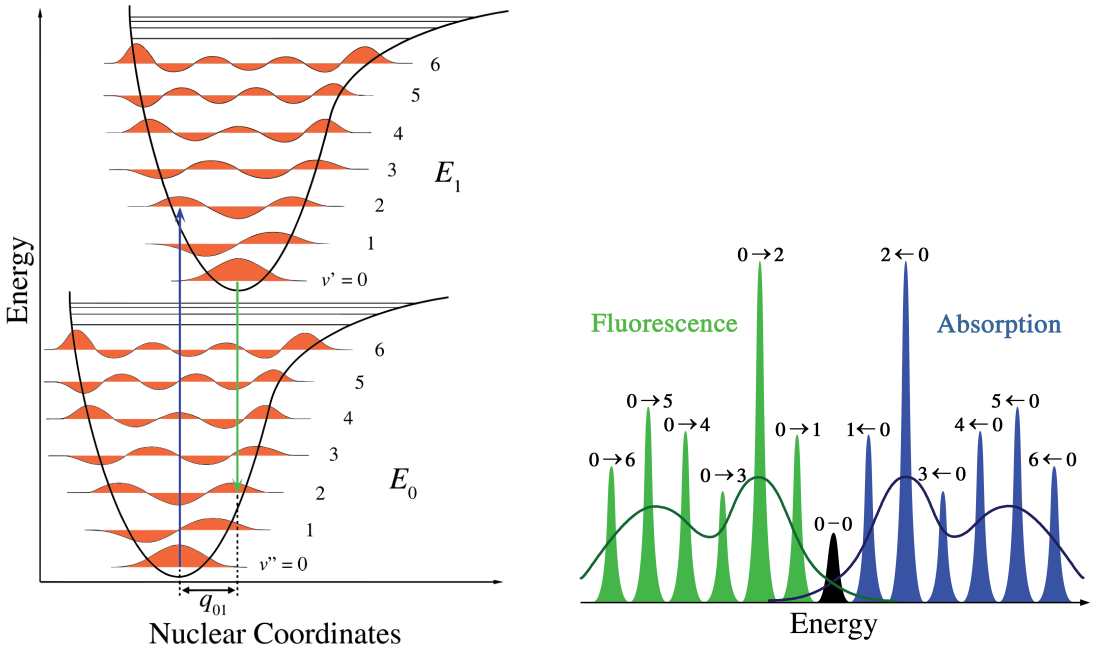


(a) Radiative Transitions

(b) Resulting Spectra

Figure 2.3: Illustration of the Frank-Condon principle: Energy diagram (a), where radiative transitions are represented as vertical arrows since nuclei are assumed to be stationary on these timescales. The transition rate depends on the overlap of the vibrational wavefunctions shown in orange, and transitions occur from the lowest vibrational energy level. This explains the shape of the emission and absorption spectra (b). In case of molecular crystals the spectral peaks are broadened (black lines in (b)). *Figures by Mark Somoza under CC-BY-SA_2.5 and GFDL license [13, 14].*

one nanosecond. Thus, the emission of photons usually occurs from the lowest vibrational state of the electronic state involved.

**The spin factor:** The integral $|\langle \Psi_{spin,f} \mid \Psi_{spin,i} \rangle|$ is zero for different spins of the initial and final state, and one for identical spins. Therefore, transitions between states with different spin are *spin forbidden*. Transitions between singlet and triplet states are only possible if the the triplet state is mixed with singlet states, or vice-versa. This is caused by *spin-orbit coupling*, an interaction of the orbital angular momentum and the spin angular momentum of the electronic state. The strength of the spin-orbit coupling depends on the atomic number, so that these

transitions have high rates only in molecules that contain heavy atoms. Emission of photons due to a transition from a singlet state to the ground state is referred to as *fluorescence*, and from a triplet state as *phosphorescence*.

### 2.1.4 Non-radiative Transitions

Molecules can change between states not only via exchange of photons, but also through non-radiative transitions. In the previous section we have already described *vibrational relaxation*, where molecules relax into the lowest vibrational state without changing their electronic state. The excess energy is dissipated into the surrounding molecules as heat. Since this often leads to a population of excited states that follows the temperature dependent Maxwell-Boltzmann distribution, vibrational relaxation is often referred to as *thermalisation*.

Another type of non-radiative transition can occur between vibrational levels of similar energies belonging to different electronic states. If both electronics states involved have the same spin, this is referred to as *internal conversion* (Figure 2.4a), if the spin changes during the transition as *intersystem crossing* (Figure 2.4b). The corresponding transition rates can again be calculated with perturbation theory (Equation 2.1), with the nuclear kinetic energy operator $\partial/\partial Q$ as the perturbing Hamiltonian [9]:

$$k_{if} = \frac{2\pi}{\hbar} \left|\langle \Psi_{el,f}\Psi_{spin,f}\Psi_{vib,f}| \, \partial/\partial Q \, |\Psi_{el,i}\Psi_{spin,i}\Psi_{vib,i}\rangle\right|^2 \rho_f. \tag{2.4}$$

This can be evaluated by first integrating over the electronic and spin wave functions, and then over the vibrational wavefunctions to yield

$$k_{if} = \frac{2\pi}{\hbar}\rho_f J^2 F \tag{2.5}$$

with

$$J = \langle \Psi_{el,f}\Psi_{spin,f}| \, \partial/\partial Q \, |\Psi_{el,i}\Psi_{spin,i}\rangle \tag{2.6}$$

and the Franck-Condon factor $F = \left|\langle \Psi_{vib,f} \,|\, \Psi_{vib,i}\rangle\right|^2$. The Franck-Condon factor, and in turn the non-radiative transition rate, has an exponential dependence on

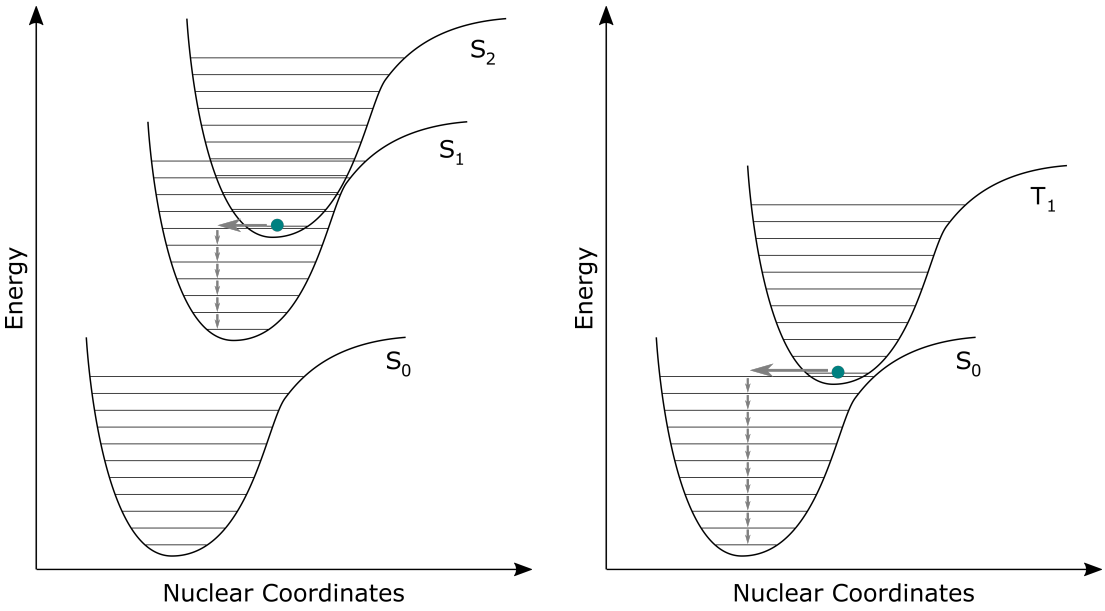


(a) Internal Conversion (b) Intersystem Crossing

Figure 2.4: Illustration of non-radiative transitions, followed by vibrational relaxation: (a) Internal conversion between states of the same spin. (b) Intersystem crossing between states of a different spin.

the energy difference $\Delta E$ between the initial and the final state [15, 16, 17]:

$$k_{if} \propto \exp\left(-\gamma \frac{\Delta E}{\hbar \omega_M}\right), \tag{2.7}$$

where $\gamma$ contains structural information about the molecule and $\omega_M$ is the frequency of the highest energy vibration of the final state. This *energy gap law* is in good agreement with experimental data [18] and often referred to when discussing non-radiative processes in OSCs.

### 2.1.5 Transitions Between Molecules

Until now we have only considered transitions between states of the same molecule. However, if molecules are in close proximity they can exchange energy via different coupling interactions. This can again be treated with perturbation theory, where the perturbing Hamiltonian describes the electrostatic interaction between

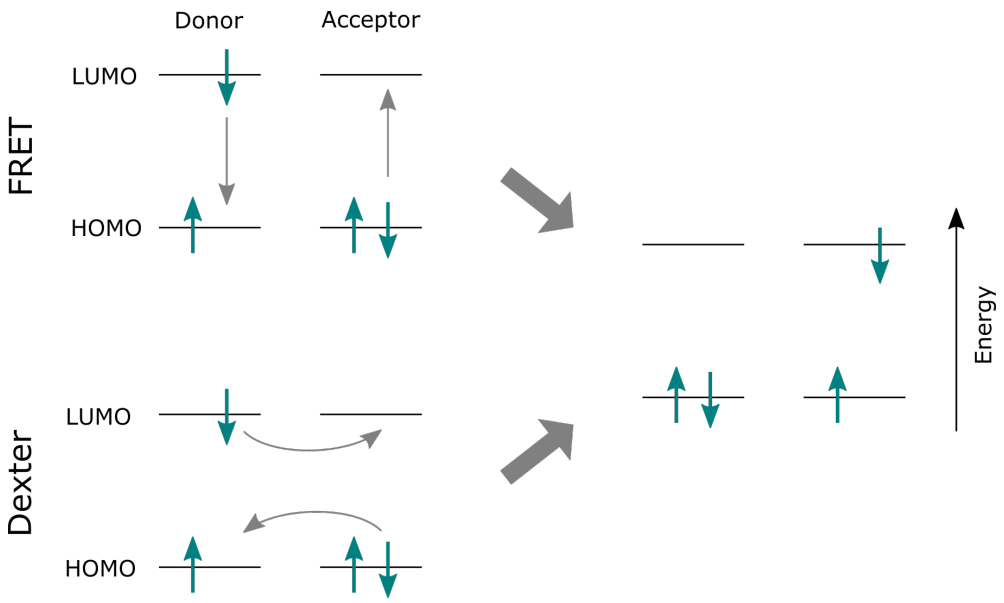


Figure 2.5: Energy transfer between molecules: In Förster resonant energy transfer (FRET, top left) energy is transferred between molecules via Coulomb coupling. In exchange mediated Dexter-type energy transfer, electrons move between the molecules.

the molecules. The initial and final state wavefunctions comprise an electron of the energy donor and and electron of the energy acceptor, and include both electron and spin wavefunction. Calculating the electronic interaction energy with this wavefunction leads to two terms: In one term the electrons change between molecules, which is referred to as *Dexter electron transfer*. In the other term the electron on the donor returns to the ground state, while the electron on the acceptor is elevated to the excited state. This is termed *Förster resonant energy transfer* (FRET). The overall transfer rate can be expressed as [19]

$$k_{ET} = \frac{2\pi}{\hbar} |V|^2 \int_0^\infty I_D(\lambda)\, \epsilon_A(\lambda) \mathrm{d}\lambda, \tag{2.8}$$

where $V = V_{\mathrm{FRET}} + V_{\mathrm{Dexter}}$ is the electronic coupling between them, $I_D(\lambda)$ is the normalised emission of the donor, and $\epsilon_A(\lambda)$ is the normalised absorption of the acceptor. Thus, the energy transfer rate is proportional to the overlap between the donor emission and the acceptor absorption. Additionally, FRET can only occur between states with the same spin.

When calculating $V_{FRET}$, the electrostatic interaction between the molecules can be simplified by considering only the dipole-dipole interaction. This approximation is valid when the intermolecular distance is much larger than their sizes. In this case the coupling can be expressed as

$$V_{\mathrm{FRET}} \propto \frac{|\mu_D||\mu_A|}{r^3}\kappa \propto r^{-3}, \tag{2.9}$$

where $\mu_D$ and $\mu_A$ are the transition dipole moments of donor and acceptor, respectively, $r$ is the distance between the molecules, and $\kappa$ is a factor that is defined by the relative orientation between the dipoles ($\kappa = 2$ for collinear, 1 for parallel, and 0 for perpendicular dipoles).

For Dexter transfer, the coupling strength depends on the overlap of the molecular orbitals of the states involved. It reduces exponentially with increasing distance between the molecules

$$V_{\mathrm{Dexter}} \propto e^{-r}. \tag{2.10}$$

Thus, Dexter transfer is efficient only at small intermolecular distances compared to FRET and typically dominates for $r < 1\,\mathrm{nm}$ [9].

## 2.2 The Physics of Organic Photovoltaics

### 2.2.1 Introduction to OSCs and Non-Fullerene Acceptors

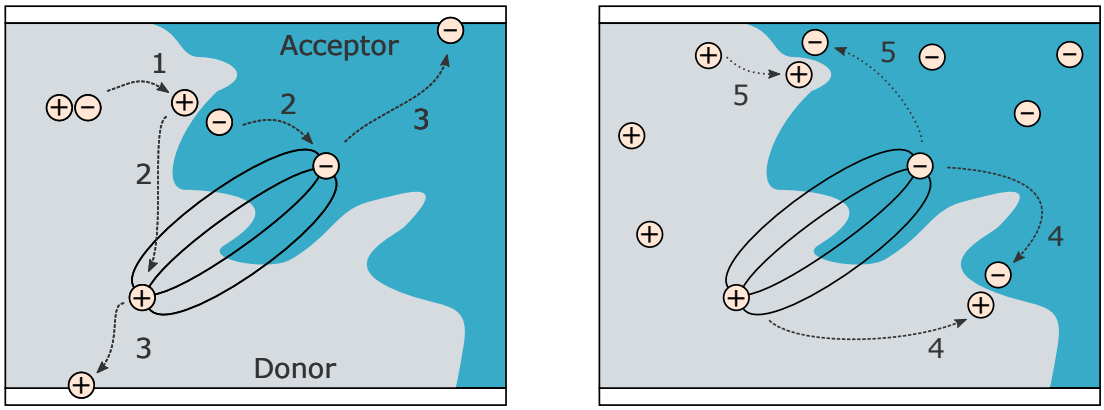


Figure 2.6: Scheme of an organic solar cell and the processes involved in the generation of photocurrent. 1: Charge generation (singlet exciton → CTE), 2: Charge separation (CTE → free charges), 3: Charge extraction, 4: Geminate recombination, 5: Non-geminate Recombination.

The previous sections provided an general overview of the energetic states of molecules and possible transitions between them. Now we will focus on processes that are specifically relevant to photovoltaics. A typical OSC consists of several layers: an active layer where charges are generated, electrodes to extract these charges, and additional layers to reduce losses at interfaces. The active layer is typically formed by an intertwined mixture of two types of molecules or polymers with different electron affinities. This is referred to as a *bulk heterojunction* of electron donor (smaller electron affinity) and electron acceptor (larger electron affinity) molecules. Generating a photocurrent in such devices requires multiple steps: Absorption of light to generate excitons, transport of excitons to an interface between phases of different molecules, dissociation of excitons into electrons and holes located on different molecules (CTE state), separation of these coulombically bound charges into free charges, transport of charges to the electrodes, and extraction of charges (Figure 2.6). These steps have to occur before excited states recombine and transition back to the ground state. An overview of these processes can be found in References [20] and [21].

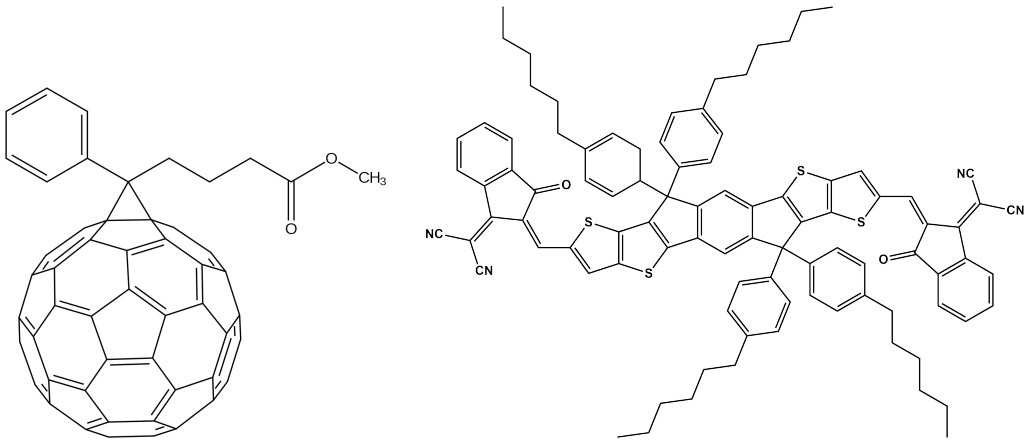


(a) Fullerene Acceptor PCBM (b) Non-fullerene Acceptor ITIC

Figure 2.7: Molecular structure of acceptor molecules in OSCs. (a) PCBM, a typical fullerene-based acceptor. (b) ITIC, one of many non-fullerene acceptors used in efficient devices.

For many years, the most efficient OSCs used fullerene derivatives as acceptor materials, such as PCBM (Figure 2.7a). Blends of these molecules with suitable donor polymers or small molecules were able to achieve very efficient charge separation and transport. However, fullerene acceptors suffer from a range of disadvantages: First, their absorption spectrum is mostly in the UV wavelength region, making them transparent for large parts of the solar spectrum. Second, they are not stable under changes in temperature or photochemical excitation. Third, their energy levels are difficult to tune. Therefore, significant efforts have been devoted to finding alternative acceptor materials [22, 23, 24, 25, 26]. The first non-fullerene OSC with an efficiency above state-of-the-art fullerene cells used ITIC as an acceptor (Figure 2.7b). In recent years a large variety of non-fullerene acceptor (NFA) molecules have been developed, achieving remarkably high power conversion efficiencies (PCE) of 15.7 % (14.9 % certified) [27] for single junction OSCs (one active layer) and 17.3 % for a tandem cell (two active layers) [28]. In this work we study the charge dynamics in several different non-fullerene OSCs.

### 2.2.2 Limits of Solar Cell Efficiencies

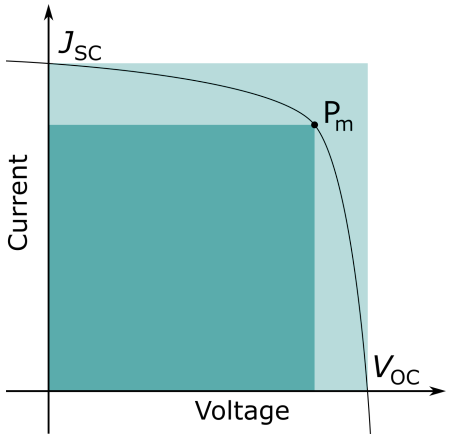


Figure 2.8: Current-voltage characteristics of a solar cell, with open circuit voltage $V_{OC}$, short-circuit current $J_{SC}$ and the maximum power point $P_m$. The fill factor $FF = P_m/(V_{OC}\ J_{SC})$ is the ratio between the light and the dark rectangle.

Solar cell devices can be characterised by their current-voltage characteristics (Figure 2.8). Important parameters for solar cell devices are the *open circuit voltage* $V_{OC}$, the *short-circuit current* $J_{SC}$, and the *fill factor* $FF = P_m/(V_{OC}J_{SC})$, where $P_m$ is the point with the largest product of current and voltage. The current extracted at a solar cell relates to the internal quantum efficiency of the device, the number of electrons created per absorbed photon. The voltage depends on the potential energy difference between electron and hole when they are extracted and relates to the initial difference between HOMO and LUMO level as well as any energy losses during charge generation, separation, and extraction. In the following we will discuss the factors affecting solar cell efficiencies.

The thermodynamic efficiency limit of solar cells is referred to as the *detailed balance limit* or *Schockley-Queisser limit* [29, 30]. This calculation approximates the solar spectrum as the black body spectrum at 6000 K, and makes two additional assumptions: each photon above the absorption edge of the material (often referred to as the *optical bandgap* $E_g$) is converted into an electron-hole pair which contributes to the photocurrent, and no non-radiative recombination of electron-hole pairs to the ground state occurs. The losses in an ideal solar cell can be separated into four contributions [31]:

**Imperfect absorption loss:** Photons with an energy below the absorption onset of the solar cell do not generate excitons. This reduces the photocurrent.

**Carnot loss:** To calculate the Carnot loss, the solar cell is considered as an ideal heat engine, with the sun as the hot reservoir (temperature $T_S$), and the solar cell as the cold reservoir (temperature $T_C$). Thus, the maximum PCE is reduced by the Carnot factor $(1 - T_C/T_S)$.

**Thermalisation loss:** Photons with an energy above the absorption edge generate 'hot excitons' which quickly thermalise. The difference between the photon energy and the bandgap energy is dissipated as heat. This reduces the photovoltage.

**Étendue expansion loss:** The solid angle of the photons emitted by the solar cell is larger than the solid angle of the incident photons from the sun. This represents an increase in photon entropy, which reduces the PCE further.

The Schockley-Queisser limit describes an idealised solar cell, whereas additional losses occur in real devices. In this study we focus on two of these losses:

**Losses due to non-radiative recombination:** If excited states recombine to the ground state via non-radiative transitions followed by vibrational relaxation, their energy is dissipated as heat. The voltage loss due to non-radiative recombination can be expressed in terms of the external quantum efficiency of the solar cell in an electroluminescence measurement ($\mathrm{EQE_{EL}}$, photons emitted per electron injected) [15, 32, 33, 34]:

$$\Delta V_{\mathrm{OC,nrad}} = k_B\, T \ln(\mathrm{EQE_{EL}}), \tag{2.11}$$

where $k_B$ is the Boltzmann constant and $T$ the temperature. Benduhn et al. found that non-radiative losses follow the energy gap law (Equation 2.7) and concluded that they are caused by the non-radiative transitions that are intrinsic to organic molecules [35]. Thus, they argued that these losses can not be avoided in OSCs. This would reduce the maximum achievable PCE and blue-shift the optimal bandgap. Others have also stressed the importance of reducing non-radiative recombination [36, 37], and Menke at al. suggested that measuring the

quenching of photoemission to identify promising materials for OSCs favours the development of materials with large non-radiative losses [38].

**Losses during charge generation and transport:** It has been proposed that a *driving energy* is needed to overcome the Coulomb binding energy of electrons and holes. This would require separated charges to have a lower energy level than the initially excited exciton, and therefore constitute a voltage loss. We will cover this debate in more detail in the next section. Additional losses can occur during the transport of charges away from the interface and towards the electrodes. For example, aggregated phases with lower energy levels have been suggested to drive charges away from the interface and prevent recombination [39].

### 2.2.3 Charge Generation, Separation, and the Role of Charge Transfer States

In inorganic solar cells the exciton binding energy is of the order of the thermal energy at room temperature. Similarly, for organic-inorganic perovskite solar cells a recent study found binding energies of only a few meV [40]. Thus, once generated these charges separate easily. In contrast, excitons in organic solar cells are strongly bound, with binding energies exceeding 0.5 eV [41, 20]. As mentioned above, there has been substantial debate on the need for excess energy as a driving force for charge separation. A closely related question is whether strongly bound CTE states are formed before charges separate. In this section we will describe the states involved in charge generation and separation and how their energetics affect solar cell efficiencies, which has been the subject of multiple review articles over the past decade [21, 42, 43, 44, 38].

From a molecular orbital perspective, charge transfer involves a transfer of an electron from the LUMO of the donor to the LUMO of the acceptor (Figure 2.9). If instead the acceptor is the initially excited molecule, hole transfer can occur. In this case an electron is transferred from the HOMO of the donor to the HOMO of the acceptor. If electron and hole, now on separate molecules, remain close together, they are still coulombically bound. The internal energy of the vibrationally relaxed CTE state is therefore lower than the energy of free charges (Figure 2.10). Typical CTE binding energies are 200 - 300 meV [20, 45, 46, 47].

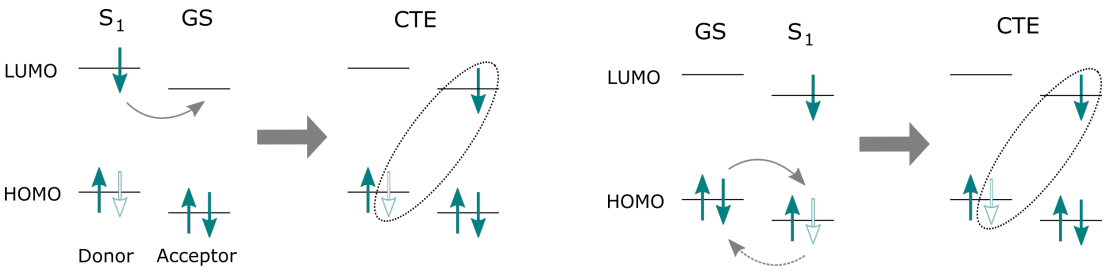


(a) Electron Transfer (b) Hole Transfer

Figure 2.9: Charge generation in the molecular orbital picture. (a) Electron transfer, with the electron transitioning from the LUMO of the donor to the LUMO of the acceptor. The dotted circle symbolises the Coulomb binding between the hole on the donor and and the electron on the acceptor. (b) Hole transfer, with the electron transitioning from the HOMO of the donor to the HOMO of the acceptor. This corresponds to a hole being transferred from the acceptor to the donor. Both processes form the same CTE state across the interface.

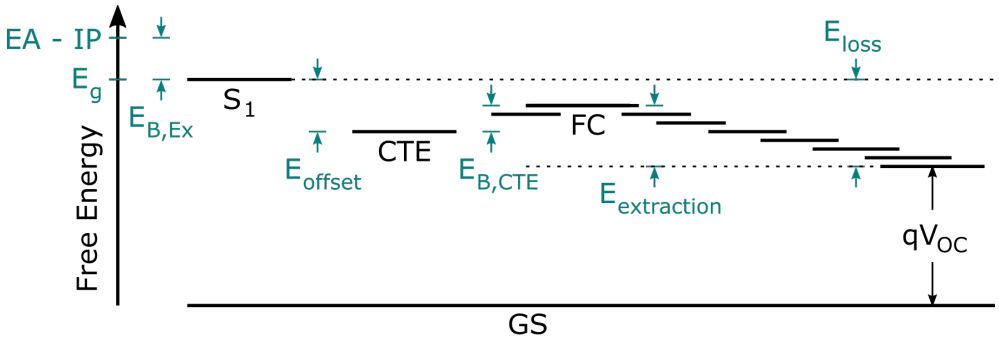


Figure 2.10: Energy level picture of charge generation and separation. The graph shows the difference of electron affinity (EA) and ionisation potential (IP) of the donor (roughly corresponding to the difference between HOMO and LUMO levels); the energy of the donor singlet exciton ($S_1$), the CTE state, and free charges (FC); and the potential energy at the electrodes ($qV_{OC}$). Also shown are the Coulomb binding energies of the donor exciton ($E_{B,Ex}$), and CTE ($E_{B,CTE}$); the driving energy for charge separation ($E_{offset}$), defined as the difference between singlet and CTE energies and roughly corresponding to the HOMO offset of donor and acceptor for hole transfer; the loss of free energy during the extraction of charges ($E_{extraction}$), with contributions from a loss in potential energy and an increase in entropy; and the total energy loss $E_{loss} = E_g - qV_{OC}$.

To overcome this binding energy, it has been proposed that excess energy is required. In this model, charge separation at least partially occurs from vibrationally excited CTE states, referred to as *hot CT states*. Since vibrational relaxation occurs within approximately one picosecond, charge separation must occur on a faster timescale to be efficient [48]. Ultrafast charge separation has indeed been observed in fullerene-based OSCs [49]. Thus, efficient solar cells have been thought to require a substantial energy difference between their singlet state and CTE state, referred to as the *offset energy* ($E_{\text{offset}}$ in Figure 2.10) or *driving energy*. Several experimental studies have supported this model, finding links between the driving energy and charge separation yield via optical measurements [50, 51], and purely electrical measurements on a device [52]. Additionally, exciting higher energy singlet states has been found to increase the generation of free charges [53].

However, several studies have cast doubt on the need for excess energy as a driving force of charge separation. Vandewal et al. found no effect of the excitation energy on the current-voltage curve of several fullerene based OSCs, with efficient charge generation even when directly exciting the vibrationally relaxed CTE state [54]. Bässler et al. have argued that the Coulomb binding energy of the CTE can be reduced by electrostatic screening and delocalisation of charges, enabling separation from thermally relaxed CTE states [55]. The importance of delocalisation and the crystallinity of the acceptor phase for efficient separation has been suggested by others as well [49, 56, 57, 58]. It has also been suggested that charge separation is entropy-driven. The density of states is drastically increased for free charges as compared to bound charges at the interface, leading to an increase in entropy. This lowers the free energy of separated charges, making charge separation energetically favourable [59]. However, there would still be an activation energy for the charge separation process. This has been studied by Arndt et al. [60], who measured photon emission from CTE states and found that the proportion of these states who do not separate into free charges depends on the sample temperature. A similar result has been reported recently for non-fullerene acceptor materials [61], where pump-push-photocurrent measurements were used to extract an activation energy for charge separation of 100 meV.

Despite these indications that excess energy is not a necessary condition for efficient charge separation, for many years there had been no OSCs with external quantum efficiencies (EQE) above 50% and energy losses $E_{\text{loss}}$ below 0.6 eV [62]. Here, the energy loss is defined as the difference between the singlet energy of the lower bandgap material, as determined by the absorption onset, and the open circuit voltage of the solar cell multiplied by the elementary charge (Figure 2.10):

$$E_{\text{loss}} = E_g - eV_{\text{OC}}.$$

However, recent materials have begun to break this trend. Ran et al. reported PIPCP:$PC_{61}BM$ devices with an energy loss of 0.52 eV, and an EQE of about 60%. Since the emergence of non-fullerene acceptors, several additional materials with high PCE and low voltage losses have been developed [63, 64, 65, 66, 67, 37]. These materials often have a negligible offset between the singlet energy of either donor or acceptor and the CTE energy, thus providing no significant driving force for charge separation. This leads to the question of whether there are properties in non-fullerene acceptors that allow them to separate charges more easily than their fullerene-based counterparts. In this work we aim to provide further insights regarding this question.

An additional interesting aspect of the negligible offset between CTE and singlet exciton states is potential hybridisation between them. If these states are almost isoenergetic, how do they interact with each other? Three studies have considered the electronic state at the interface as a mixture of the locally excited exciton and the CTE state [68, 69, 70]. Since the formation of a CTE state results in a change in dipole moment [71], the CTE character of the interfacial state can be determined via the polarisation anisotropy between absorption and emission [69, 70]. A recent study proposed that this hybridisation can reduce non-radiative voltage losses [72]. Furthermore, Chen et al. suggested that the effect of hybridisation is important even in materials with large offsets between CTE and singlet exctiton [73].

### 2.2.4 Charge Recombination

To contribute to photocurrent, charges have to be extracted before they recombine to the ground state. There are two different ways charges can recombine: *geminate recombination*, where the same electron and hole that formed the initial CTE or singlet exciton recombine, and *non-geminate recombination*, where random encounters of separated charges form new electron-hole pairs. They can be experimentally distinguished through their fluence dependence [52, 39]: The probability of random encounters for non-geminate recombination depends on the square of the charge density, while the rate of geminate recombination depends linearly on their density. Thus, kinetics of non-geminate recombination normalised to the initial density show a faster decay at higher excitation densities, while geminate recombination kinetics are fluence-independent. Strong geminate recombination is a result of inefficient charge separation [52, 39], which reduces the open circuit current of the device. Strong non-geminate recombination has been shown to predominantly effect the fill factor [74] and open circuit voltage [46].

A standard model of non-geminate recombination is the Langevin theory [75], which describes recombination in a homogenoeus medium and assumes that every electron that encounters a hole recombines. However, observed recombination rates $k$ in efficient OSCs are typically lower than the ones predicted by Langevin theory ($k_{\mathrm{LAN}}$) [76], which is often express in terms of the *Langevin reduction factor* $\zeta = k/k_{\mathrm{LAN}}$. Various alternative models of non-geminate recombination have been developed that include the influence of energetic disorder, interfacial states, or different mobilities of electrons and holes [77, 78, 79]. For example, the interface morphology and size of the donor and acceptor domains have been shown to influence recombination rates in Monte-Carlo simulations [80], and aggregation can lower the optical bandgap and drive charges away from the interface, thus suppressing recombination [39].

An additional effect that could reduce the apparent non-geminate recombination rate is the formation of an equilibrium between CTE states and separated charges [81, 46]. In this model, CTE states formed by encounters of free charges

can separate again, and only a small proportion is lost via non-radiative recombination to the ground state. Thus, most CTE reformation events do not reduce the density of charges, contrary to the assumptions in Langevin theory.

### 2.2.5 Triplet Formation

As we have discussed above, encounters of charges only reduce the PCE if the thereby formed CTE states subsequently recombine to the ground state. A major pathway for this is the formation of triplet states. When electrons and holes collide, they randomly form either singlet or triplet states ($CTE^1$ or $CTE^3$). Since there are three possible configurations for triplet states, three quarters of the CTE states will have triplet character. This allows them to transition into a triplet exciton state ($T_1$) of either donor or acceptor without the need for intersystem crossing [82]. Re-separation into free charges from the $T_1$ state is very unlikely, and the molecules will eventually undergo non-radiative recombination. It has been shown that for some fullerene based OSCs this process can be responsible for the majority of losses in extracted charges [83]. However, another study found no influence of the $T_1$ energy level on the rate of non-radiative recombination, and suggested that non-radiative recombination occurs directly from the CTE state [84]. Nevertheless, evidence of $T_1$ formation in OSCs likely indicates losses that could be avoided, for example via careful design of molecular energy levels.

# Chapter 3

# Methods

In this chapter we present the experimental methods we used in our investigations. It begins with the steady state measurements of photon absorption and emission. These techniques are used for a basic characterisation of materials, but are also vital for interpreting the spectral features in the more advanced measurements. Similarly, information from steady state electroabsorption measurements can help identify features of separating charges in pump-probe (PP) spectra. We follow by briefly describing a time-resolved photoluminescence (PL) technique, which complements the time-resolved absorption studies that form the core of our investigation. The main part of this chapter then describes PP spectroscopy, providing an overview of the setup used and the non-linear optical effects that allow us to generate the laser pulses used in the experiment, as well as a discussion of the spectral features that can be observed in PP spectra.

## 3.1 Steady-State Measurements

### 3.1.1 UV-Vis Absorption

Measuring the absorption of molecular films and devices is a standard technique during materials development and allows basic characterisation of molecular features. In our measurements we used a commercial UV-Vis setup (8453, Agilent/Hewlett Packard). In this setup, the light of a Tungsten lamp and a Deuterium lamp are combined to a single collimated beam. This broadband light source is collimated and directed onto the sample. The transmitted light is focused onto the entrance slit of a spectrometer, where it is dispersed by a grating. Finally, the dispersed light is measured by a photodiode array. To obtain the absorption spectrum, the spectrum $I(\lambda)$ of the light transmitted by the sample is compared to the initial spectrum $I_0(\lambda)$ measured without the sample. From the difference between these spectra the absorbance $A(\lambda)$ is calculated according to

$$I(\lambda) = I_0(\lambda)\, 10^{-A(\lambda)}.$$

### 3.1.2 Photoluminesence

A complementary technique to measuring the absorption of molecular film is PL spectroscopy. Here, we excited the samples with a laser and then measured the emitted light with spectrometer and a photodiode array. We used a 407 nm pulsed laser (LDH407, PicoQuant), with a pulse length of around 100 ps, a repetition rate of 40 MHz, and a pulse energy of 6 $\mathrm{pJ/cm^2}$. The light emitted from the sample was collected with a collimating lens, and then focused onto the entrance slit of a spectrometer (SpectraPro 2500i, Acton) with a grating with 150 grooves per millimetre. The dispersed light was measured by a CCD camera (PIXIS 100F, Princeton Instruments).

### 3.1.3 Electroabsorption

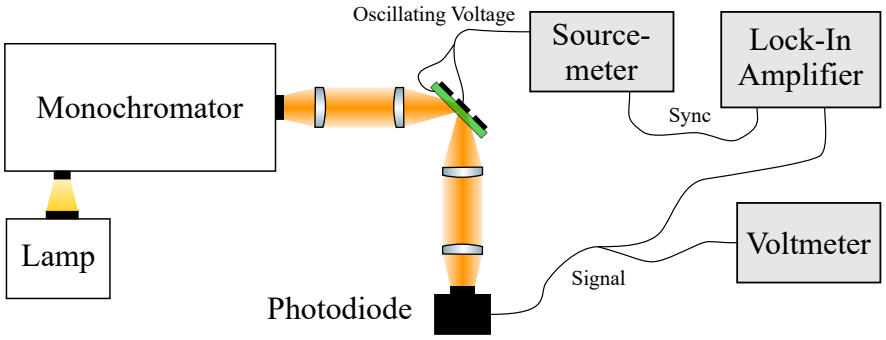


Figure 3.1: Overview of the steady-state EA setup: Monochromatic light is focused onto a sample at a 45° angle, where it is transmitted by the sample and reflected off the back contact. The intensity of the transmitted light is measured by a photodiode. A sourcemeter applies an oscillating electric field to the sample, and a lock-in amplifier detects the signal from the photodiode that oscillates with this frequency. The average photodiode signal is measured by a voltmeter.[2]

When molecules are subjected to a steady electric field, the energies of their excited states can shift downwards. This results in a red-shift of the absorption spectrum, a phenomenon known as the *Stark effect* [85]. Comparing the difference between the absorption spectra with and without an external electric field yields a electroabsorption (EA) signal proportional to the strength of electric field that roughly corresponds to the first derivative of the absorption spectra [86]. We measured this effect by applying an electric field to polymer films in a diode structure and measuring how the transmission of a monochromatic beam was influenced by the field intensity. To improve the signal-to-noise ratio, we used an oscillating field instead of a steady field, and measured the effect on the transmitted light with a lock-in amplifier.

In our setup, the light of a broadband Xenon arc lamp is reduced to a narrow spectrum by a monochromator (25015/SM, Bruker). In the monochromator the light is dispersed with a grating, and the wavelength range passing through the exit slit is selected by rotating the grating. The monochromatic light is then

[2]The ComponentLibrary (`http://www.gwoptics.org/ComponentLibrary/`) by Alexander Franzen was used for schematics in this thesis (CC-BY-NC 3.0 Unported License).

focused on the sample at an incident angle of 45°. The beam is reflected off the back-contact, collimated, and focused onto a silicon photodiode. The excitation wavelength is then scanned from 680 - 900 nm.

The electric field applied to the sample is produced by a source measurement unit (2400 SourceMeter, Keithley), generating a field oscillating from 0 - 4 V, with a modulation frequency of 470 Hz. The signal from the photodiode is measured twice: The average signal (DC component) is detected by a multimeter (34401A, Hewlett Packard), while the oscillating signal (AC component) is recorded by a lock-in amplifier (SR830, Stanford Research Systems). For each wavelength, the change in the transmitted light induced by the electric field, as measured by the lock-in, is normalised by the overall transmitted light, as measured by the photodiode. More details on this technique can be found in the PhD thesis by Thomas M. Brown [87].

## 3.2 Time-Correlated Single Photon Counting

To measure the decay times of PL, we used a time-correlated single photon counting (TCSPC) setup. It generates a histogram of the time between emission of a laser pulse exciting the sample, and detection of a photon emitted from the sample.

The sample is excited with a pulsed supercontinuum laser (SC400-2-PP, Fianium), reduced to a narrow spectrum by a bandpass filter. The emission from the sample is collimated and then focused onto the entrance slit of a monochromator. As described in the previous section, this reduces the incoming broadband pulse to a narrow spectrum. The resulting beam is detected with a photomultiplier tube (PMT) that is sensitive enough to detect single photons. The electrical trigger pulses from the laser diode driver and the PMT are processed by a Becker & Hickl TCSPC module (SPC-150N), which calculates the time between excitation and detection for each photon and generates a histogram. The time-resolved PL decays presented in Section 4.4 show these histograms as kinetics. The time resolution of the setup is $\sim 1$ ns.

## 3.3 Pump-Probe Spectroscopy

### 3.3.1 Setup Overview

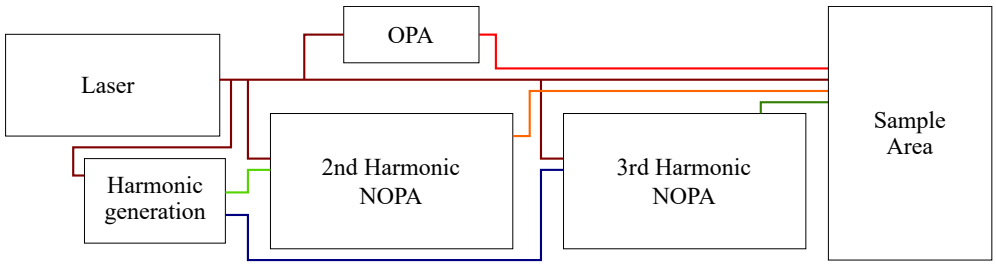


Figure 3.2: Overview of the pump-probe setup. The laser output is directed to four modules: A commercial harmonic generation unit, a commercial optical parametric amplifier (OPA), and two self-built NOPA setups. One of the NOPAs is pumped by the second harmonic output, the other one by the third harmonic output. The fundamental beam and the outputs from the OPA and the NOPAs are directed towards the sample area.

The main method we used to study excited states in our samples is *pump-probe spectroscopy* (PP), which has been widely employed to measure optoelectronic processes in organic semiconductors [88]. In this technique we measure how exciting the sample with a 'pump' pulse affects the transmission of a broadband 'probe' pulse:

$$\frac{\Delta T}{T} = \frac{T_{\text{pump on}} - T_{\text{pump off}}}{T_{\text{pump off}}}.$$

The dynamics of excited state populations can be studied by measuring this change in transmission for different delays between pump and probe. By using a chirped probe pulse and an ultrashort short pump pulse, time resolutions below 10 fs can be achieved [89]. The time resolution depends on the spectral bandwidth of the probe, the temporal width of the pump, and the specific interaction of the sample the with the probe [90].

To generate the pulses we used a pulsed Yb:KGW-based laser (PHAROS, Light Conversion). It generates pulses with a duration of $\sim$200 fs, a wavelength of 1030 nm, a repetition rate of 38 kHz, and a power of 14.5 W. For generating

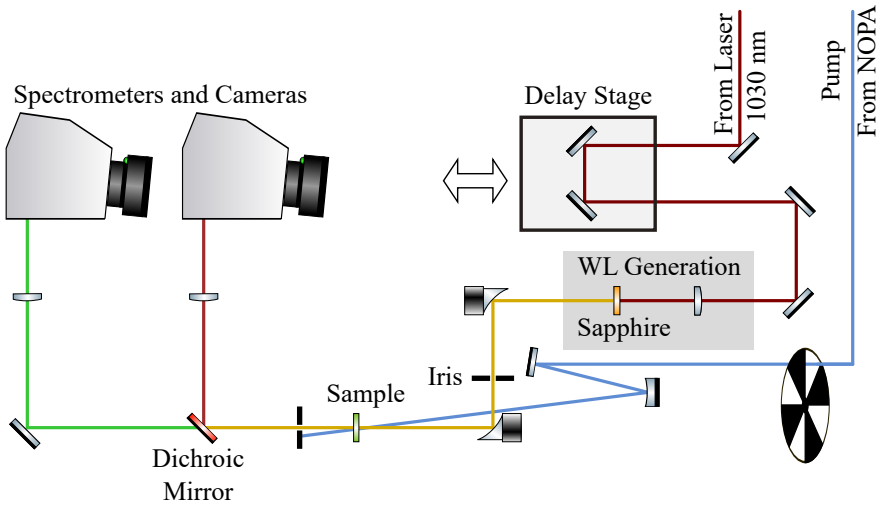


Figure 3.3: Sample area of PP setup: The white-light probe is generated by focusing the 1030 nm beam onto a sapphire crystal. A chopper reduces the frequency of the pump, and a mechanical delay stage before the white-light generation controls the delay between pump and probe. Both beams are focused onto the sample. The pump is then blocked, while a dichroic mirror splits the probe into a visible and NIR component, which are dispersed by spectrometers and measured by cameras.

the pump pulse, we use four different modules (Figure 3.2): a harmonics generator, an optical parametric amplifier, and two non-collinear parametric amiplifiers (NOPAs). A commercial module (HIRO, Light Conversion) generates second and third harmonics of the fundamental wavelength. The outputs of this module, together with the fundamental laser output, are then used for generating the broadband pump in the NOPAs, as described in the next section. If no short pulse duration is needed, a commercial optical parametric amplifier (OPA, ORPHEUS, Light Conversion) can be used to generate narrow-band pump pulses. The output of the NOPAs and the OPA are then directed towards the sample area, together with the fundamental beam.

In the sample area of the setups (Figure 3.3), the pump frequency is halved by a chopper. Thus, we are alternating between probing the sample with and without excitation. Before the fundamental is used to generate white-light, as described in the next section, a motorised delay stage with micrometer precision is used to adjust the length of the beam path. This allows us to scan the delay

between the pulses. Subsequently, pump and probe are focused onto the sample with a concave circular and a parabolic mirror, respectively. The transmitted pump is then blocked by an iris. The probe is split into a visible and a NIR beam by a 950 nm dichroic mirror. Each beam is dispersed by a spectrometer (Shamrock 163, Oxford Instruments), with a 550 nm blazed grating for the visible light and a 1200 nm blazed grating for the NIR light. The visible light is then detected by a silicon camera (custom built by Stresing Entwicklungsbüro, using a Hamamatsu S11490 photodiode array). The NIR light is measured by an InGaAs camera (SU1024LDH2, Sensors Unlimited). The cameras are triggered by the chopper sync signal, connected in series, which allows to simultaneously measure the whole probe spectrum.

### 3.3.2 Non-linear Optics

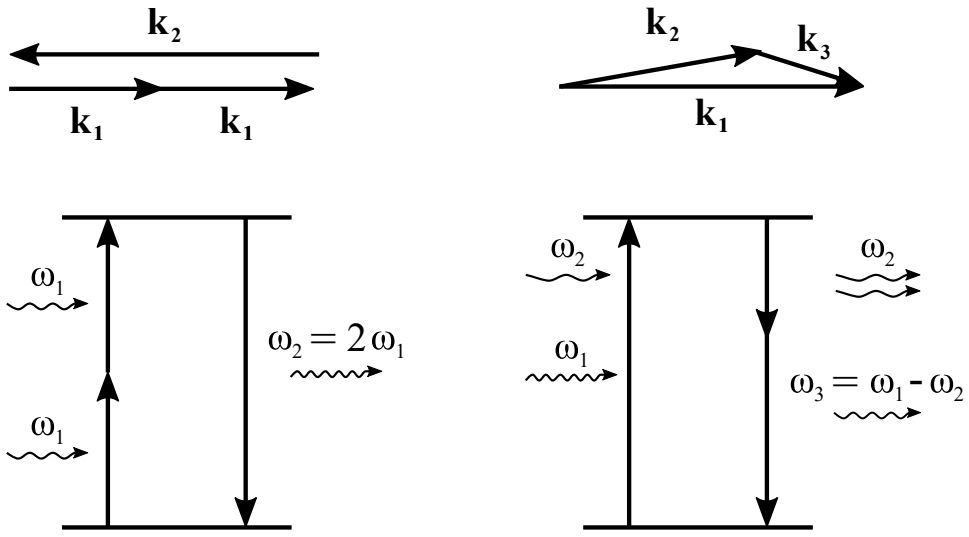


(a) 2nd Harmonic Generation (b) Parametric Amplification

Figure 3.4: Illustration of energy and wave-vector conservation (phase matching) in non-linear optics: In second harmonic generation (a) the energies $\hbar\omega$ of the incoming photons with radial frequency $\omega$ are added, the wave-vectors $\boldsymbol{k}$ are automatically matched. In optical parametric amplification (b) the energies $\hbar\omega$ of the incoming photons are subtracted, and phase matching of the wave-vectors depends on the angle between the incoming beams.

To generate the laser pulses for our pump-probe experiment, we make use of non-linear optical effects. When light and matter interact, a dipole moment is induced, referred to as *polarisation*. This polarisation can be expressed as a power series of the electrical field. To describe effects that occur at low light intensities, such as changes in the beam path due to differences in refractive index, it is sufficient to only consider the linear term of the polarisation. However, at high intensities the non-linear terms become relevant, describing the interaction of multiple photons. For example, second harmonic generation can be described as adding the energy of two photons to form a virtual energy level (Figure 3.4a). From this virtual level, a photon of twice the initial frequency is emitted. In the following we will describe two additional useful non-linear effects. A more detailed description can be found in the book "Nonlinear Optics" by Robert W. Boyd [91].

#### 3.3.2.1 White-light Continuum Generation

When intense ultrashort pulses are tightly focused in crystals such as yttrium aluminium garnet (YAG) or saphhire, the spectrum of the pulse broadens drastically. This effect is referred to as *supercontinuum generation* or *white-light generation*. Describing the mechanism behind this phenomenon is still an active research field. It is likely caused by a combination of self focusing of the beam, due to changes in the refractive index, and self-defocusing, due to the generation of an electron plasma [92]. However, other causes have been suggested as well.

In our setup we focus the 1030 nm beam onto Sapphire or YAG crystals of high purity. By placing the crystals onto a micrometer stage we are able to fine-tune the location of the focus within the crystal. We use a half-wave plate followed by a polariser to attenuate the beam. This combination gives us precise control over the beam intensity while maintaining a homogeneous beam profile. By adjusting the focus and intensity we are able to optimise stability, spectral output, and spatial profile of the white-light. To generate the probe we use a lens with a 100 mm focal length and a 4 mm thick YAG crystal.

#### 3.3.2.2 Optical Parametric Amplification

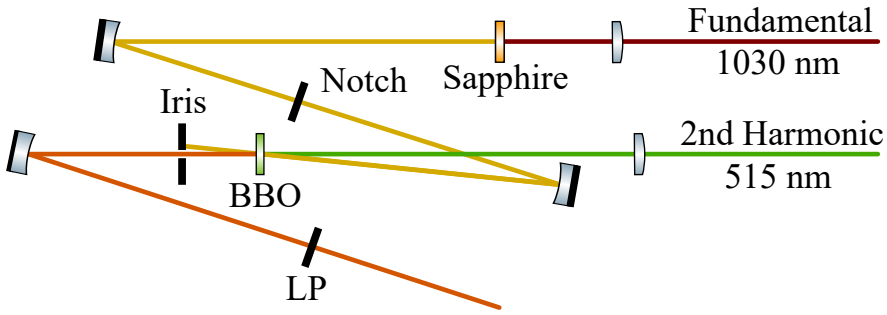


Figure 3.5: NOPA setup to generate the pump beam: The fundamental beam is focused onto a sapphire crystal to generate white-light. The white-light is collimated and focused onto a BBO crystal. The second harmonic beam is focused onto the focal spot of the white-light on the BBO, generating the broadband pump beam. An iris and long-pass filter are used to block the second harmonic and fundamental beams and remove them from the spectrum.

To generate ultrashort tunable laser pulses, *optical parametric amplification* can be used [93, 94, 95, 96, 97]. This process is similar to second harmonic generation, except that two beams with different frequencies $\omega_1$ and $\omega_2$ are interacting. In the photon picture (Figure 3.4b), a higher energy photon populates a virtual energy level $\hbar\omega_1$. The lower energy photon then stimulates the emission of one photon of frequency $\omega_2$, and one photon with a frequency $\omega_3 = \omega_1 - \omega_2$. However, for this to occur, not only the energies $\hbar\omega$ of incoming and outgoing photons have to conserved, but also their wave-vectors $\boldsymbol{k} = \boldsymbol{n}(\boldsymbol{\omega})\,\omega\,/\,c$, with the refractive index $\boldsymbol{n}(\boldsymbol{\omega})$ and the speed of light in vacuum $c$. This condition, also referred to as *phase matching*, is only fulfilled for one angle between the two incoming beams. Typically birefringent crystals are used for non-linear optics, where the refractive index is anisotropic and depends on the polarisation of the light. Thus, by rotating the non-linear crystal and adjusting the angle of the beams it is possible to change the wavelength for which these conditions are fulfilled. This is used in OPA and NOPA setups, where one of the incoming beams is spectrally broad, allowing one to choose the wavelength of the outgoing beam. In an OPA the incoming beams are co-linear inside the crystal. In this configuration, phase matching is

only possible for a narrow spectral range. In contrast, in a non-collinear OPA (NOPA), simultaneous phase-matching over a broad spectrum is possible. This allows us to generate broadband pump pulses, which is a pre-requisite for the generation of short pulses due to the Heisenberg uncertainty principle.

In our setups (Figure 3.5) we start by generating white-light as described above, which is collimated and then focused onto a $\beta$-barium borate (BBO) birefringent crystal (37° cut, type I, 5° external angle). A notch filter is used to remove the remaining strong intensity around the fundamental frequency. The second (or third) harmonic beam is focused on the crystal as well, at an angle that allows phase-matching. Following the parametrical amplification in the BBO, the beam is collimated again, and a longpass filter and an iris are used to block the second harmonic and remove its remaining intensity from the outgoing beam.

### 3.3.3 Typical Signals in Pump-Probe Spectra

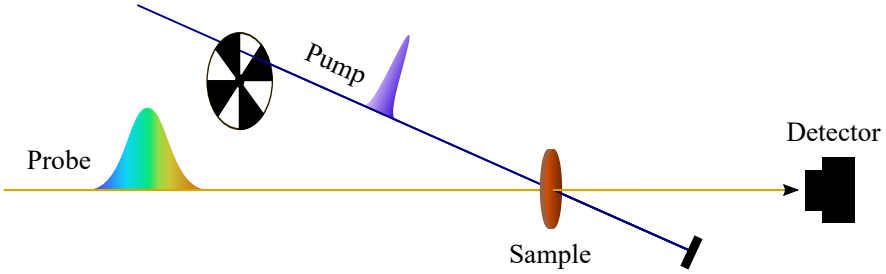


Figure 3.6: Simplified scheme of the PP setup.

Having described the experimental setup used for PP spectroscopy, we will now give an overview of the different features present in typical spectra. As mentioned before, PP spectra are obtained by comparing the transmission of the probe when the sample is excited, $T_{\text{pump on}}$, with the transmission when the pump is blocked by the chopper, $T_{\text{pump off}}$ (Figure 3.6):

$$\frac{\Delta T}{T} = \frac{T_{\text{pump on}} - T_{\text{pump off}}}{T_{\text{pump off}}}.$$

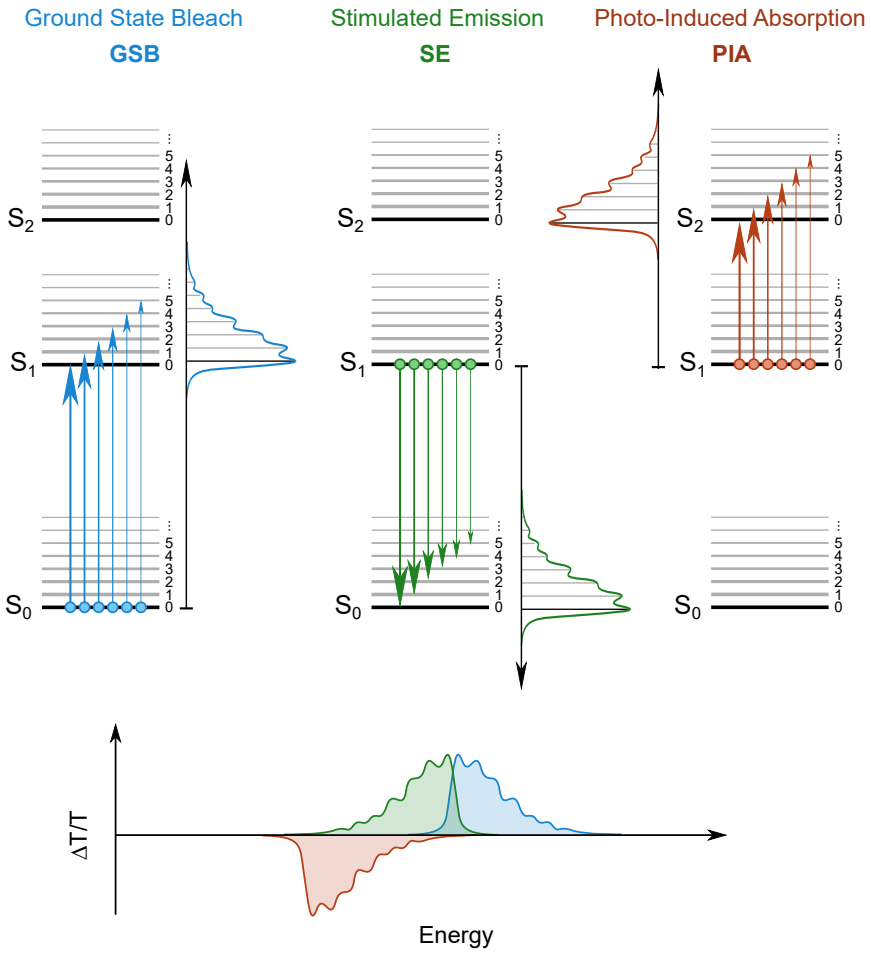


Figure 3.7: Overview of typical features in PP spectra. *Figure by Dr Andreas Jakowetz, adapted from a figure by Dr Simon Gélinas. Used with permission.*

There are three main features in typical PP spectra (Figure 3.7): The ground state bleach (GSB), which is a positive signal similar to the absorption spectrum; the stimulated emission (SE), which is a positive signal similar to the PL spectrum; and the photoinduced absorption (PIA), which is a negative signal that originates from additional absorption of excited states. We will now describe these signals in more detail.

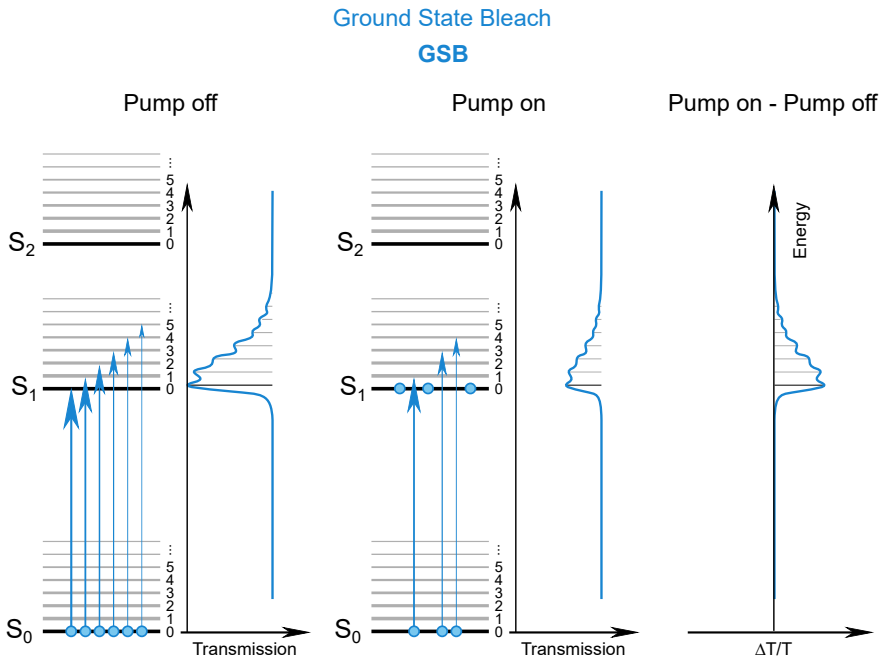


Figure 3.8: Origin of the GSB: If molecules are in an excited state, radiative transitions from the ground state are not possible. The pump therefore increases the transmission at these transition energies, resulting in a positive PP signal matching the absorption spectrum. *Figure by Dr Andreas Jakowetz, adapted from a figure by Dr Simon Gélinas. Used with permission.*

The GSB signal is the result of a reduced absorption when the sample is excited (Figure 3.8). The absorption of molecules in the ground state can be measured by steady state absorption spectroscopy, as described in Section 3.1.1. After exciting the sample, fewer molecules are in the ground state than before. Thus, the absorption at the energies that correspond to transitions from the ground state to excited states is reduced. This increases the transmission at these energies when the pump is on. Consequently, the GSB is a positive signal with a shape matching the steady state absorption spectrum. Its intensity is proportional to the number of molecules in any type of excited state.

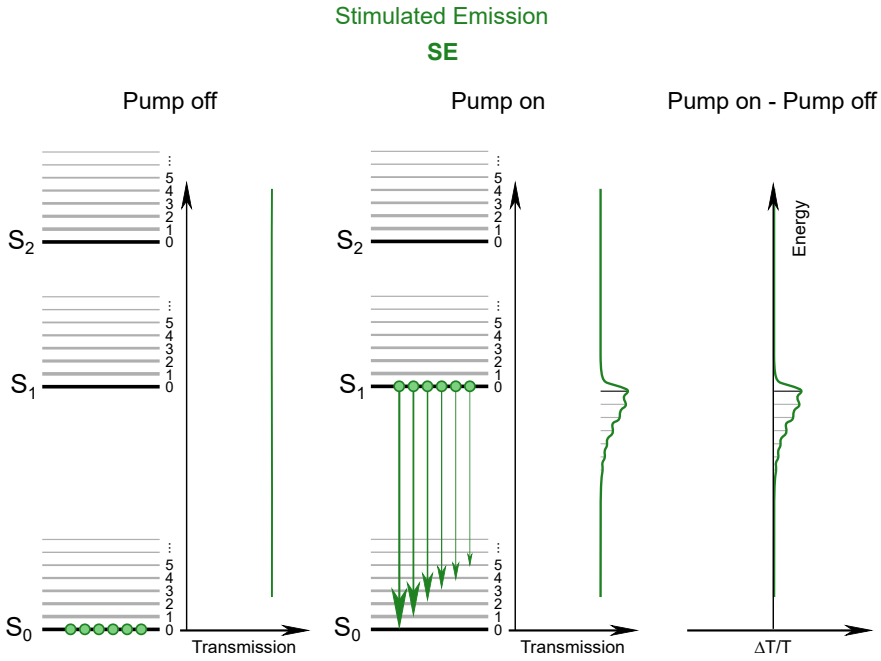


Figure 3.9: Origin of the SE: If molecules are in an excited state, the probe can induce stimulated emission. The pump therefore causes more photons to arrive at the detector, resulting in a positive PP signal matching the PL spectrum. *Figure by Dr Andreas Jakowetz, adapted from a figure by Dr Simon Gélinas. Used with permission.*

The SE signal is the result of stimulated emission from molecules in an excited state (Figure 3.9). When molecules are excited by the pump, they quickly undergo vibrational relaxation to the lowest vibrational level of the first exited state. From this state, they can radiatively transition to the ground state at random delays after the pump. The resulting emission can be measured by PL spectroscopy, as described in Section 3.1.2. However, if the excited state interacts with a photon of an energy that corresponds to a radiative transition to a lower energy state, this increases the probability of transitioning and emitting a second photon of the same energy. This process is known as *stimulated emission*, and can be induced by the probe. These emitted photons are detected as increased transmission, and therefore result in a positive signal that roughly matches the PL spectrum. Yet, the steady state PL shows the time-integrated emission, while SE shows

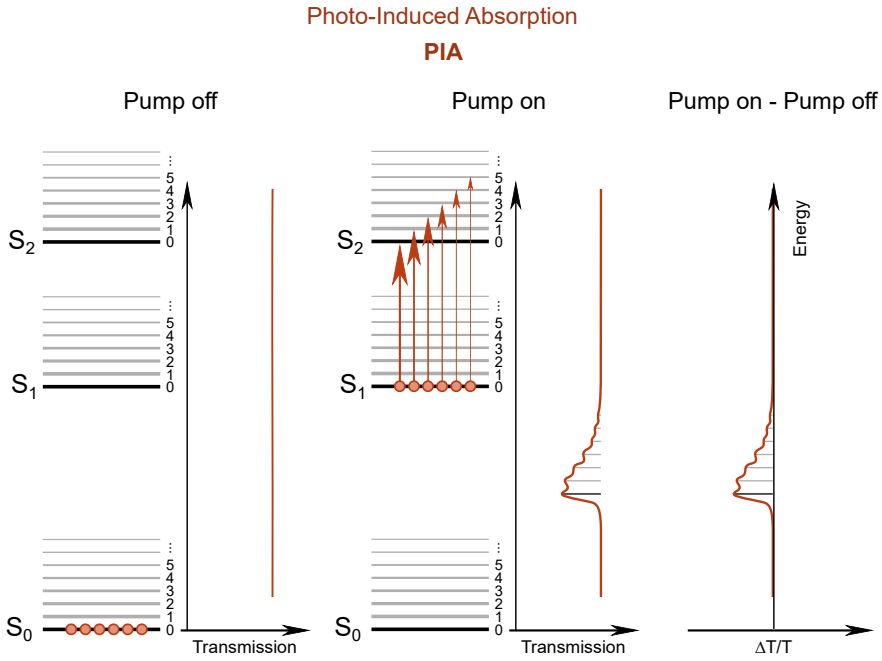


Figure 3.10: Origin of the PIA: If molecules are in an excited state, new radiative transitions to excited states of higher energy are possible. The pump therefore reduces the transmission at these transition energies, resulting in a negative PP signal. *Figure by Dr Andreas Jakowetz, adapted from a figure by Dr Simon Gélinas. Used with permission.*

radiative transitions from states that are populated at a specific time after the push. For example, energy transfer from one type of molecule to another would result in a SE signal from the first molecule at short pump-probe delays, and a SE signal from the other molecule at long delays. To summarise, the SE shows the population of excited states that can undergo radiative transitions.

The PIA signal is the result of absorption by excited states that transition to higher excited states (Figure 3.10). When the pump excites the sample, new transitions become possible. At the energies of these transitions the probe is only absorbed by molecules in the excited state. This reduced transmission results in a negative PP signal. In contrast to the SE signal, PIA is also caused by states that are not accessible via radiative transitions from the ground state, such as triplet excitons and charges.

### 3.3.4 Electroabsorption Signals

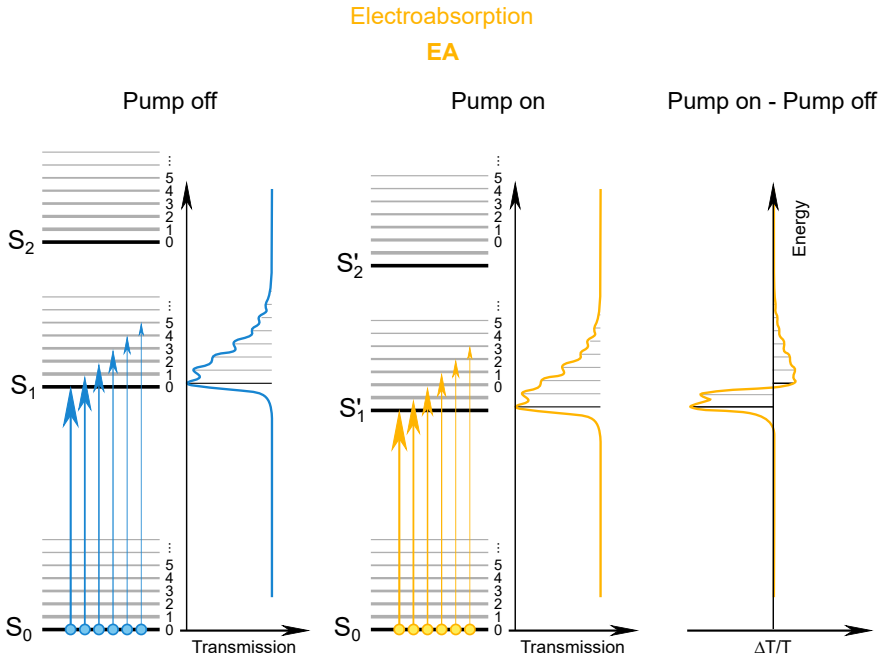


Figure 3.11: Origin of the EA signal: If the pump induces an electric field in the sample, for example the field generated by separated electrons and holes in solar cells, the absorption of the molecules in this field is red-shifted due to the Stark effect. This results in a derivative-like signal around the absorption edge of the molecule. *Figure by Dr Andreas Jakowetz, adapted from a figure by Dr Simon Gélinas. Used with permission.*

One additional signal that is particularly useful to study charge separation in OSCs is the EA signal. As mentioned in Section 3.1.3, electric fields cause a red-shift of the absorption by lowering the energy levels of the molecules. Thus, if the pump induces a (non-oscillating) electric field in the sample, the sample starts to absorb at energies below its first excited state energy. At higher energies the absorption is reduced. Consequently, the $\Delta T/T$ signal is negative below the absorption edge (less transmission) and positive above the absorption edge (more transmission).

In organic solar cells, the pump can induce an electric field via charge generation [47, 49, 98]. If charges separate at a donor-acceptor interface, they generate a microscopic field between the electron and the hole. This shifts the absorption of the nearby molecules. It can be shown that the intensity of the EA signal in a PP spectrum is proportional to the energy stored in the microscopic fields across the interface [49]. Since this energy increases when the charges separate, the EA signal can be used as a measure of their separation [47, 49, 98, 99, 100]. However, results have to be interpreted with caution, since other effects can also cause shifts in the absorption spectrum and result in similar derivative-like signals.

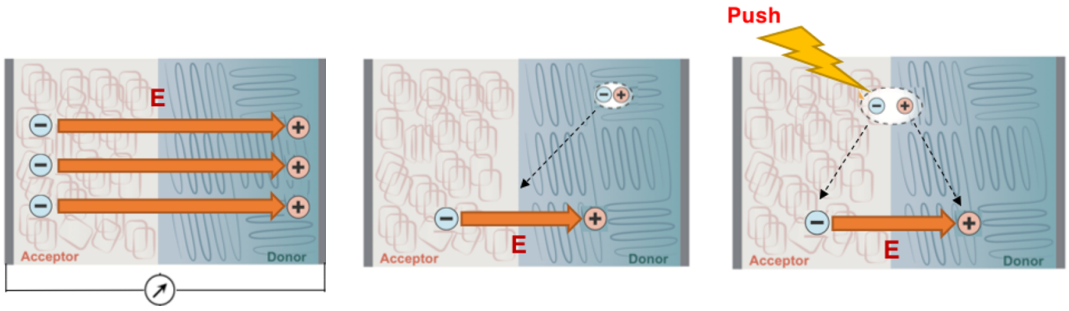


(a) Device EA (b) Pump-Probe EA (c) Pump-Push-Probe EA

Figure 3.12: Schemes of different electroabsorption (EA) signals discussed in this Thesis: A device EA signal (a) is often used as a reference. Here the electric field is applied externally. In Pump-Probe measurements (b) an EA signal is caused by the local field of charges separating across the heterojunction. In Pump-Push-Probe measurements (c) the EA signal is also caused by separated charges. However, in this case the charges bound at the interface are separating due to interaction with a laser pulse. *Figures by Dr Phillip Chow, used with permission.*

## 3.4 The Genetic Algorithm

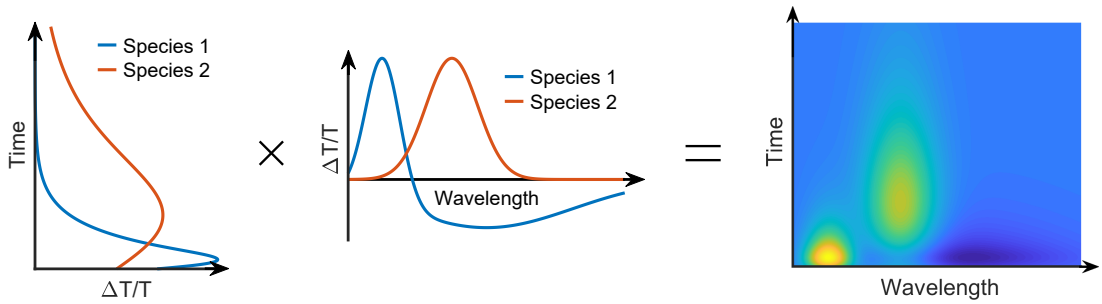


Figure 3.13: Example of a model generated by the genetic algorithm. A set of spectra optimised by the algorithm is multiplied with kinetics obtained via least squares fitting to generate a two-dimensional map of PP data.

The PP signals described in the previous section often overlap. Thus, identifying the characteristic spectral features of the different species in the sample, or extracting their time evolution, can be difficult. The *genetic algorithm* (GA) is a numerical optimisation method that has been adapted by Simon Gélinas [101] for the deconvolution of PP spectra into its components. It uses an iterative procedure similar to natural evolution to find combinations of spectra and kinetics that explain the experimental data.

If, for example, two excited states are expected in the sample, the GA would be set to find a combination of two spectra and corresponding time traces (kinetics). The spectra are stored as horizontal vectors $s_{\text{species i}}$ and the time traces as vertical vectors $k_{\text{species i}}$. A two-dimensional map can then be obtained via matrix multiplication and compared to the experimental data (Figure 3.13):

$$\left[k_{\text{species 1}}, k_{\text{species 2}}\right] \times \begin{bmatrix} s_{\text{species 1}} \\ s_{\text{species 2}} \end{bmatrix} = \begin{bmatrix} s_{t_1} \\ s_{t_2} \\ s_{t_3} \\ \cdots \end{bmatrix} = [TA]_{model} \tag{3.1}$$

where $s_{t_i}$ corresponds to the spectrum measured at the timepoint $t_i$.

The aim of the GA is to minimise the mean squared difference between the experimental data $[TA]_{data}$ and the model $[TA]_{model}$ that the GA produces:

$$res = \text{mean}\left(\left([TA]_{model} - [TA]_{data}\right)^2\right). \tag{3.2}$$

In the following we will describe the different steps of the algorithm.

### 3.4.1 Generation of a Random Population

In the first step, the algorithm generates a 'population' of sets of random spectra which are stored as rows of a matrix:

$$\begin{bmatrix} s_{\text{species 1}} \\ s_{\text{species 2}} \end{bmatrix}_1, \quad \begin{bmatrix} s_{\text{species 1}} \\ s_{\text{species 2}} \end{bmatrix}_2, \quad \begin{bmatrix} s_{\text{species 1}} \\ s_{\text{species 2}} \end{bmatrix}_3 \quad \dots \tag{3.3}$$

Each spectrum consists of a sum of random Gaussian functions with added noise, and a typical population size is 1000 sets of spectra. Increasing the population size makes it more likely that a better solution is found but also increases computation time.

It is possible to start the algorithm with an initial guess of spectra. In this case, one member of the population consists of the unmodified initial guess, while the other members are calculated as a sum of the initial guess and the random spectra described above.

### 3.4.2 Evolution

In the next stage, the random population of spectra undergoes a process that is similar to biological evolution. The best spectra are kept, while the worst ones are combined into new spectra. This occurs in iterations of the following steps:

**Fitness Calculation:** The GA optimises a population of spectra, not of the whole PP map. The kinetics that give the best approximation of the experimental data for each set of spectra are calculated on-the-fly whenever the 'fitness' is evaluated. The optimal kinetics are obtained via a least squares fit, by multiplying the matrix of the experimental data with the pseudoinverse of the matrix

containing the spectra:

$$\left[k_{\text{species 1}}, k_{\text{species 2}}\right] = \begin{bmatrix} s_{\text{species 1}} \\ s_{\text{species 2}} \end{bmatrix}^{+} \times [TA]_{exp}\,, \tag{3.4}$$

where $^{+}$ denotes the pseudoinverse of the matrix. These fitted kinetics can then be used to calculate the residual according to Equations 3.1 and 3.2.

These kinetics can be negative, which is unphysical since they represent the population of excited state species. However, temporarily allowing negative kinetics can be beneficial to find the optimal spectra faster. Thus, the optimisation target of the algorithm is to maximise a fitness function $f$ that contains a *negative kinetic penalty* factor *nkp*:

$$f = \frac{1}{res \cdot (1 + nkp \cdot (n_{k<0}/n_{total}))}, \tag{3.5}$$

where $n_{k<0}$ is the number of time-points for which the kinetics are below zero, and $n_{total}$ is the total number of time-points.

**Breeding:** To generate the population of the next step of the iteration, some of the sets of spectra are kept, while others are replaced. The replacements are 'children' spectra formed by combining two sets of 'parent' spectra. The probability of being replaced is determined by the fitness of the parents according to the *adaptive crossover probability* $P_{co}$ [102]:

$$P_{co}(f_{ij}) = \begin{cases} \frac{f_1 - f_{ij}}{f_1 - f_{av}} & \text{if } f_{ij} > f_{av} \\ \\ 1 & \text{if } f_{ij} \leq f_{av} \end{cases} \tag{3.6}$$

where $f_1$ is the fitness of the best set of spectra, $f_{ij}$ is the average fitness of the sets $i$ and $j$, and $f_{av}$ is the average fitness of the whole population. Thus, all combination of sets with a fitness below average will be replaced, and the probability of replacing the remaining sets decreases with increasing fitness. It is important to generate children spectra in a way that preserves features of the parents without introducing step changes. This can be achieved with a mask $G(x)$ generated from a random Gaussian function. One set of spectra is multiplied by the mask, and the other by the inverted mask $(1 - G(x))$. Adding these modified

spectra gives the first set of children spectra. For the second set of children, the first parent set is multiplied by the inverted mask, and the second by the non-inverted mask.

**Mutation:** As a last step of the evolution cycle, random noise is added to randomly selected points of the spectra. This ensures a diversity of spectral features and allows the development of new features over multiple iterations of the evolutions.

### 3.4.3 Generating New Populations

After a predefined number of evolution iterations, all sets of spectra are discarded except for the one with the highest fitness. These best spectra are then used as an initial guess to start a new generation of random spectra as described in Section 3.4.1. Each time a new population is generated, the algorithm reduces the strength of the noise and the intensity of the random Gaussians that are added to the initial spectra. This allows convergence to a set of spectra that does not change further.

### 3.4.4 Summary

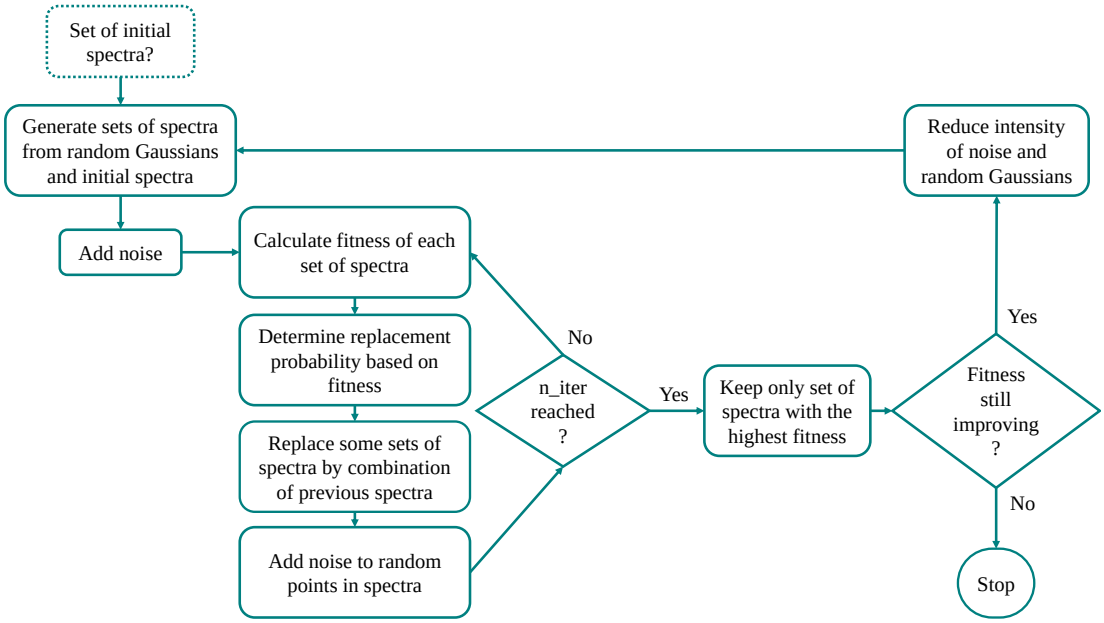


Figure 3.14: Overview of fundamental steps of the genetic algorithm.

An overview of the different steps of the GA is shown in Figure 3.14. Combined with previous knowledge of both the spectral features and the possible excited state dynamics in the sample, this algorithm can be very useful to extract the spectral features and dynamics of the different excited states. However, it is important to remember that this method involves random processes. Thus, the outcome might depend on the start parameters and it is not guaranteed that the resulting model represents the best approximation of the experimental data. Additionally, the algorithm is not well suited to account for shifts in spectra. Results should therefore always be interpreted cautiously, and the reproducibility of the results should be tested by running the algorithm multiple times with many different start parameters.

# Chapter 4

# Charge Dynamics in P3TEA:SF-PDI$_2$

As detailed in Section 2.2.3, one of the major open questions in organic photovoltaics is how charge separation can be efficient without an 'excess energy' to drive the process. Here we investigate the model non-fullerene organic photovoltaics (OPV) system P3TEA:SF-PDI$_2$, which is highly efficient in generating photocurrent despite having a negligible offset between singlet exciton and CTE state.

We begin this chapter by introducing the materials studied and their basic characteristics. Subsequently, we identify their characteristic features in PP spectroscopy and assign these features to the exited states present in the donor polymer P3TEA: singlet excitons and holes. In the next section we study the dynamics of these states in the P3TEA:SF-PDI$_2$ blend during the charge generation and separation process. We find that a significant proportion of charges are present on ultrafast timescales ($< 400\,\mathrm{fs}$), with a second slower charge generation process occurring within tens of picoseconds, while charge separation is much slower ($\sim 100\,\mathrm{ps}$). Comparing these timescales with the typical timescale of vibronic relaxation, we propose that the charge separation is a thermally activated process from relaxed CTE states. We continue by measuring the temperature-dependence of these dynamics, and indeed find that charge separation is slowed down when the sample temperature is reduced.

In the last section we focus on the reverse process: reformation of CTE states. We find a long-lived PL decay component in the blend, that is quenched when applying a reverse bias. Supported by an analysis of the resulting PL spectra, we suggest that singlet excitons are regenerated via bimolecular encounters of free charges.

The thermally activated slow charge separation from relaxed CTE states is in sharp contrast with conventional fullerene-based OSCs. Combined with the observed singlet regeneration, this strengthens the notion that a better understanding of the role of CTE states in OSCs is crucial for materials development and device design. The next chapter will therefore focus on directly monitoring the CTE population.

*This chapter is the result of a collaboration with Dr Philip Chow and co-workers from the Hong Kong University of Science and Technology, who also provided the samples for this project. Section 4.3.3 and 4.4 are largely based on work by our collaborators and are included for completeness of the story. The content is adapted from the resulting publication [103] (under review), with substantial contributions from Professor Sir Richard Friend and Dr Akshay Rao.*

## 4.1 Properties of Studied Materials

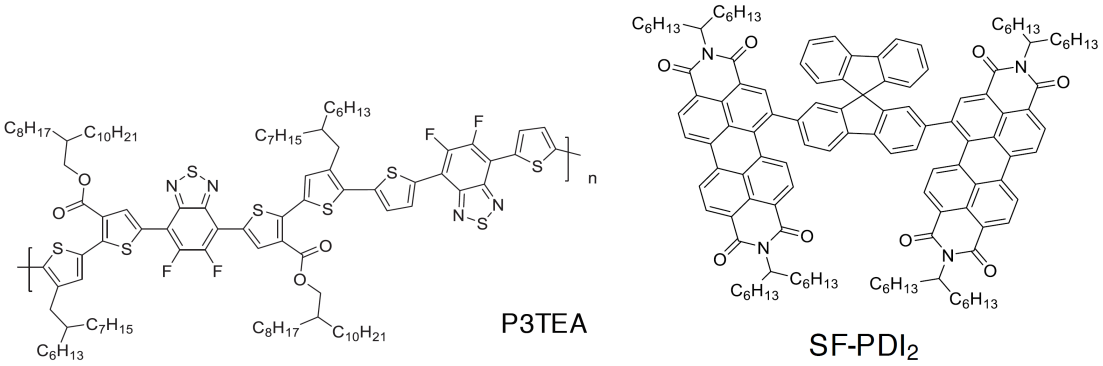


(a) Electron Donor (b) Electron Acceptor

Figure 4.1: Chemical structures of electron donor (a) and acceptor (b) molecules used as a model system to study the dynamics of CTE states.

The main model system used in this study is a blend of the polymer P3TEA, acting as an electron donor, and SF-$PDI_2$, acting as an electron acceptor (Figure 4.1). As reported previously, this non-fullerene OPV system shows small photovoltage losses and high charge generation quantum yields [66]. To determine the energy of the singlet exciton in a pristine P3TEA film, the authors compared the normalised absorption and emission spectra. The intercept of the spectra allows the extraction of $E_{S1} = 1.72$ eV. With an open circuit voltage of $V_{OC} = 1.11\,V$, this yields a photovoltage loss of $E_{loss} = 0.61\,eV$. The external quantum efficiency for electroluminescence (emitted photons per injected electron, $EQE_{EL}$) of this device is high ($0.5 \times 10^{-4}$), indicating that non-radiative voltage losses contribute $\sim 0.25\,V$ to $E_{loss}$ (see Equation 2.11). Comparing the spectra of the external quantum efficiency for the blend and the pristine donor, the authors found almost no change at the absorption edge. In particular, they did not observe additional absorption from the CTE state despite a dynamic range of four orders of magnitude. Thus, they concluded that the offset between singlet exciton and CTE state is negligible. This is plausible, given the small difference between the LUMO levels of the two materials (50 meV, Figure 4.2a). Despite this lack of a driving energy, they measured an internal quantum efficiency of nearly 90 %. This highly efficient charge generation despite low voltage

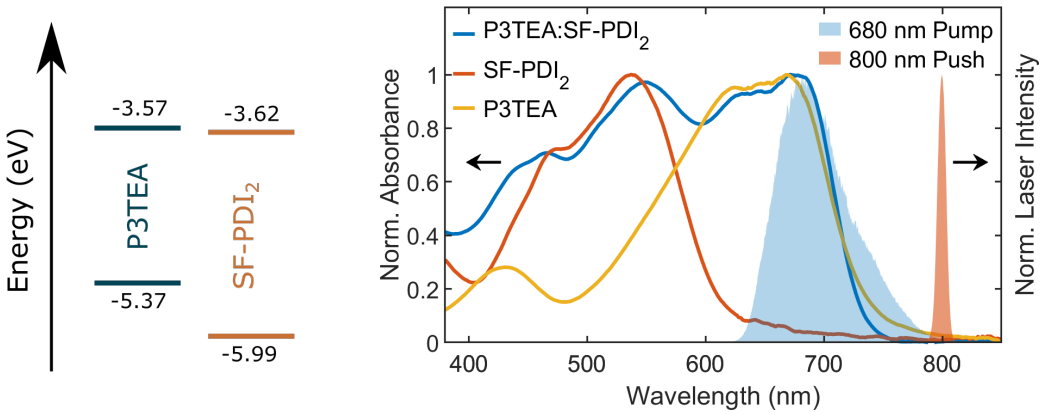


(a) HOMO & LUMO Levels [66] (b) Absorption

Figure 4.2: Absorption spectra (a) and energies of molecular orbitals (b) of P3TEA:SF-PDI$_2$ and its individual components. Also shown are the spectra of the laser pulses used to excite the samples.

loss allows a PCE of 9.5 %, making this system one of the most efficient OSCs with a small voltage loss.

In this blend the acceptor has a higher bandgap than the donor and therefore absorbs at smaller wavelengths (Figure 4.2). By exciting the blend at 680 nm we therefore expect to predominantly excite the donor, allowing us to study electron transfer to the acceptor.

An often used measure of charge formation efficiency is the extent of PL quenching. We measured the (time-integrated) PL spectrum of pure P3TEA, the P3TEA:SF-PDI$_2$ blend, and a reference P3TEA:PCBM blend (Figure 4.3). The P3TEA:SF-PDI$_2$ blend is significantly less emissive than the pure P3TEA sample, and slightly more emissive than the P3TEA:PCBM blend. To quantify this, we measured the total PL quantum yield (PLQE, emitted photons per absorbed photons) with an integrating sphere. The PLQE of the pure sample of $\approx 2\,\%$ was reduced to $\approx 0.2\,\%$ in the non-fullerene blend, indicating efficient charge generation. The fullerene blend had a further reduced PLQE of $\approx 0.1\,\%$. This higher PLQE of the non-fullerene sample is consistent with the regeneration of singlet excitons from free electron-hole encounters, as discussed in Section 4.4.

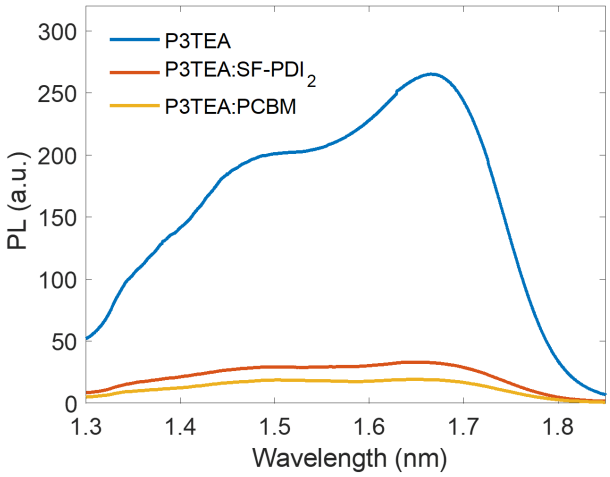


Figure 4.3: Photoluminescence spectra of P3TEA, P3TEA:SF-$PDI_2$, and P3TEA:PCBM under 633 nm excitation (corrected for the difference in absorbance between samples). *Measurements and plot by Dr Philip Chow and co-workers.*

We extended our study to include three additional non-fullerene OPV blends with negligible $E_{S1}$–$E_{CTE}$ offsets, namely P3TEA:FTTB-$PDI_4$ [104], P3TAE:SF-$PDI_2$ [105] and PffBT2T-TT:O-IDTBR [106] (see Appendix A.2 for details). Devices based on these blends can achieve large $V_{OC}$ of 1.13 V, 1.19 V and 1.08 V, respectively. The combination of small voltage losses ($< 0.6$ V) and high external quantum efficiencies ($> 60$ %) allows these systems to achieve high PCEs of 7.1 %, 10.6 % and 10.4 %, respectively. The various non-fullerene acceptors cover a range of different structural motifs (Figure A.6) and allow us to generalise the results of our study to any non-fullerene system with near zero energy offsets to drive charge separation.

## 4.2 Identifying Components of PP Spectra

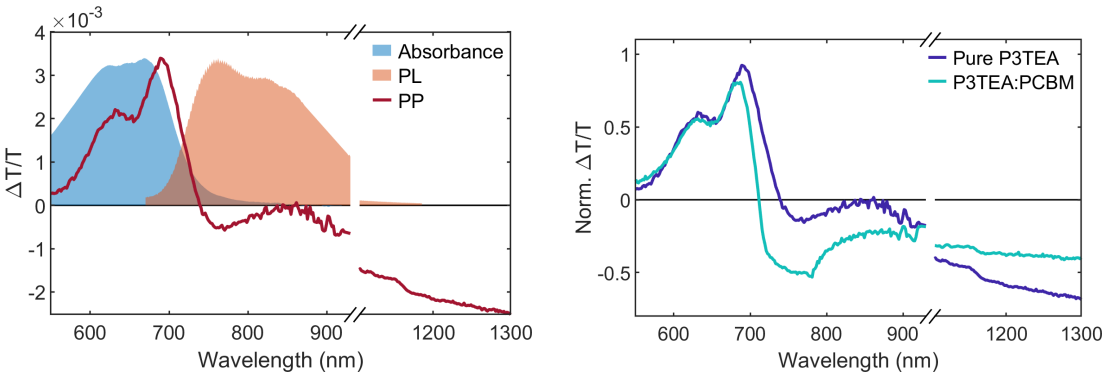


(a) Pure P3TEA (b) P3TEA:PCBM

Figure 4.4: Identifying the spectral components of PP data: (a) Comparison of the PP spectrum and the absorption and photoluminescence spectra of a pristine P3TEA film. (b) Comparison of the PP spectra of the pristine P3TEA film and a P3TEA:PCBM blend, where charge generation is known to occur.

We start our PP studies by measuring a pristine P3TEA film and comparing the resulting spectra with the UV-VIS absorption spectra and PL spectra (Figure 4.4a). This allows us to identify the different spectral features of the PP spectra described in Section 3.3.3. The spectrum is positive at 550 - 750 nm and mostly negative at longer wavelengths, with almost no signal at 850 - 900 nm.

The positive signal matches well with the absorption spectrum, and can therefore be assigned to the GSB of P3TEA. The regions where the signal is weakest match with the PL spectrum, where we would expect SE. Thus, we assign the PP signal in this region to a positive SE signal overlapped with a broad negative PIA. We have therefore identified the characteristic PP features of the pristine P3TEA film, where we expect the signal to be dominated by singlet excitons.

To identify the spectral features of charges in P3TEA, we measure a blend of P3TEA with the donor polymer PCBM. The PP signal of PCBM in this wavelength region is more than an order of magnitude lower than the signal of P3TEA. Additionally, device measurements in this blend indicate that it efficiently generates charges (Appendix Figure A.1). Comparing the PP spectrum measured in

the pristine P3TEA with the spectrum of the blend allows us to isolate the effects of charges (Figure 4.4b). We observe three main effects: the lower-wavelength edge of the GSB is blue-shifted (the zero crossing point shifts from 739 nm to 712 nm), the signal from 700 - 950 nm is much more negative, and the PIA above 1100 nm is reduced. The dip in the blend signal at 790 nm is likely to be an artefact, caused by saturation of the detector at this wavelength.

The more negative signal at 800 - 950 nm was expected: We previously described how in this region the PIA is overlapping with the SE from P3TEA singlets. If these singlets are converted into charges, we expect the positive SE to disappear and the signal to become more negative. Furthermore, we can now confirm that the strong PIA at wavelengths >1200 nm is a characteristic feature of singlet excitons in P3TEA, whereas charges have a much weaker signal in this region. The shift of the GSB and the additional negative signal at 700 - 750 nm is likely to be an EA feature. As described in Section 3.3.4 this signal indicates charge separation. We will discuss this feature in more detail for the P3TEA:SF-$PDI_2$ blend in the next section.

To summarise, we have identified the following species and their characteristic features:

- **Donor (P3TEA) singlet exciton:** GSB at 550 - 750 nm, SE at ∼800 - 950 nm, broad PIA at > 1200 nm
- **Donor (P3TEA) hole polaron:** GSB at 550 - 700 nm, EA at ∼700 - 750 nm, PIA at ∼750 - 900 nm

In the next section we will compare these features with the features in the P3TEA:SF-$PDI_2$ blend.

## 4.3 Exciton Dissociation

### 4.3.1 Tracking Charge Generation and Separation

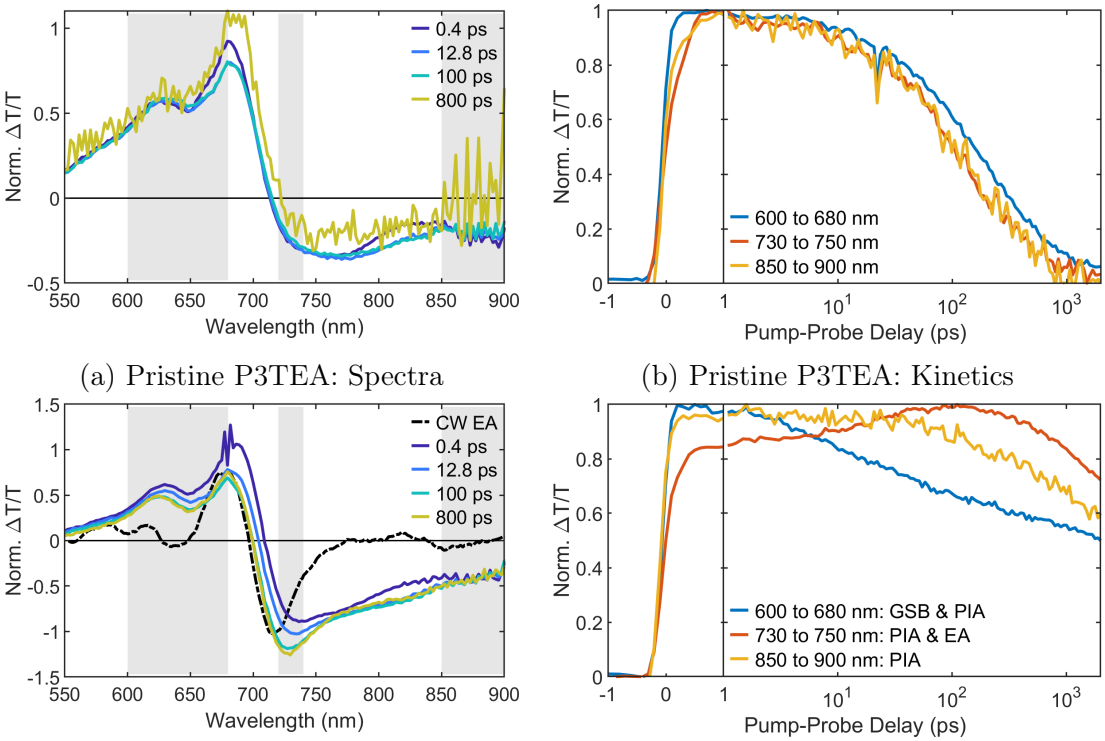


(a) Pristine P3TEA: Spectra

(b) Pristine P3TEA: Kinetics

(c) P3TEA:SF-PDI$_2$: Spectra

(d) P3TEA:SF-PDI$_2$: Kinetics

Figure 4.5: Charge generation and separation: PP spectra (a) and kinetics (b) of pristine P3TEA. PP spectra (c) and kinetics (d) of the P3TEA:SF-PDI$_2$ blend. The wavelength ranges used for extracting kinetics are shown as a grey overlay in the spectra. The black dotted line in panel (c) is the EA spectrum measured on a device. The spectra are normalised to the absolute signal strength integrated over the wavelength range shown, the kinetics are normalised to the maximum absolute signal intensity.

To explore the mechanism of charge generation and separation in P3TEA:SF-PDI$_2$, we study the kinetics of the spectral features identified above. In the pristine P3TEA film the spectra do not change significantly when increasing the pump-probe delay (Figure 4.5a). The decaying kinetics taken at three different wavelength ranges show almost identical behaviour (Figure 4.5b), indicating that

there is likely only one excited state population present in the pristine P3TEA film, namely singlet excitons. A fit with a sum of exponential decays revealed characteristic decay times of $\sim 62$ ps and $\sim 360$ ps (Appendix Figure A.2).

In contrast, in the blend the spectra evolve significantly as the probe delay increases (Figure 4.5c): The edge of the GSB blue-shifts, a new negative feature grows in at 700 - 750 nm, and the GSB peak is reduced. Additionally, the negative signal at wavelengths $> 750$ nm is stronger than in the pure film. Also shown is the EA signal measured under continuous excitation at a device (see Sections 3.1.3 and 3.3.4 for details), which matches the new negative feature around 720 nm. Taking into account the spectral components identified in the previous section, we can assign the observed spectral features in this blend as follows: The stronger negative signal above 750 nm is caused by the overlapping PIA of singlet excitons on the donor and holes generated via charge transfer onto the acceptor. The growing signal at the absorption edge, which also shifts the edge of the GSB, is likely to be an EA signal due to separation of these charges. We note that we do not observe spectral changes after 100 ps.

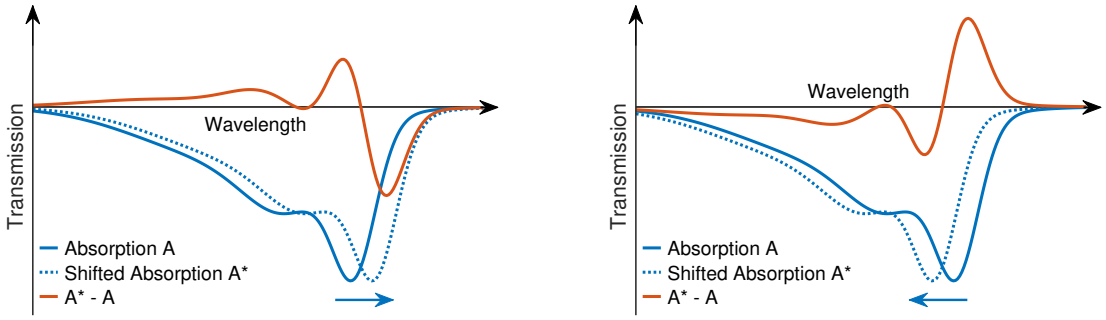


(a) Red-shift of Absorption

(b) Blue-shift of Absorption

Figure 4.6: Illustration of the origin of a derivative signal in PP spectra. When measuring the change in transmission, a red-shift of the absorption leads to a signal similar to the first derivative of the absorption (a). A blue-shift of the absorption leads to a signal of opposite sign (b).

As discussed in Section 3.3.4, the growth of a derivative-like signal near the absorption edge has been interpreted as indicating an increasing separation of charges in previous publications [47, 49, 98, 99, 100]. However, since the EA signal could easily be confused with other shifts in the absorption spectrum we will

briefly discuss our assignment. We need to distinguish between a simple shift in the GSB, which could for example be caused by an exited state population moving to states with different energies, and a derivative-like signal which also includes the growth of a negative signal at the absorption edge. First, we observe a blue shift of the ground state bleach. This would correspond to excited states moving to states with higher energy, which is unlikely. Second, we observe a negative signal at 730 - 750 nm in addition to the shift in the GSB, which is consistent with the growth of a derivative signal. This signal appears in the *Pump on - Pump off* spectrum when the absorption spectrum of the sample under excitation with the pump (*Pump on*) is shifted, as compared to the absorption spectrum of the sample without excitation (*Pump off*). A red-shift of the absorption causes a signal similar to the first derivative of the absorption spectrum, with a negative signal at the red edge of the absorption, while a blue-shift causes a signal of the opposite sign (Figure 4.6). Our observation thus indicates a red-shift of the absorption, consistent with a Stark effect due to microscopic fields of separating electrons and holes.

Another origin of derivative-like signals in PP spectra are thermal effects [107]. If the pump increases the sample temperature, we would expect an increase in the optical bandgap and thus a blue-shift of the absorption spectrum (an effect we observe in our temperature-dependent measurements discussed in Section 4.3.3). This would lead to a positive PP signal near the absorption edge (Figure 4.6b), in contrast to our observation.

To conclude, it is implausible that this signal is caused by either a shift of excitons to states with different energies or by thermal effects. Together with the appearance of a similar signal in the P3TEA:PCBM blend and prior strong evidence for charge generation occurring in these blends, we can be confident that by tracing this signal we are able to monitor charge separation dynamics.

For a better understanding of these dynamics we analysed the kinetics of these features (Figure 4.5d). Kinetics were extracted at the following wavelength ranges (grey shades in Figure 4.5a): 600 - 680 nm, where the spectrum is similar to that of pristine P3TEA; 730 - 750 nm, where the pronounced EA signal is observed; and 850 - 900 nm where the PIA features of singlet excitons and hole polarons overlap.

**600 - 680 nm (singlet and charge GSB):** The signal continuously decreases to about 50 % of its initial intensity at the end of the measurement window. Compared to the same kinetic in the pristine sample the signal intially decreases faster (in the 1 - 100 ps range), and then shows a much slower decay (> 100 ps).
**730 - 750 nm (EA):** The signal slowly increases up to 100 ps and then decreases together with the overall signal intensity.
**850 - 900 nm (singlet and charge PIA):** The signal appears within our time-resolution of ∼ 0.3 ps, is constant for the first 50 ps, and then slowly decays. At the end of the measurement window the signal is still at 60 % of its initial value, while the signal at the same wavelengths in the pristine sample has completely disappeared.

The fact that we do not observe a rise of the PIA at 850 - 900 nm could indicate that a significant part of the charge generation occurs within the time-resolution of our measurement of a few hundred femtoseconds. A similar behaviour has been reported previously by Liu et al. in the original publication of this OPV system [66], estimating that 23 % of excitons dissociated within 100 fs. They also reported that the remaining charge-generation occurs with a characteristic half-lifetime of 3 ps, which we do not observe in this measurement. Their assessment was based on the decay of the exciton PIA in the NIR region of the spectrum. However, they did not observe a corresponding rise of the hole PIA on the same timescale. It is possible that the limited wavelength range in our data prevents us from observing this slower charge generation process. We will discuss this further in the following section.

Another explanation for the presence of hole features in the initial spectrum could be the hybridisation of singlet exciton and CTE states, as discussed in Section 2.2.3. If singlet and CTE form a new mixed state, we would not be able to observe a transition between them on the timescales of our measurements.

The rise of the EA signal shows charge separation occurring on a timescale of ∼ 100 ps. We highlight that by tracking the emergence of the EA signal we monitor the separation dynamics of CTEs to free charges, while other reports to date focused on measuring the charge transfer time across the D/A heterojunctions in non-fullerene OSCs, i.e. the conversion of excitons to CTEs [37]. On the same timescale we observe a decrease in the GSB, which is likely linked to the

charge separation as well. The slower decay of the GSB compared to the pristine sample can be explained with the difference between singlet and charge decay. The kinetic in the pristine film shows the lifetime of singlet excitons, while the late-time kinetics in the blend show slowly decaying separated charges.

The slow timescale for charge separation of CTEs measured here ($\sim$100 ps) contrasts with the fast rate of vibrational relaxation for CTEs ($\leq$100 fs) [36, 108, 109]. This means that CTE separation must occur from thermally-relaxed CTEs [54]. Furthermore, it is several orders of magnitude slower than in conventional OSC blends, where ultrafast charge separation on a timescale of hundreds of femtoseconds is considered necessary for good device performance [49]. We note that no 'excess energy' is available for the systems studied here, as they have negligible $E_{S1}$–$E_{CTE}$ offsets. However, as the internal energy of free charges must lie above the coulombically-bound CTE, it follows that charges must overcome the Coulomb energy barrier to separate into free charges. This barrier, the CTE binding energy, is typically found to be 200 - 250 meV [20, 38, 46, 49]. We thus propose that the slow charge separation measured here for the non-fullerene systems is due to the need for thermal activation of the CTEs to free charges, making the process endothermic.

### 4.3.2 Charge Dynamics at Higher Fluences

In the next chapter we will discuss pump-push-probe (PPP) data measured on this system. To obtain a good signal-to-noise ratio the pump intensity was drastically increased for the PPP measurements, compared to the PP measurements. To ensure that this does not change the dynamics we simultaneously measured the PP signal. The resulting spectra are shown in Figure 4.7, normalised as described above.

In the wavelength range up to 900 nm the spectra are very similar to the ones in Figure 4.5, with differences largely due to the different wavelength range used for normalisation (non-normalised versions of the plots are shown in Figure A.3).

Additionally, the extended wavelength range $>$900 nm, compared to the previous section, allows further analysis. In the spectra measured on the pristine sample at 0.2 ps after the pump, we observe a strong PIA from 1200 to $>$1300 nm.

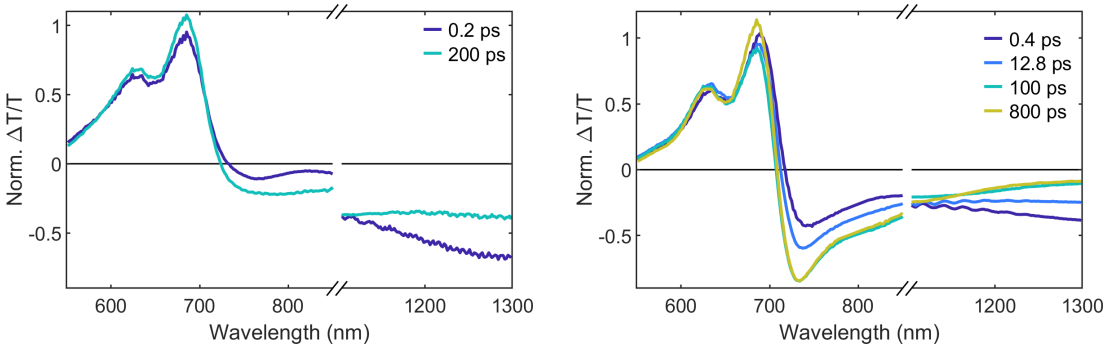


(a) Pristine P3TEA (b) P3TEA:SF-PDI$_2$

Figure 4.7: Charge generation and separation: PP spectra of pristine P3TEA (a) and the P3TEA:SF-PDI$_2$ blend (b) at the higher pump fluences used in PPP measurements ($\sim 1\,\mu J/cm^{-2}$). Spectra are normalised to the absolute signal strength integrated over the wavelength range shown.

In the blend this PIA is present at early times as well, although weaker. At long pump-probe delays this signal has almost completely disappeared. Based on our previous conclusion that the singlet excitons are transformed into charges in the blend, we can assign this PIA to singlets in the P3TEA. The spectral change of this PIA in the pristine sample is likely due to the overlapping positive SE signal. The PL of this sample spans from 700 - 1000 nm ($\sim$1.2 - 1.7 eV, Figure 4.9; also Figure 4.4a), so we expect a SE signal in this wavelength which can disappear at later times if the population shifts from a bright singlet state to a dark state. At these high excitation densities it is also possible that singlet-singlet annihilation leads to charge generation even in the pristine sample. This would also reduce the singlet PIA. However, in the blend the signal continues to decay over several tens of picoseconds, long after the fast timescale for the initial charge generation discussed above. Thus, in this measurement we do observe evidence for a slow component of the singlet dissociation similar to the report mentioned in the previous section, albeit on a longer timescale of tens of picoseconds.

This slow component could be due to diffusion of singlets to the donor-acceptor interface before fast charge generation can occur. Another possible interpretation is that only some of the singlet and CTE states are hybridised, causing the initial charge signal, while others are separate singlet states that dissociate within tens

of picoseconds. This could be the case if hybridisation strongly depends on the local morphology at the heterojunction.

### 4.3.3 Temperature Dependence of Charge Separation

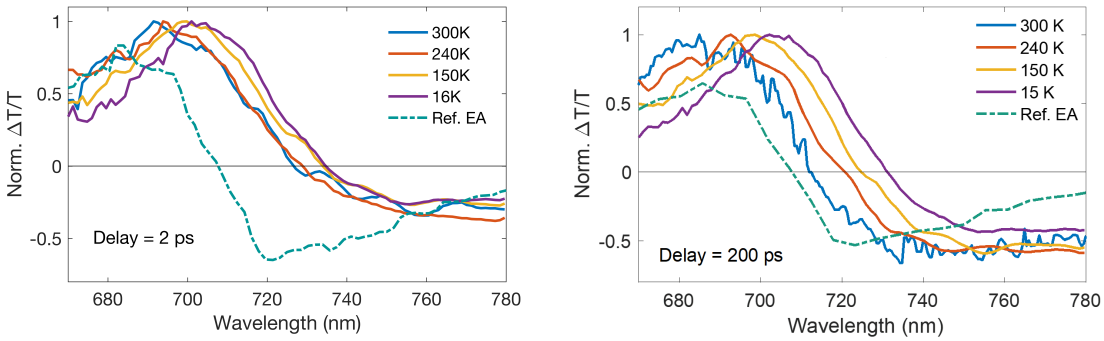


(a) Δpump-probe: 2 ps (b) Δpump-probe: 200 ps

Figure 4.8: Temperature dependence of PP spectra of P3TEA:SF-PDI$_2$ as measured 2 ps after the initial excitation (a), and 200 ps after the initial excitation (b). Also shown is the reference EA spectrum measured on a device. *Measurements and plots by Dr Philip Chow and co-workers, used with permission.*

To further explore the proposed endothermic nature of charge separation we perform PP spectroscopy at reduced temperatures. We find little effect of temperature at early times, with the PP spectrum (associated mostly with singlet excitons) largely unchanged except for a slight red shift of the GSB due to lowering of bandgap upon cooling (Figure 4.8a). At 200 ps, however, we observe a clear temperature dependence (Figure 4.8b); the PP spectrum showing a weaker PIA response at $\sim$750 nm and less spectral blue shift near the band edge at $\sim$700 nm (which is associated with the rise of the EA response) at reduced temperatures. This indicates that the long-range charge separation is suppressed at lower temperatures in the non-fullerene blend, confirming that it is an endothermic process.

In contrast, reducing temperature has insignificant effects on charge separation in the P3TEA:PCBM blend (Appendix Figure A.4), consistent with the considerable $E_{S1}$–$E_{CTE}$ offset expected for this system (see energy levels in Appendix Figure A.7) and previous reports that charge separation via the delocalised electronic states of fullerene acceptors is a temperature-independent process [49, 110].

Examining the effect of temperature on the charge generation yield, we find that for the P3TEA:SF-PDI$_2$ blend almost no photocurrent is generated below $\sim 120\,\mathrm{K}$ (Appendix Figure A.5). In comparison, we find that P3TEA:PCBM has a much weaker dependence on temperature. Weak temperature dependence of photocurrent yield is also found in other efficient fullerene-based systems that are designed with energy offsets to drive charge separation [110]. These results are consistent with the proposed endothermic nature of free charge generation in the non-fullerene blends studied here.

However, measurements of photocurrent probe not only the charge generation and separation but also carrier transport, recombination, and extraction processes. One previous study of polymer solar cells attributed the temperature dependence of the photovoltaic quantum efficiency ($\mathrm{EQE_{PV}}$, charges generated per incident photon) mainly to charge separation, and given this interpretation the authors extracted an activation energy $E_a$ [110]. To achieve this, they fitted the Arrhenius equation $k = A\exp(-E_a/k_BT)$ (with the rate constant $k$, Boltzmann constant $k_B$, the temperature $T$, and a pre-exponential factor $A$) and replaced the rate $k$ with the measured quantum efficiency, which corresponds to the resulting overall efficiency of the process. The $\mathrm{EQE_{PV}}$ depends on the complex interplay of the rates of all processes involved. Besides, even in a simplified model of an isolated charge separation process, measuring the temperature dependence of the photocurrent or $\mathrm{EQE_{PV}}$ under continuous illumination would not yield the activation energy since all carriers would eventually overcome the activation barrier [111]. Additionally, other studies have attributed changes in the photocurrent exclusively to carrier mobilities [112, 113]. Thus, the possibilities to extract information on the energetics of the charge separation process from photocurrent measurements are limited.

## 4.4 Dynamics of CTE Reformation

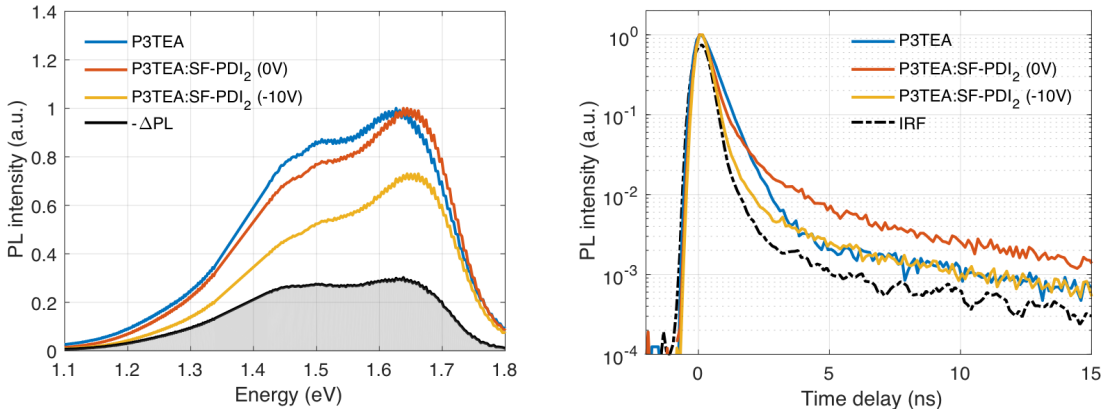


(a) Spectra (b) Kinetics

Figure 4.9: Photoluminescence data of pure P3TEA and the P3TEA:SF-PDI$_2$ blend measured with and without reverse bias. *Measurements and plots by Dr Philip Chow and co-workers, used with permission.*

We now turn to the dynamics of CTE reformation and the high $EQE_{EL}$ shown by the non-fullerene blend. To investigate how charge generation influences the emission from the donor singlet state, we compare the PL spectra of pristine P3TEA and the P3TEA:SF-PDI$_2$ blend. In order to identify the effect of charge encounters, we measured the blend PL in a device under both open-circuit conditions and when applying a negative bias of - 10 V. The negative bias increases the electron-hole separation, which lowers the rate of random encounters between charges [114]. Differences in the PL at 0 V and at - 10 V can therefore be attributed to reformation of CTE states.

The spectra of pristine P3TEA and P3TEA:SF-PDI$_2$ without applied bias are very similar (Figure 4.9a), with a small red-shift of the emission for the blend. When a negative bias is applied, the PL of the blend is reduced. The difference between the blend emission at 0 V and at - 10 V (Figure 4.9a, black line) closely resembles the PL spectrum of the pristine P3TEA, originating from the singlet state. This is an initial indication that due to the negligible energy difference between CTE state and singlet state of the donor, singlets are repopulated when

charges collide. This has been reported previously for a polymer-polymer donor-acceptor blend [115], and for non-fullerene OSC blends [37, 116].

We explore this further by analysing the decay of the PL signal via time-resolved measurements (Figure 4.9b). Comparing the kinetics of pristine P3TEA and the P3TEA:SF-$PDI_2$ blend at zero bias, we find that in the first few nanoseconds the blend PL decays faster. This can be explained by quenching of the singlet PL due to charge formation. However, at longer times ($>3$ ns) the blend PL decays slower than the PL from the pristine sample. This slow component is reduced when a negative bias is applied. Both of these observations support the view that when electrons and hole collide and form a CTE state, back-transfer from this state to the singlet exciton can occur.

## 4.5 Conclusions

In this chapter we presented our PP and time-resolved PL measurements of P3TEA:SF-PDI$_2$. In our PP data we found that the spectral features indicating the presence of charges initially appear on ultrafast timescales after the initial excitation ($< 400\,\mathrm{fs}$), which we attributed to either ultrafast charge transfer or hybridisation of singlet and CTE states. However, the separation of these Coulombically bound states into free charges occurs on a much slower timescale of $\sim 100\,\mathrm{ps}$. This is several orders of magnitude slower than in efficient fullerene-based OSCs. Based on this slow separation and the lack of excess energy as a driving force for charge separation, we proposed that in this blend charge separation is thermally activated. This was supported by our observation that the separation is slowed down further at low temperatures.

In the high-fluence measurement, which covered a wider wavelength range, we found evidence for a second, slow charge generation component (tens of picoseconds), similar to previous reports. This could be caused by either diffusion of singlets to the interface or slow dissociation of non-hybridised singlets. Additionally, we observed long-lived PL in the blend, that was quenched when we applied a reverse bias. We assigned this emission to the regeneration of singlet excitons via CTE states formed by non-geminate encounters of charges.

The slow charge separation from thermally relaxed CTE states and the regeneration of singlets from encounters of free charges suggest that CTE states play an important role in the efficient generation of photocurrent in these materials. However, the techniques described in this chapter do not allow us to directly track the CTE population. In the next chapter we therefore turn towards PPP spectroscopy.

# Chapter 5

# Probing CTE States with Pump-Push-Probe Spectroscopy

While PP spectroscopy allows us to track the spatial separation of carriers via growth of the EA signal, as described in the previous chapter, it does not provide a picture of the size of CTE population confined at the heterojunctions. In this chapter we describe how we extended our PP spectroscopy setup with a third laser pulse, which further excites the sample before measuring the absorption. This PPP spectroscopy allows us to interact with excited states in the sample and then probe the optical response to this additional excitation. In our case we are able to identify a feature that is specific to the CTE states, allowing us to probe these states directly at different times after the initial excitation. Based on observations in the model polymer-donor non-fullerene-acceptor blend P3TEA:SF-PDI$_2$ we propose that these OSCs operate in a thermodynamic equilibrium between free charges, CTE and singlet excitons. In sharp contrast with conventional OSC blends, this allows endothermic charge separation of CTE via thermal activation and hence results in minimum voltage loss. By extending our study to P3TEA:FTTB-PDI4, P3TAE:SF-PDI2 and PffBT2T-TT:O-IDTBR, we show that the proposed new operation mechanism is ubiquitous in non-fullerene OSCs. We believe that this study provides insights that facilitate the development of high performance materials.

# 5 PROBING CTE STATES WITH PPP SPECTROSCOPY

Following a description of the setup we begin our analysis of PPP spectra by discussing the origin of the features observed in pristine P3TEA films. Since we do not expect charges to be present in these samples, we can attribute all features to an interaction of the push with singlet excitons. A careful investigation of the spectral features and their dynamics in the pristine film then enables us to identify additional features appearing in the P3TEA:SF-PDI$_2$ blend. In particular, we identify a feature that matches the device EA spectrum, which we attribute to an increased charge separation when the push interacts with CTE states.

In the next section we investigate how this CTE response develops when increasing the delay between the initial excitation and the push pulse. We find a strong CTE signal at push delays of as long as 1 ns, which is approximately an order of magnitude longer than the charge separation timescales determined in the previous chapter. We also find that at low temperatures the CTE population per singlet is drastically increased, providing further evidence for thermal activation of the charge separation. Lastly, we find that interaction with the push can regenerate singlets. Taken together, these observations provide evidence for the formation of the thermodynamic equilibrium between states that we mentioned above. At the end of this chapter we discuss the implications of these findings for future efforts to increase OPV efficiencies.

*This chapter is the result of a collaboration with Dr Philip Chow and co-workers from the Hong Kong University of Science and Technology. The pump-probe part of Section 5.2.4 is based on work by our collaborators, who also provided the samples for this project. Section 5.2 and 5.3 are adapted from the resulting publication [103] (under review), with substantial contributions from Professor Sir Richard Friend and Dr Akshay Rao.*

## 5.1 Identifying Components of PPP Spectra

In this section we describe the different components we have identified in the PPP spectra of P3TEA:SF-PDI$_2$. We first focus on data from a film consisting of only P3TEA, and discuss two PPP components that can be attributed to singlet annihilation and temporary charge formation, respectively. We then turn towards the P3TEA:SF-PDI$_2$ blend to identify a feature related to CTE states. This section focuses on describing the spectral features and understanding their origins. The following section then uses these insights to analyse the photophysics of charge separation and discuss the implications for the design of organic solar cells.

PPP spectroscopy has been used previously to study charge dynamics at the interfaces of OPV systems [38, 98]. By adding an additional manual delay stage we were able to extend the range of pump-push delays by two orders of magnitude. Furthermore, we investigate the origin of the different components of the PPP signal in more detail than previously done.

### 5.1.1 Experimental Setup and Background

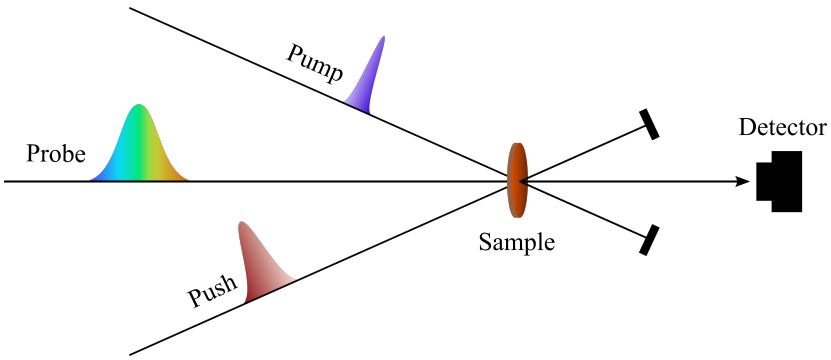


Figure 5.1: Simplified pump-push-probe setup.

PPP spectroscopy extends PP spectroscopy by adding a third pulse (Figure 5.1). Initially, a 'pump' pulse excites the sample with an energy sufficient to create an excited state population, for example singlet excitons in the $S_1$ state. Subsequently, a 'push' pulse excites the sample a second time. It is usually tuned to an energy low enough not to be absorbed by the ground state, so that it

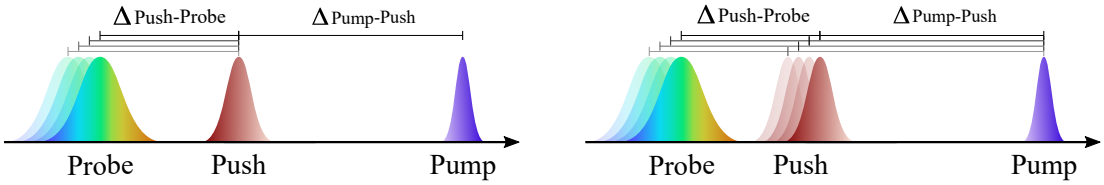


(a) Tuning Δpush-probe (b) Tuning Δpump-push

Figure 5.2: Scheme illustrating the two different modes of PPP measurements: (a) Tuning Δpush-probe while Δpump-push is fixed. (b) Tuning Δpump-push while Δpush-probe is fixed.

can only be absorbed by excited states. Finally, the transmission of a broadband 'probe' pulse is measured. We then calculate the difference between the PP signal after exciting with both pump and push

$$(\Delta T/T)_{\text{push on}} = \frac{T_{\text{push on, pump on}} - T_{\text{push on, pump off}}}{T_{\text{push on, pump off}}}$$

and the normal PP signal

$$(\Delta T/T)_{\text{push off}} = \frac{T_{\text{push off, pump on}} - T_{\text{push off, pump off}}}{T_{\text{push off, pump off}}}$$

to obtain the PPP signal

$$\Delta(\Delta T/T) = (\Delta T/T)_{\text{push on}} - (\Delta T/T)_{\text{push off}}.$$

Tuning the delay between pump and push allows us to interact with the system at different steps in the excited state dynamics. Additionally, it is sometimes possible to only excite specific sub-populations of the excited states by tuning the push wavelength. And finally, tuning the delay between push and probe delay allows us to control how much time the system is given to relax after the interaction with the push. As we will see in the following, observing changes in the PPP signal in response to changes in these parameters allows us to study different processes of relevance for solar cell operation.

When measuring PPP spectra, we generate a full PP map for each fixed pump-push delay. To understand the origin of features in these spectra it is important to analyse both aspects: When pushing the sample at a certain time after the

pump, how do the spectra depend on the push-probe delay (fixed Δpump-push, Figure 5.2a)? And how does the response at a certain time after the push depend on the pump-push delay (fixed Δpush-probe, Figure 5.2b)? To simplify this discussion we use a colour-code for PPP spectra: When we show spectra with a fixed pump-push delay and varying push-probe delays we use orange-to-brown colours, when we show spectra at a fixed push-probe delay at different pump-push delays we use blue-to-green colours.

### 5.1.2 Features in Pristine P3TEA

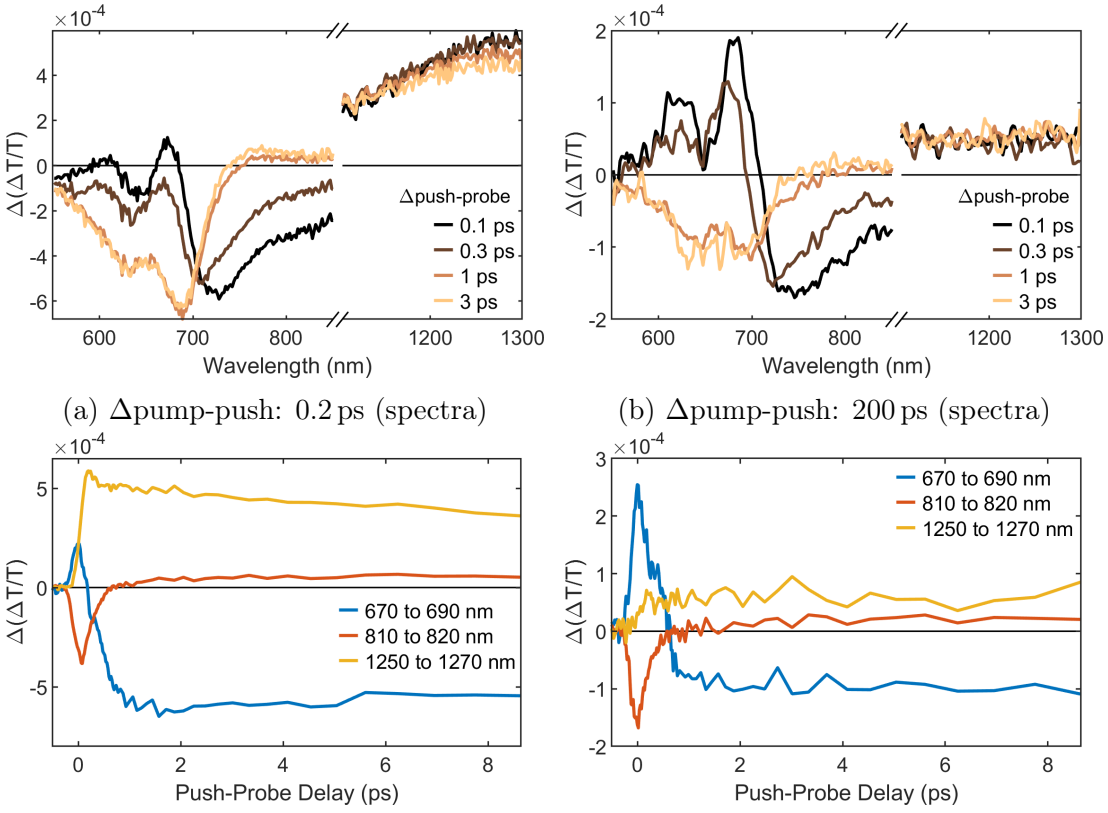


(a) Δpump-push: 0.2 ps (spectra)

(b) Δpump-push: 200 ps (spectra)

(c) Δpump-push: 0.2 ps (kinetics)

(d) Δpump-push: 200 ps (kinetics)

Figure 5.3: PPP spectra (a)&(b) and kinetics (c)&(d) of P3TEA at two different pump-push delays and various push-probe delays. There are two different regimes: rapid change within 1 ps, followed by slow evolution.

We begin our analysis by measuring a pristine P3TEA film at two different pump-push delays (0.2 ps and 200 ps) and varying push-probe delays (Figure 5.3). Similar to the previous chapter we expect only one excited species to be present in this sample, simplifying the analysis. In this measurement, as in all other data presented in this chapter, the push wavelength was set to 900 nm. At this wavelength the PP spectra of both singlet excitons and charges show a PIA signal, as shown in Chapter 4.3.1. Thus, the push can be absorbed by both of these states. As we demonstrate at the end of this section (Figure 5.12), absorption of the push by the ground state does not significantly contribute to the signals.

At both delays we observe two different regimes: The signal changes drastically within the first picosecond and remains largely constant afterwards. This is apparent in the strong difference between the spectra taken at 0.1 - 0.3 ps and the spectra taken at 1 - 3 ps (Figures 5.3a and 5.3b), and in the decay of the initial signal within $\sim$1 ps in the 670 - 690 nm and 810 - 820 nm kinetics (blue and red lines in Figures 5.3c and 5.3d).

We will first discuss the spectra in the second regime, at push-probe delays longer than 1 ps (Figure 5.4a). To account for changes in the overall population density, we normalise the signal with the PIA intensity in the PP signal near the push wavelength (910 - 930 nm) whenever we are comparing spectra at different push delays. To understand the origin of this feature we compare it with the normal PP signal discussed in the previous chapter. When we extract the spectra at the same pump-probe delays, the shape of the PPP spectrum matches the inverted PP spectrum (black dotted line in Figure 5.4a). This can be explained when considering how the PPP signal is calculated: the PP signal without the push is subtracted from the PP signal when the push is present. Therefore, if the effect of the push is to reduce the overall PP signal by a factor $0 < \alpha < 1$ without changing the spectrum, we expect the PPP signal to be

$$\begin{aligned}\Delta(\Delta T/T) &= (\Delta T/T)_{\text{push on}} \;-\; (\Delta T/T)_{\text{push off}} \\ &= (1-\alpha)\,(\Delta T/T)_{\text{push off}} \;-\; (\Delta T/T)_{\text{push off}} \\ &= -\alpha(\Delta T/T)_{\text{push off}}.\end{aligned}$$

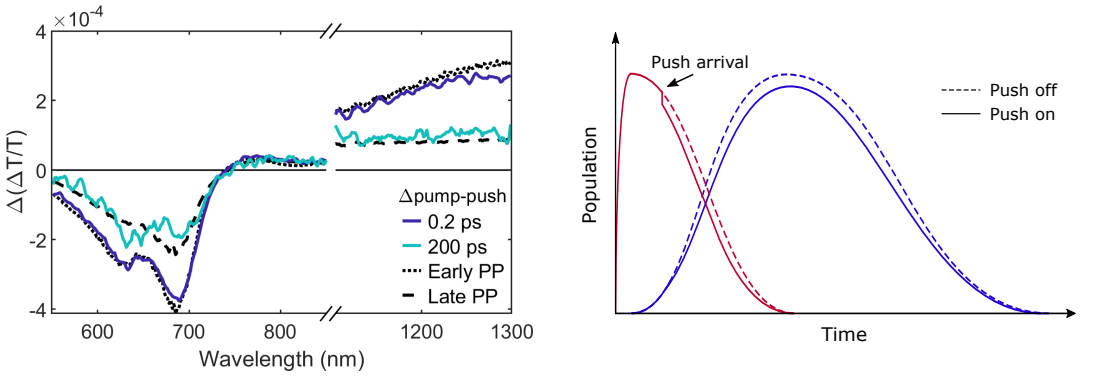


(a) PPP spectra (b) Schematic representation of dynamics

Figure 5.4: PPP at long push-probe delays: (a) PPP spectra of P3TEA after the initial feature has disappeared (Δpush-probe: 2-5 ps). Also shown is the inverted PP spectra measured at the same Δpump-probe. (b) Effect of overall reduction of population by the push. If the push reduces the population of the initial species, it also reduces the population of of any species that is subsequently generated from the first.

For example, if the push is reducing the excited state population by 1 %, we expect the PPP spectrum to be the inverted PP spectrum reduced to 1 % of its intensity. Importantly, this is true even if there is a transition between different excited states in the time between absorption of the push and measurement by the probe. If the push reduces the population of the initial state it also reduces the population of the final state (Figure 5.4b).

Consequently, we presume that one effect of the push is to reduce the overall exited state population. A previous study found that the rate of exciton-exciton annihilation in a pure conjugated polymer film increases when the excitation energy increases [117]. Thus, singlet excitons at higher energies annihilate faster. This explains why the push reduces the overall PP signal: It elevates the excitons to higher energies, where part of the population annihilates. For example, the push reduces the early PP signal in Figure 5.4a by ≈4 %, corresponding to a 4 % reduction in population.

Having identified the origin of one of the components of the PPP signal, we can now subtract this component from our data. This allows us to study the other components in more detail. To achieve this, we multiply the PP data

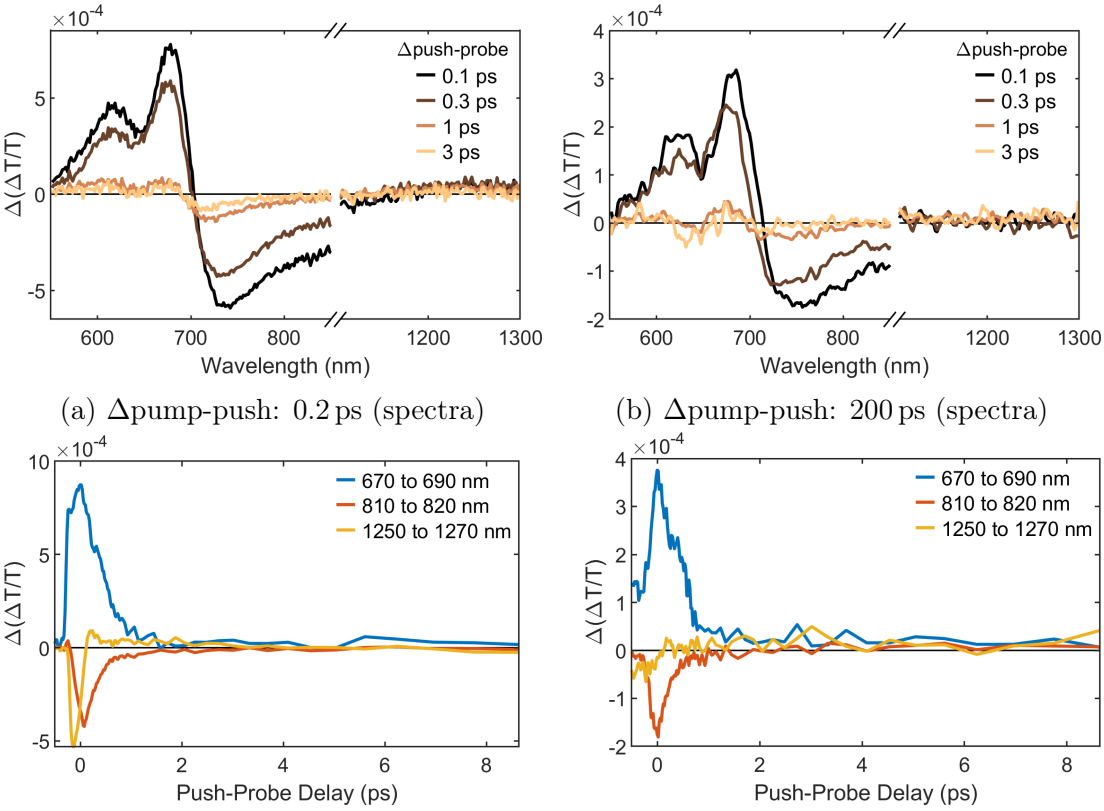


(a) Δpump-push: 0.2 ps (spectra)

(b) Δpump-push: 200 ps (spectra)

(c) Δpump-push: 0.2 ps (kinetics)

(d) Δpump-push: 200 ps (kinetics)

Figure 5.5: PPP spectra (a)&(b) and kinetics (c)&(d) of P3TEA after removing the contribution of singlet annihilation.

with a factor $\alpha$ and then add it to the PPP data (equivalent to subtracting an inverted signal). For each pump-push delay we chose the factor to minimise the signal at long push-probe delays (Figure 5.5). After this subtraction the spectra and kinetics at the two different push delays look remarkably similar. We can confirm that the initial component disappears almost completely within the first 1 - 2 ps.

As explained above, the reduction in signal occurs when the pump is absorbed. This justifies our approach of keeping $\alpha$ constant over all push-probe delays for a specific pump-push delay. However, due to noise in the data the exact choice of this parameter relies on subjective judgement. This adds uncertainty to the interpretation of the data and should be considered in any conclusions.

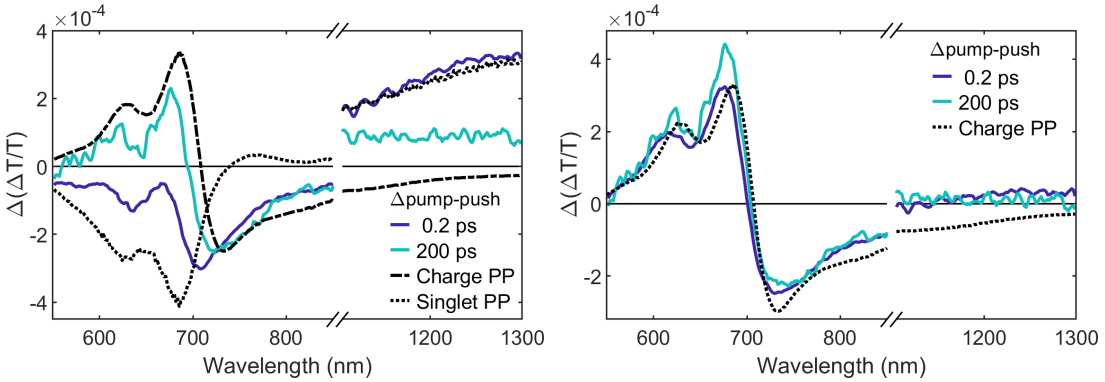


(a) Before subtraction (b) After subtracting singlet component

Figure 5.6: Initial PPP spectra of P3TEA (Δpush-probe: 0.2 - 0.5 ps) before (a) and after (b) removing the contribution of singlet annihilation. Also shown are the PP spectra of P3TEA at early times ('Singlet PP') and of P3TEA:SF-PDI$_2$ after charge separation ('Charge PP').

We now continue by discussing the other component of the PPP signal, which dominates at push-probe delays shorter than 1 ps. We compare the initial PPP spectra for both pump-push delays to two different PP spectra (Figure 5.6): The inverted spectrum of pristine P3TEA at early time, as described above, and the spectrum of the P3TEA:SF-PDI$_2$ blend after charge separation has occurred (Δpump-probe 200 ps). Before subtracting the singlet component (Figure 5.6a) the PPP spectrum at a push delay of 200 ps roughly matches this charge PP spectrum. The PPP signal at short push delays of 0.2 ps is similar to a linear combination of the charge PP spectrum and the singlet annihilation component.

After subtracting this singlet component (Figure 5.6b), the initial PPP signal matches the charge PP signal very well, both at short (0.2 ps) and long (200 ps) push delays. The PPP signal is of the same sign as the PP signal, suggesting that additional charges are generated by the push. Thus, a possible explanation of this initial component is that the push creates a temporary charge population by dissociating singlet excitons on the polymer. However, since there is no energy barrier, these charges recombine within 1 - 2 ps, explaining the decay of the initial component. Additionally, the longer-lived component could at least partially be explained by recombining charges that form triplets instead of singlets, or form singlets of higher energy that annihilate.

### 5.1.3 Features in P3TEA:SF-PDI$_2$ Blend

**Long push-probe delays**

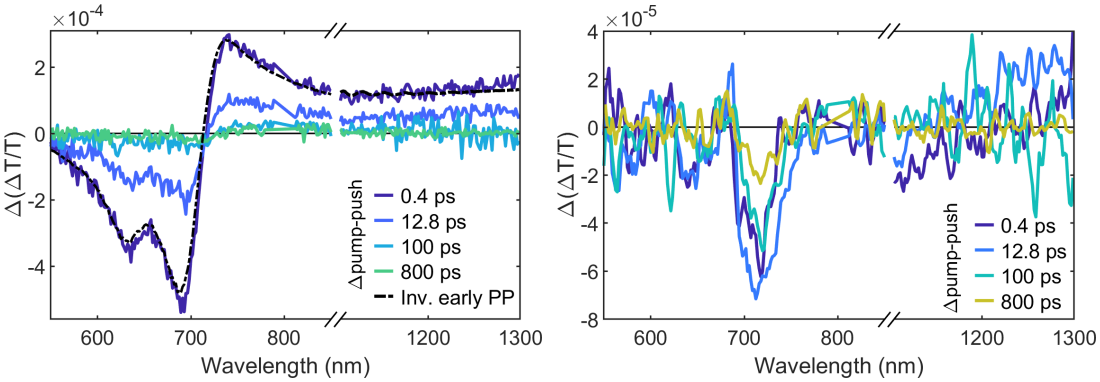


(a) Before subtraction (b) After subtracting singlet component

Figure 5.7: PPP spectra of P3TEA:SF-PDI$_2$ long after the push (Δpush-probe 7 - 8 ps). Before the subtraction (a) the spectra are very similar to the inverted pump-probe signal (black dashed line), indicating an overall reduction in PP signal due to singlet annihilation. After subtracting this component (b) there is almost no signal left.

We now turn to the P3TEA:SF-PDI$_2$ blend to study how the presence of charges changes the PPP spectra. We again start by analysing the spectra long after the push (integrating over push-probe delays of 7 - 8 ps), and comparing it to the inverted PP spectrum at early times (Figure 5.7a). The inverted PP spectrum now also contains features of charge polarons. Nevertheless, PPP and inverted PP spectra overlap well, in agreement with our explanations in the previous section. However, in this sample the signal intensity reduces when increasing the pump-push delay, disappearing almost completely at delays of 100 ps and longer. As described above, we normalise the PPP signal to the intensity of the PP PIA at the wavelength of the push. In this blend charge generation occurs and the PIA has contributions of both singlets and charges. This means that in this case we observe a signal that depends on the singlet population and normalise it by the combined population density of singlets and charges. Thus, if the proportion of singlets in the overall population is reduced, the signal reduces as well.

We have already studied the dissociation of singlets with PP spectroscopy and aim to gain further insights by using PPP spectroscopy. Therefore, we again subtract the singlet annihilation component from the PPP signal. The resulting spectra at long push probe delays are not completely flat, there are still features visible (Figure 5.7b). This adds further uncertainty in choosing the factor $\alpha < 1$ with which we multiply the inverted PP spectrum before subtracting it, beyond the uncertainty due to noise discussed in the previous section. Since we cannot completely cancel out the signal at all wavelengths, we chose to minimise the signal in the region from 850 - 950 nm.

### Short push-probe delays

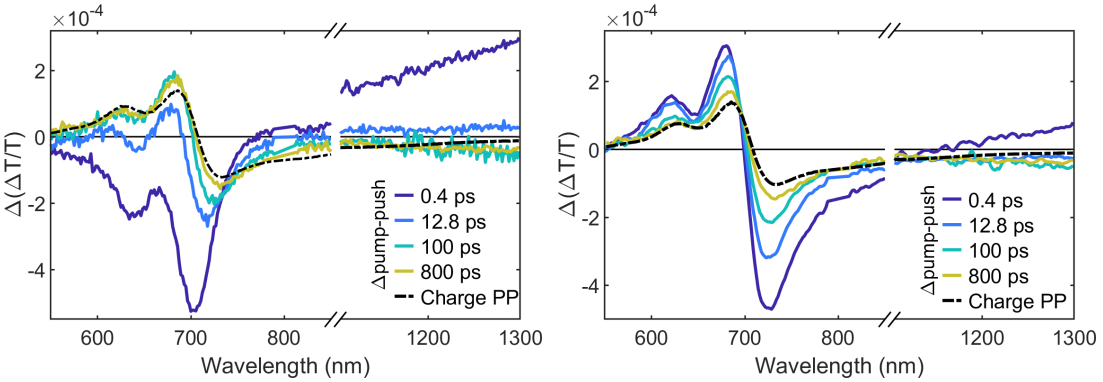


(a) Before subtraction (b) After subtracting singlet component

Figure 5.8: PPP spectra of P3TEA:SF-PDI$_2$ shortly after the push (Δpush-probe 0.2 - 0.5 ps) at various pump-push delays. Before the subtraction (a) the spectra at short pump-push delays are dominated by the singlet annihilation component; at long pump-push delays they are very similar to the pump-probe signal of separated charges (dashed line). After subtracting the annihilation component (b) all spectra are similar.

We continue our analysis with the PPP signal directly after the push (Δpush-probe = 0.2 - 0.5 ps) at pump-push delays from 0.4 - 800 ps (Figure 5.8). Before subtraction of the singlet component (Figure 5.8a) the signal is very similar to the initial signal in the pure P3TEA film. At short pump-push delays, the spectrum is dominated by the inverted PP signal. At long push-probe delays ($>$ 100 ps) the signal is similar to the PP signal of charges.

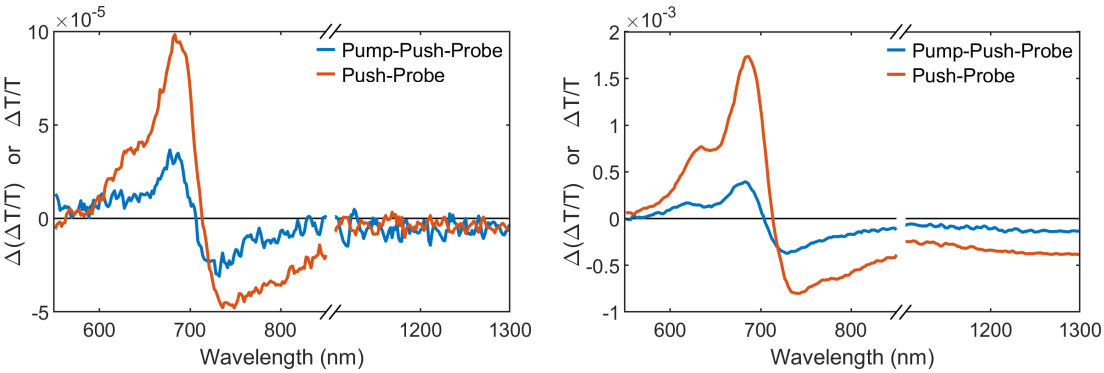


(a) 300 $\mu$W push (b) 3600 $\mu$W push

Figure 5.9: Comparison of PPP and push-probe spectra of P3TEA:SF-PDI$_2$ shortly after the push ($\Delta$push-probe 0.5 - 0.6 ps) at different fluences. The push delay is 200 ps.

If we subtract the singlet annihilation component (Figure 5.8b), we again find that the shape of the initial response does not change significantly when increasing the push delay. Interestingly, the intensity of the signal does change in the blend, where it did not change in the pure material. This suggests that at least part of the signal is caused by an interaction of the push with the singlet population. As described above, in this case we would expect a diminishing signal as the proportion of singlets decreases. However, in contrast to the singlet annihilation component, this initial response does not reduce to approximately zero but remains at roughly half its maximum intensity even at push delays of more than 100 ps. A possible explanation for this is that part of the signal is caused by an interaction of the push with the charge population. Another possibility is that this signal originates from two-photon absorption, where the push is directly exciting higher energy states that quickly form charges.

To investigate potential two-photon absorption, we measured the PPP spectra with a push delay of 200 ps at different fluences. We then compared them to the push-probe spectra, where the pump is absent and we are measuring a normal PP signal with the push pulse acting as a below-bandgap pump (Figure 5.9). We find that the ratio between the intensity of the PPP signal and the push-probe signal does not depend on the push fluence. If the push-probe signal increases, the PPP signal shortly after the push increases by the same factor. At this long

push-delay (200 ps) the initial signal is therefore likely to be dominated by a two-photon signal leaking into the PPP spectra.

To summarise, the PPP signal at short push-probe delays contains two components: Part of the signal is caused by to two-photon absorption, the other part is caused by the generation of a temporary charge population from an interaction of the push with singlet excitons, especially at short push delays.

### Intermediate push-probe delays

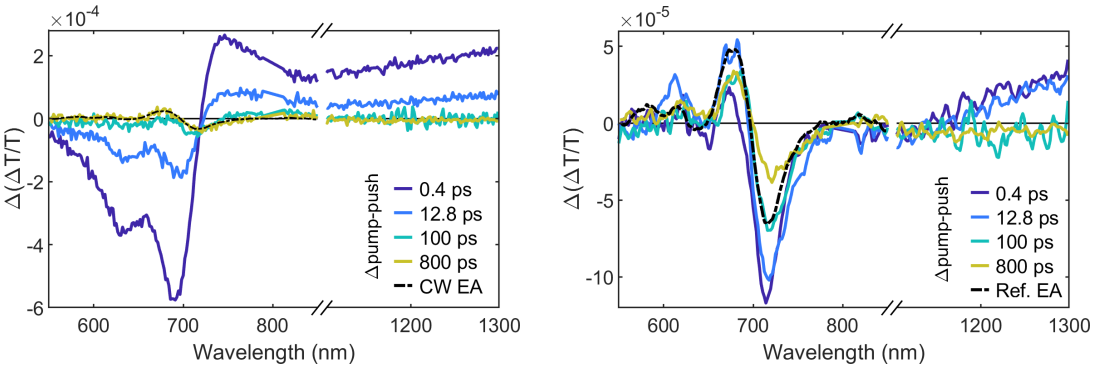


(a) Before subtraction (b) After subtracting singlet component

Figure 5.10: PPP spectra of P3TEA:SF-PDI$_2$ at intermediate times after the push (Δpush-probe 2 - 5 ps) at various pump-push delays. Before the subtraction (a) the spectra at short pump-push delays are dominated by the singlet annihilation component; the spectra at short pump-push delays are very similar to the electroabsorption signal measured in a device (black dashed line), indicating that the push leads to an increased charge separation. After subtracting the annihilation component (b) all spectra are similar.

Lastly, we analyse the signal at intermediate push-probe delays (2 - 5 ps), after the initial charge-like component has disappeared (Figure 5.10). At short push delays the signal is dominated by the singlet annihilation component (Figure 5.10a). At long push delays a new feature appears, which matches the EA spectrum we measured on a device based on the same film (black line in Figure 5.10a). When we subtract the singlet annihilation component (Figure 5.10b) this EA feature becomes more clearly visible at all push delays.

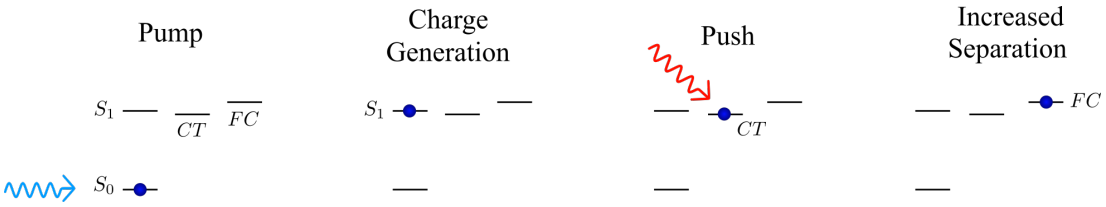


Figure 5.11: Origin of the EA component of the Pump-Push-Probe signal: If the push arrives after charge generation has occurred, and is absorbed by coulombically bound charges ($CT$ states), it can lead to increased charge separation and create free charges ($FC$).

Since this signal is crucial for the arguments in the remainder of this chapter, we will briefly repeat the discussion of the different EA signals from Section 3.3.4. In the previous chapter we described how the PP-EA signal is caused by separated charges. These free charges are formed via the normal process of exciton dissociation, in the same way as during solar cell operation. The PPP-EA signal has a different origin. In this data we compare the *push off* PP data to the *push on* PP data. Observing an EA signal is therefore indicative of additional free charges created by the push. The push is tuned to be absorbed by CTE states and it has been shown previously that electron-hole separation can increase when bound charges absorb the push [98, 108]. This can be observed as an additional EA signal [38, 98] (Figure 5.11). Once the carriers have separated to free charges, the push does not create an additional EA response. The EA signal is caused by randomly orientated dipoles from different electron hole pairs at the interface. If these electron hole pairs separate, the volume that is affected by their field increases, strengthening the EA signal. However, once the distance between electron and hole is in the same order of magnitude as the distance between different electron-hole pairs, their fields start to overlap. Since the orientation of the dipoles created by the electron-hole pairs is random, the net-field is approximately zero if their fields overlap sufficiently. Any further separation of these charges by the push therefore does not cause an EA response. Therefore, by tracking the intensity of this signal, we can monitor the amount of bound charges present at the heterojunctions.

To rule out a significant influence of two-photon absorption on the EA component, we again compare the PPP signal to the push-probe signal at different push

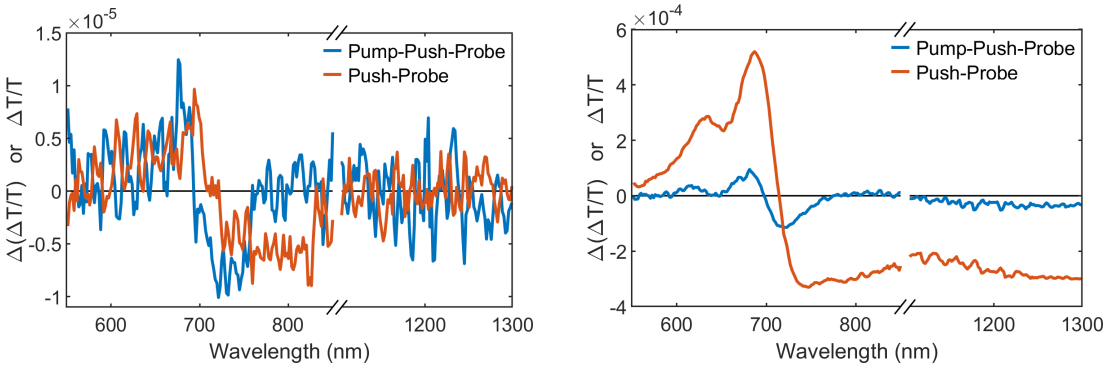


(a) 300 $\mu$W push (b) 3600 $\mu$W push

Figure 5.12: Comparison of PPP and push-probe spectra of P3TEA:SF-PDI$_2$ at intermediate times after the push ($\Delta$push-probe 0.5 - 0.6 ps) at different fluences. The push delay is 200 ps. The signals scale very differently with the push fluence, indicating that they have different origins.

intensities and the same push-probe delay (Figure 5.12). This time we observe a clear difference in the fluence dependence of the two signals: the push-probe (two-photon absorption) signal increases drastically with increasing push power, while the PPP signal only shows a modest increase. This indicates that there is no strong influence of two-photon absorption on the PPP signal.

In conclusion, by analysing the PPP spectra of pristine P3TEA and P3TEA:SF-PDI$_2$ and comparing it with PP spectra and EA spectra measured on a device, we have identified the three main components contributing to the PPP signal in these materials:

- a signal that matches the inverted singlet PP spectrum, caused by singlet-singlet annihilation (dominant at $\Delta$push-probe $> 7$ ps),
- a signal that matches the charge PP spectrum, caused by temporary dissociation of singlets and two-photon absorption, (dominant at $\Delta$push-probe $< 1$ ps), and
- a signal that matches the device EA spectrum, caused by an increased separation of bound charges (strongest at $\Delta$push-probe 2-5 ps).

In the next section we will use these insights to investigate the dissociation of CTE states.

## 5.2 Probing the CTE Population

### 5.2.1 Observing the Equilibrium of Free Charges and CTE States

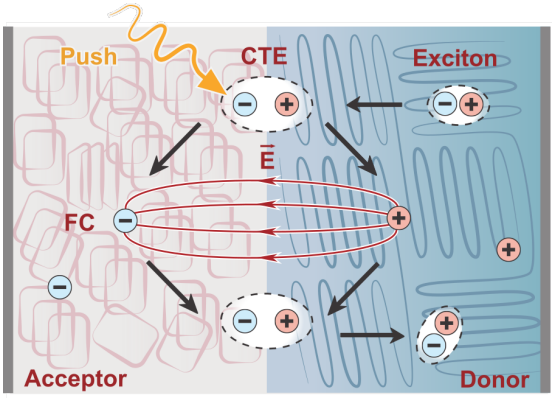


Figure 5.13: Effects of the push on CTE states at the heterojunction. The push increases the separation of bound charges, resulting in an EA signal due to the electric field between electron and hole. The charges can recombine and reform singlets. *Figure by Dr Phillip Chow, used with permission.*

In Chapter 4 we described how we studied the spatial separation of carriers via growth of the EA signal in the PP data. This PP-EA signal increases when charges separate, but does not allow us to investigate the population of bound charges at the interfaces (CTE states). In contrast, the PPP-EA signal discussed in the previous section is proportional to the CTE population, complementing the measurements discussed in Chapter 4.

Figure 5.14 shows the PPP response for several pump-push delay times, each integrated over push-probe delays of 2 - 5 ps. To reveal the effect of the push pulse on the CTE states, we have subtracted the 'annihilation' component resulting from exciton absorption, as described above. The PPP spectrum near the band edge ($\sim$ 700 nm) matches the quasi-steady-state EA response measured in a diode structure (black line in Figure 5.14a). As described in the previous section, by tracking the strength of this PPP-EA response we are able to monitor the population of Coulombically-bound CTEs at the heterojunctions (Figure 5.14b).

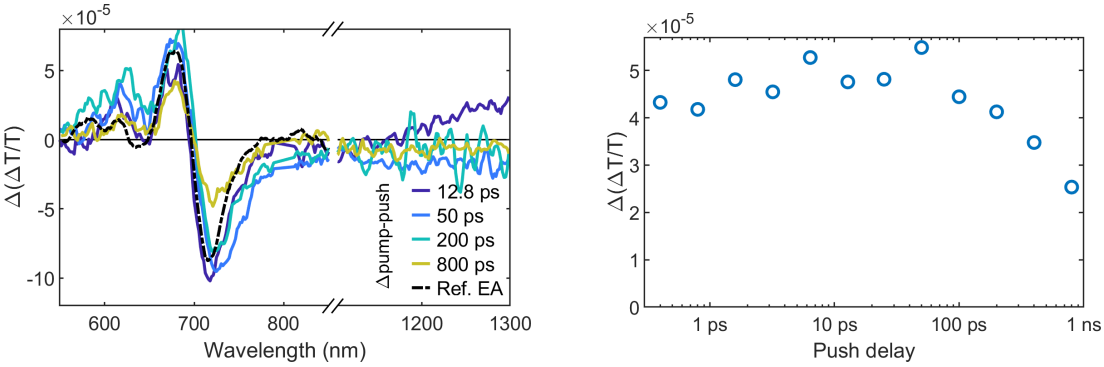


(a) PPP spectra

(b) Kinetics of PPP signal

Figure 5.14: Tracking the CTE population: PPP spectra (a) and kinetics (b) of P3TEA:SF-PDI$_2$ after charge generation.

The PPP-EA signal is already present at early times, which agrees with the evidence from the PP data that the initial charge generation occurs very quickly. Between 0.4 ps and 10 - 50 ps the signal rises by about 20 - 25%, suggesting that the proportion of CTE states further increases. From the PP data we inferred that free charges are formed on a similar timescale, which would decrease the proportion of CTE states. However, we also found evidence of a slow component of the charge generation process on a timescale that matches the rise of the PPP-EA signal. Thus, one consistent explanation of these observations is the following: A proportion of excitons either dissociates within a few tens of picoseconds, or hybridises with CTE states. In the following 10 - 50 ps CTE states separate into free charges while simultaneously new CTE states are formed via the slow exciton dissociation component, with the former process dominating slightly (Figure 5.15).

From about 50 ps onwards we observe a decrease in the PPP-EA signal. This suggests a decrease in CTE population, indicating that charges separate faster than they are formed. However, the signal does not fall to zero; approximately half of the initial signal is still present at 800 ps. In the PP data presented in the previous chapter we do not observe a growth of the PP EA signal beyond 200 ps, indicating that the population of free charges does not substantially increase beyond this point.

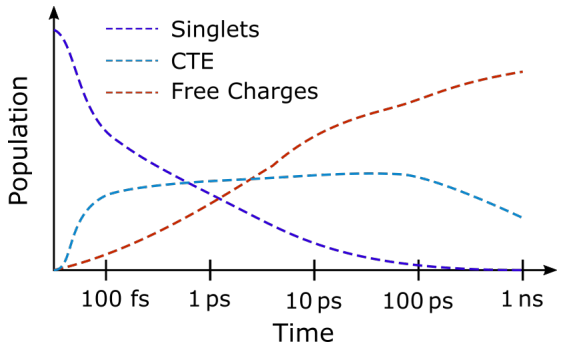


Figure 5.15: Summary of population dynamics in P3TEA:SF-PDI$_2$ (assuming no hybridisation): A significant proportion of singlets dissociates within 100 fs, forming CTE states. Over the following 10 - 100 ps these CTE states separate into free charges while CTE states are re-formed from free charges and newly formed from singlet states diffusing to the interface. On the timescale beyond 100 ps the system slowly moves towards a greater proportion of free charges, as the remaining CTE states separate.

An important consideration is that free charge generation is extremely efficient in this blend, Liu et al. measured a maximum external quantum efficiency (photo-generated electrons per incident photons) of $\approx 60\,\%$ and an internal quantum efficiency (photo-generated electrons per *absorbed* photons) of $\approx 90\,\%$ [66]. Thus, the CTE population associated with the long-term PPP EA signal does eventually separate to free charges. We have noted in the previous chapter that the slow charge separation we observe occurs from thermalised CTEs, which will also be the states populated via bimolecular encounters of free electrons and holes. We therefore consider that this long-lived PPP signal arises from CTEs formed at long-timescales via bimolecular charge encounters. Since these are the same states from which the charges have separated previously, they can separate again. Thus, our observations point towards the build-up of a quasi-equilibrium between free charges and CTEs, in agreement with previous suggestions in the literature [46, 118].

We note that we normalise the PPP spectra by the intensity of the PP PIA near the push wavelength at the time when the push arrives. Thus, we are compensating for a change in the overall population density. Changes in the PPP response plotted here therefore represent relative changes in the population den-

sities. Tracking the relative CTE population after the initial charge separation has occurred, we find that the population of bound CTE states decreases by only 10 - 20 % by 200 ps (Figure 5.14b). This suggests that within these systems the quasi-equilibrium favours the bound CTE states in the absence of charge extraction, i.e. open circuit conditions. Without a thermally-activated charge separation channel (which we observe both after initial photoexcitation and following bimolecular charge encounters), this would lead to poor photovoltaic quantum efficiencies.

### 5.2.2 Temperature Dependence of CTE Population

To complement our studies of the temperature dependence of the PP signal of separated charges, we measured the influence of decreasing the sample temperature on the evolution of PPP spectra (Figure 5.16). In these measurements we only measured push-probe delays up to 0.6 ps, which makes it impossible to subtract the contribution of the singlet population to the PPP signal. Therefore, Figure 5.16 shows the original spectra, containing all components of the signal discussed in Section 5.1. In particular, the spectra contain a small contribution from the component attributed to short-lived charges generated by the push, since we do not have data from the push-probe delays at which this component has disappeared. However, the spectra were taken at push-probe delays integrated from 0.45 - 0.5 ps, at which this component is not dominant any more.

The PPP response at all temperatures is similar to the room temperature data discussed before (Figure 5.8a): At short push delays the spectra are similar to the inverted PP spectra, probing the singlet population; at long push delays the spectra are similar to the EA signal measured at a device, probing the CTE population. Changes in temperature affect these two components very differently. The singlet response is not affected significantly, changes in signal intensity between measurements can most likely be attributed to slight changes in alignment. In contrast, the EA response strongly increases with decreasing temperature. The derivative-like signal at long push delays is more than four times stronger at temperatures of 16 K than at 290 K.

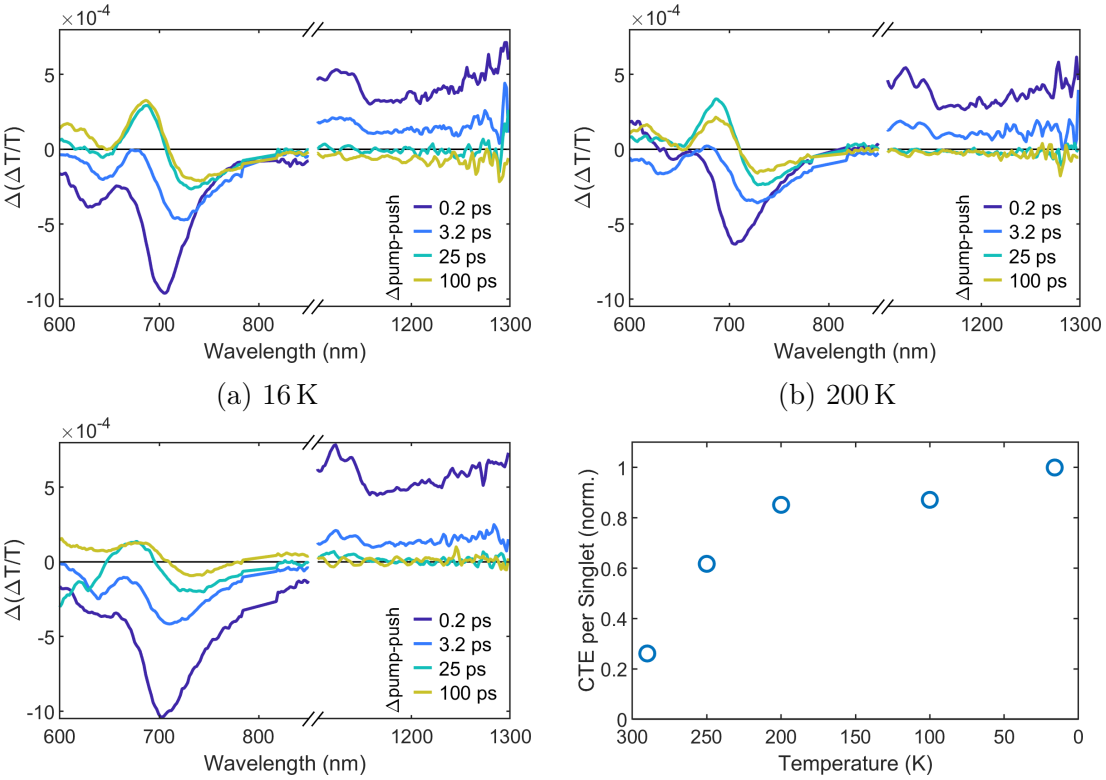


(a) 16 K (b) 200 K

(c) 290 K (d) Overview of CTE population

Figure 5.16: PPP spectra and kinetics of P3TEASF-$PDI_2$ at different temperatures. All spectra were taken at a Push-Probe delay of 0.4 - 0.5 ps. Data points in (d) were obtained by averaging the absolute signal intensity from 660 - 760 nm (EA), and dividing it by the the signal in the 1200 - 1280 nm range at a push delay of 0.8 ps (singlets).

For a more detailed analysis of how the sample temperature affects the CTE population, for each temperature we normalised the PPP-EA signal (absolute signal from 660 - 760 nm averaged over push delays of 50 and 100 ps) by the singlet PPP signal (1200 - 1280 nm at a push delay of 0.8 ps) (Figure 5.16d). At temperatures below 200 K the CTE population is much larger than at room temperature. Thus, at lower temperatures the equilibrium between free charges and CTE states is strongly shifted towards the CTE population. This is likely due to changes in the interplay of the charge separation and CTE reformation processes, both of which can be sensitive to changes in the thermal energy available.

The strong influence of temperature on the CTE population is further evidence of the endothermic nature of charge separation in non-fullerene systems. However, our method provides only a rough estimate of the ratio of CTE population to initial singlet population that depends on the wavelength and time ranges selected for integration. While this allows us to infer a qualitative trend, the range of uncertainty of the extracted values is large.

### 5.2.3 Regeneration of Singlets

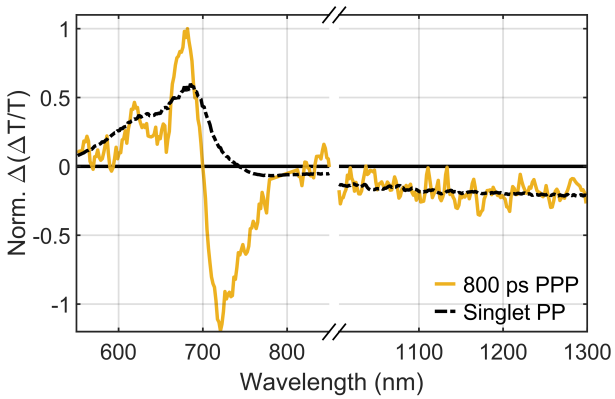


Figure 5.17: Regeneration of singlets by the push: The NIR region of PPP spectra of P3TEA:SF-PDI$_2$ at long push delays (yellow line) matches the PP signal of singlets in P3TEA (black line).

In addition to the signal at the band edge, the PPP spectrum contains a response in the NIR between 1100 and 1300 nm (Figure 5.17). At longer push delays ($>50$ ps), this NIR response is negative, indicating that the push leads to the formation of states which absorb in this region. This absorption is not consistent with the absorption of charges (electrons or hole polarons) in this system, but matches the absorption of singlet excitons in the NIR (black line in Figure 5.17). This suggests that, in addition to separating CTEs to free charges, the push pulse can regenerate singlet excitons from the CTE states.

### 5.2.4 Comparison to Other Blends

For P3TEA:FTTB-PDI4, P3TAE:SF-$PDI_2$ and PffBT2T-TT:O-IDTBR, we also observe a long-lived PPP spectral response with derivative line-shape near the band edge that we attribute to CTEs at the donor-acceptor heterojunction of these blends (see Appendix Figure A.8). These CTE signals do not fall to zero beyond the free charge generation timescale (up to 800 ps; see Appendix Figure A.9), in agreement with our observations for the P3TEA:SF-$PDI_2$ blend of a quasi-equilibrium between CTEs and free charges. Overall, we observe very similar PP and PPP results in the four efficient non-fullerene blends with small photovoltage losses despite their different structural motifs, thus showing that the slow (hundreds of ps) yet efficient endothermic charge separation process is general to non-fullerene systems with near zero $E_{S1}$–$E_{CTE}$ offsets.

## 5.3 Conclusions & Outlook

To summarise, using PPP spectroscopy we were able to monitor the CTE population over a range of 0.4 - 800 ps after the initial excitation. This data suggests that approximately half of the initial population is still present at 800 ps. Our PP data discussed in the previous chapter indicated that most of the charge separation occurs before this time. Thus, we concluded that we observe an equilibrium between thermally activated charge separation and electron-hole encounters that reform thermally relaxed CTE states. Our temperature dependent measurements support this claim: with decreasing temperature we observe a decreasing PP signal of separated charges and an increasing PPP signal of bound CTE states.

We also found that the push can regenerate singlets from these relaxed CTE states, further supporting our conclusion in the previous chapter that electron-hole encounters can lead to regeneration of singlets. Taken together, these results indicate that the thermodynamic equilibrium exists between all three excited states: singlet excitons, CTEs, and free charges.

For conventional fullerene-based OSCs it has been widely noted that the rate of bimolecular recombination is suppressed compared to Langevin recombination models, and a number of explanations such as phase segregation of electrons and

holes have been put forward to explain this [46, 76] (see Section 2.2.4 for details). However, in these systems electron-hole encounters do not regenerate singlet excitons to any significant extent as there is a substantial energetic offset between the relaxed CTEs (which are formed via recombination) and the singlet excitons. The energetic offset in turn is required to drive rapid charge separation, as separation of the relaxed CTEs is not efficient. This is also due to the high degree of electronic disorder found in conventional fullerene blends (Urbach energy $\geq 40\,\mathrm{meV}$) which traps the CTEs in low energy sites from which they cannot escape to form free charges or regenerate singlet excitons [38, 84, 119]. Thus the $\mathrm{EQE_{EL}}$ values for fullerene-based OSCs are very low ($\leq 10^{-6}$ typically, as measured here for P3TEA:PCBM system). In contrast, the results presented here indicate that in the non-fullerene systems a significant fraction of the charge separation occurs over hundreds of picoseconds from thermalised CTEs via thermal activation. These same CTEs are repopulated via charge encounters allowing for the regeneration of singlet excitons, which consequently establishes an equilibrium between the singlet excitons, CTEs and free charges. This much more efficient regeneration of the singlet excitons enables higher $\mathrm{EQE_{EL}}$ ( $\geq 10^{-4}$ for the non-fullerene system [22, 37, 120]) and hence lower non-radiative voltage losses. Importantly, the regenerated singlet excitons can then once again form CTEs which dissociate to free charge.

As mentioned earlier, our analysis of the PPP-EA signal involves manually choosing several parameters, such as the amount of inverted PP signal we subtract as the singlet-annihilation component and the time and wavelength ranges we integrate to extract the CTE kinetics. Our results should therefore be interpreted with caution. However, we have combined evidence from a range of spectroscopic methods and several of our results are in agreement with results and considerations reported previously. Our conclusions therefore provide important insights for future efforts to improve organic photovoltaics.

If confirmed, our results call for a shift in the way OSCs are designed and optimised. The reversible interconversion of free charges, CTEs, and singlet excitons that we observe indicates that their Gibbs free energies must be very similar. This contrasts with conventional OSC blends, where large energy offsets have been designed into systems to rapidly separate electrons and holes and prevent

their re-encounters. This lowers the Gibbs free energy of the free charges with respect to CTEs and singlet excitons, thus introducing irreversibility into the system and preventing recombination in a manner similar to natural light harvesting complexes. In both natural light harvesting complexes and conventional OSC blends this results in high quantum efficiencies but a large photovoltage loss. However, our results suggest that in non-fullerene blends with low photovoltage loss endothermic charge separation of CTEs occurs on long timescales ($>100\,\mathrm{ps}$) via thermal activation, removing the need for energy offsets to engineer rapid and irreversible charge separation. This removes the need for a large loss of free energy to obtain high quantum efficiencies and allows for minimal voltage loss. This brings non-fullerene OSCs into the same mode of operation as inorganic solar cells, where encounters of free carriers do not lead to recombination (in the absence of non-radiative decay events associated with defect states) and the free energy of the photogenerated electron hole pair and separated electron and hole are very close. Our results indicate that OSCs are not fundamentally limited by the Coulomb energies that bind excitons and CTEs, due to the possibility of undergoing thermally activated charge separation. In this case future OSCs should be designed to remove all irreversible processes and energy offsets, with significant efficiency gains being possible by reducing non-radiative losses in recombination. This could be achieved for example via the use of high PLQE donor and acceptor materials such that reformation of excitons via bimolecular electron-hole encounters leads to efficient emission. It is also now time to address issues such as quenching of PL at charge collection electrodes, much investigated for lead halide perovskite photovoltaic systems but not for OSCs. This could enable OSCs to achieve high charge generation efficiencies with small photovoltage losses that are comparable to non-excitonic solar cells based on inorganic semiconductors [33, 35].

# Chapter 6

# Charge Dynamics in PBDB-T:ITIC

In this chapter we present our spectroscopic studies of another non-fullerene OPV system: the PBDB-T:ITIC blend. This system was used as the active layer in the first highly efficient polymer:non-fullerene solar cell with efficiencies surpassing those of fullerene based solar cells [8]. The first section focusses on PP measurements of charge generation. We show how in these samples charges can be formed via hole transfer from the acceptor to the donor, or via electron transfer from the donor to the acceptor. In the second section we investigate how these photogenerated charges recombine. The third section then describes our attempts to probe the CTE population using PPP spectroscopy.

*This chapter is the result of a collaboration with Associate Professor Feng Gao and co-workers from Linköping University, who provided the samples for this project. The content is adapted from the resulting publication draft* [121].

## 6.1 Properties of Studied Materials

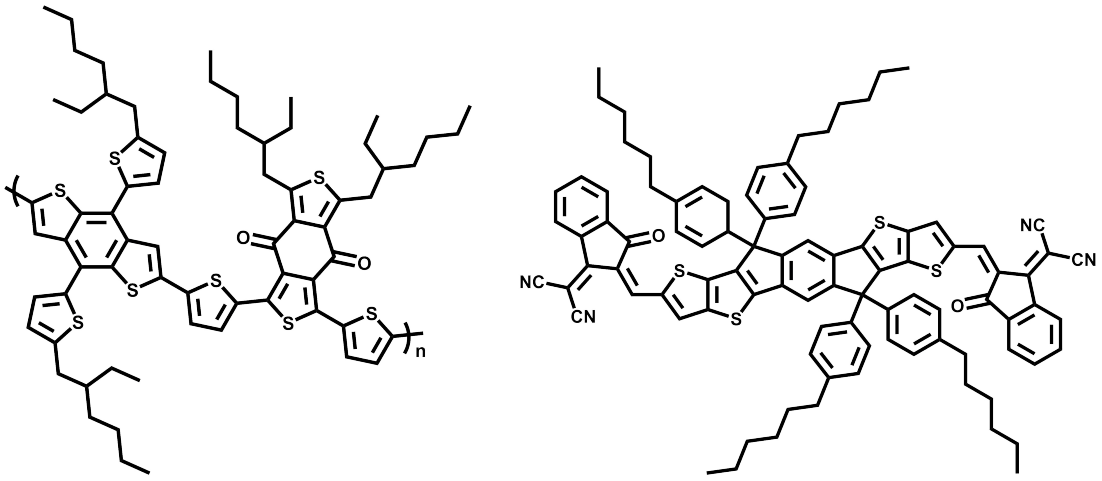


(a) Electron Donor: PBDB-T (b) Electron Acceptor: ITIC

Figure 6.1: Chemical structures of the electron donor polymer PBDB-T and the electron acceptor molecule ITIC.

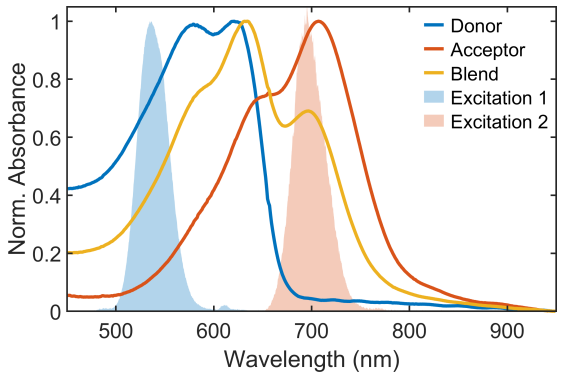


Figure 6.2: Absorbance spectra of pristine PBDB-T (donor), pristine ITIC (acceptor), and the PBDB-T:ITIC blend. Also shown are the spectra of the exciting laser pulses, showing selective excitation.

The material we investigated in this study is a bulk heterojunction of the conjugated polymer PBDB-T, acting as an electron donor, and the molecule ITIC, acting as an electron acceptor (Figure 6.1). A device based on this blend was the first organic solar cell to reach a PCE above 10 %, leading to a strong increase in research into non-fullerene acceptors [8].

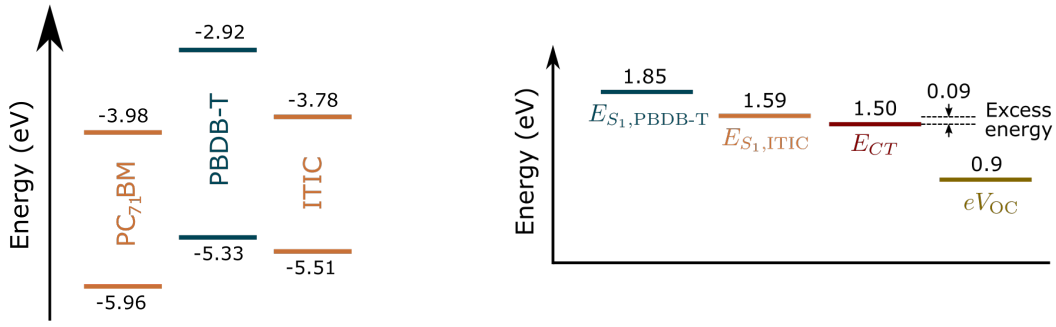


(a) HOMO & LUMO levels

(b) Excited state energies

Figure 6.3: Energy levels of PBDB-T:ITIC: (a) HOMO and LUMO levels of the individual molecules as measured via cyclic voltametry. (b) Energies of the excited states, as determined by the absorption onset ($S_1$) or the crossing point of absorption and electrolumnescience spectra ($E_{CT}$). *All values except* $E_{S_1,\text{PBDB-T}}$ *taken from Reference [8].*

To begin our characterisation of this material, we measured the absorption spectra of a pristine PBDB-T film, a pristine ITIC film, and a blend of the two components (Figure 6.2). The absorption of the blend is very similar to a linear combination of the spectra from the pure components, indicating that interface effects are weak. Based on these absorption spectra we tuned the pump pulses to selectively excite the two components of the blend. The pulse centred around 535 nm is predominantly exciting the donor molecules, the pulse centred around 700 nm is predominantly exciting the acceptor molecules (shades in Figure 6.2).

To understand the excited state dynamics in this system it is important to consider the alignment of the energy levels of donor and acceptor (Figure 6.3). Comparing fullerene and non-fullerene acceptor, the HOMO energy of ITIC is about 0.5 eV higher than the HOMO energy of PCBM (Figure 6.3a). This lowers the bandgap of the material, allowing it to absorb photons of lower energy. Importantly, reducing the difference between the HOMO levels of donor and acceptor reduces the 'excess energy' available for hole transfer. For this system the difference between the singlet energy $S_1$ of the electron acceptor and the energy of the CTE state was measured to be as low as 90 meV [8] (Figure 6.3b). Nevertheless, the hole transfer is efficient, with external quantum efficiencies around 75 % [8].

## 6.2 Identifying Components of PP Spectra

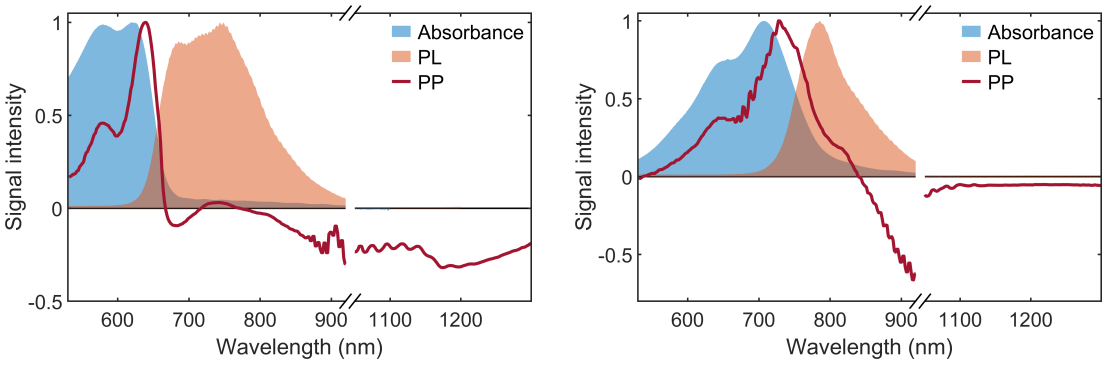


(a) PBDB-T (b) ITIC

Figure 6.4: Comparison of PP spectra at 0.1 ps of pristine PBDB-T (a) and pristine ITIC (b) with absorbance and PL data. Ground state bleach and stimulated emission spectra can be identified, as well as destinct photoinduced absorption features.

To identify the characteristic PP features of the singlet excitons, we compare the PP spectrum of PBDB-T to the steady-state absorption and PL data of the same film (Figure 6.4a). We can distinguish the following components:

- **GSB:** a positive feature from below 530 - 660 nm, overlapping with the absorption spectrum,
- **SE:** a positive feature from 680 - 880 nm, overlapping with the PL spectrum, and
- **PIA:** a broad negative feature from 660 - 1300 nm, with a minimum around 1200 nm, overlapping with the other two features.

A similar comparison for ITIC (Figure 6.4b) shows a distinct PIA (negative feature from 840 - 1400 nm) and overlapping GSB and SE (positive features from 540 - 760 nm and 660 - 860 nm).

To identify the features of hole polarons on the donor, we also measured a blend of PBDB-T and PCBM (Figure 6.5). Since PCBM has only a weak PP response in this wavelength region (Appendix Figure B.1), spectral differences

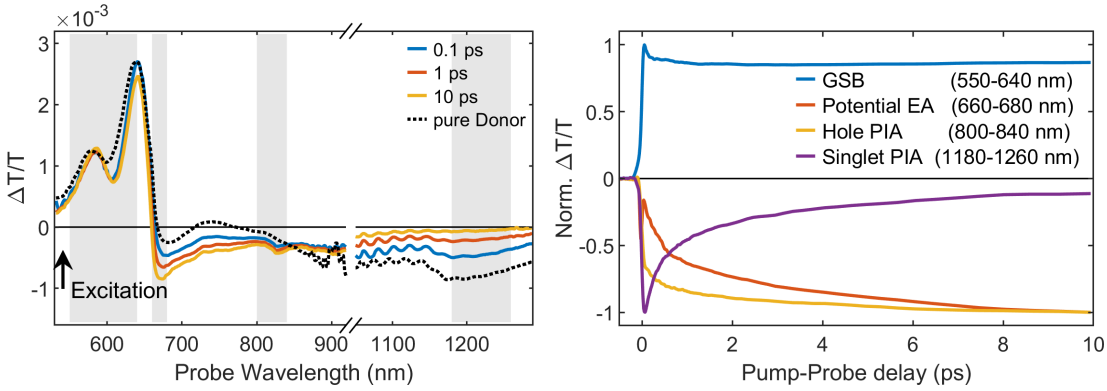


(a) Spectra (b) Kinetics

Figure 6.5: PP spectra (a) and kinetics (b) of the PBDB-T:PCBM blend.

between this blend and the pristine PBDB-T film (black line in Figure 6.5a) can be attributed to the donor polaron. In this blend, the singlet exciton PIA from 1050 - 1400 nm almost completely disappears within the first 10 ps. Simultaneously, a new negative feature from 680 - 920 nm appears, with minima at 690 nm and 820 nm, which is partially overlapping with the PIA of the exciton around 900 nm. The GSB does not differ much from the GSB measured in the pure PBDB-T film, as expected. Since efficient photovoltaic devices have been fabricated with this material [8], we expect charge transfer to occur. The negative feature from 690 - 920 nm, that increases while the singlet PIA around 1200 nm decreases, can therefore be attributed to hole polarons.

The negative feature on the red edge of the GSB could also be an electroabsorption (EA) signal, caused by the microscopic electric field of separated charges (see Chapter 3.3.4). Comparing the kinetic of this feature (red line in Figure 6.5b, generated by integrating the spectrum from 660 - 680 nm) and the kinetic of the PIA at longer wavelengths (yellow line, integrated from 800 - 840 nm) shows that the potential EA feature has a slower rise during the first picosecond. The relative difference between these lines would correspond to the proportion of charges that have not fully separated yet. However, it is difficult to draw conclusions from this, since the feature is overlapping with the SE from the PBDB-T singlet exciton.

To summarise, we have identified the following species and their characteristic features:

- **Donor (PBDB-T) singlet exciton:** GSB from 520 - 660 nm, SE from 700 - 840 nm, broad PIA which is strongest from 1180 to 1300 nm
- **Donor (PBDB-T) hole polaron:** GSB from 520 - 660 nm, PIA from 680 - 1000 nm
- **Acceptor (ITIC) singlet exciton:** GSB from 580 - 780 nm, SE from 720 - 850 nm, PIA from 840 - 1000 nm

Some of these features are overlapping, complicating the tracking of different species. However, the overall donor population can be easily tracked by its GSB, and the donor singlet population can be tracked via the PIA in the NIR.

## 6.3 Charge Generation

In the previous section we have analysed our PP data with the aim of assigning spectral features to the excited states in our materials. After identifying the features of singlet excitons and hole polarons on the donor, and singlet excitons on the acceptor, we now proceed by studying these populations in the donor-acceptor blend during the charge generation process.

### 6.3.1 Hole Transfer Dynamics

We first focus on the hole transfer dynamics, following selective excitation of the acceptor. Figure 6.6a shows the PP spectra of the blend at different delays after exciting the acceptor. For comparison we also reproduce the spectra described in the previous section (Figure 6.6b). The initial spectrum of the blend (0.1 ps after the pump) mainly consists of features of the acceptor singlet. The GSB of the donor singlet is also present, most likely caused by the remaining direct excitation of the donor. Another reason for the presence of this GSB at early times could be charge transfer on timescales shorter than our time-resolution. At later times we observe a simultaneous growth of the donor GSB and of the PIA

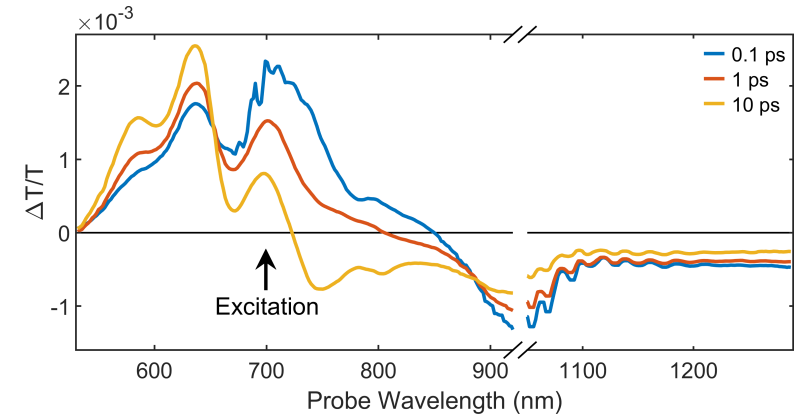


(a) PBDB-T:ITIC after exciting ITIC

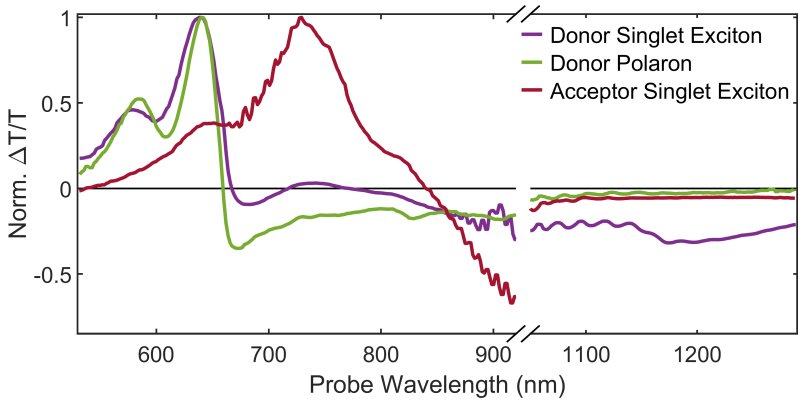


(b) Reference Spectra

Figure 6.6: Hole transfer dynamics. (a) PP spectra of PBDB-T:ITIC blend when predominantly exciting the ITIC (donor) phase (700 nm). (b) Components of the PP spectrum identified previously.

associated with charge formation on the donor. We also observe a quenching of the acceptor singlet PIA around 900 nm, but since the donor hole polaron also has a PIA in this region, there is a remaining signal in this wavelength region at late times ($>10$ ps). These spectral changes show the hole transfer from the acceptor to the donor.

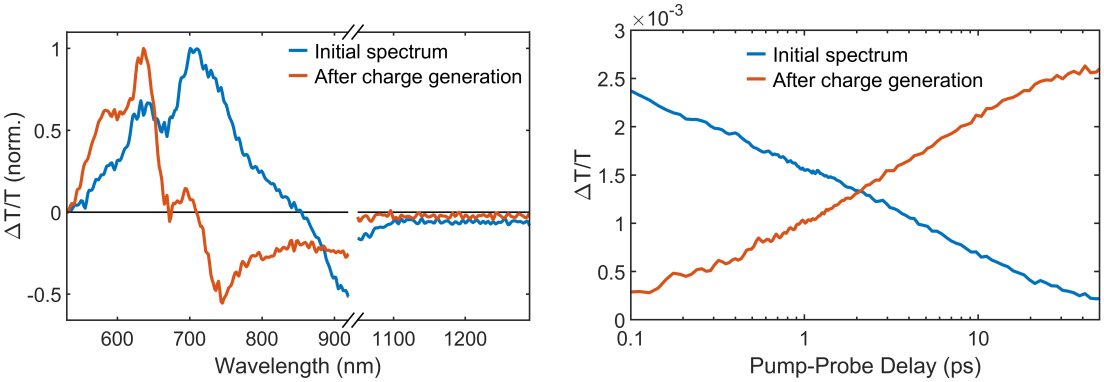


(a) Spectra (b) Kinetics

Figure 6.7: Hole transfer dynamics as extracted via the genetic algorithm.

To extract the kinetics of the hole transfer we decompose the spectral dynamics with the genetic algorithm described in Section 3.4. After running the algorithm with different parameters we can identify two main components (Figure 6.7):

- The spectrum that is dominant in the beginning (blue lines) closely resembles the spectrum of the pure acceptor. It contains GSB, SE, and PIA from the acceptor singlet exciton, as well as a smaller peak at 640 nm that matches the donor GSB.

- The spectrum that is dominant at the end ($>10$ ps) is similar to the spectrum of the donor hole polaron. It contains the the donor GSB and the hole PIA that is strongest near the GSB. However, instead of a minimum at 660 nm it has a peak at 700 nm, corresponding to the acceptor GSB. There is no positive signal between 700 - 850 nm, which would correspond to SE from the acceptor. This is expected: The spectrum of electron polarons on the acceptor will consist of the same GSB as the singlet exciton. Since polarons are not emissive, they lack the SE component.

Thus, the initial spectrum represents the state of the system before charge generation occurs, the final spectrum represents the electron- and hole-polarons. The kinetics extracted by the genetic algorithm therefore are the kinetics of the charge generation process. Most of the charges ($>75\%$) are formed within 10 ps.

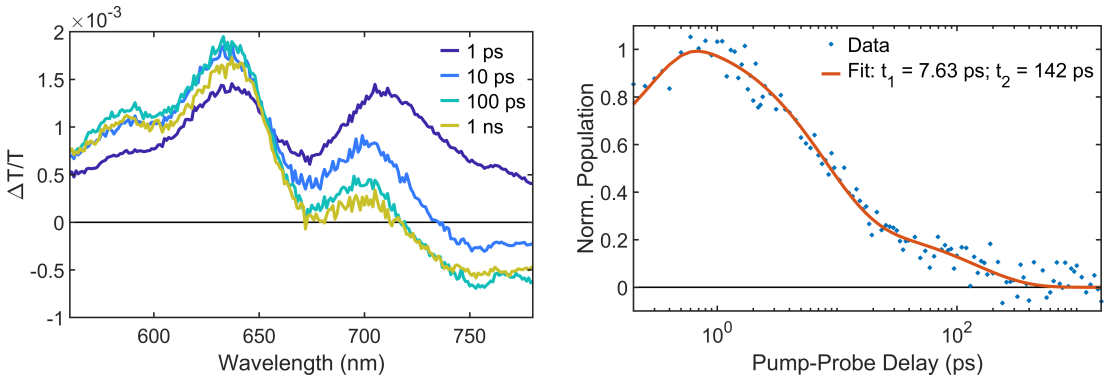


(a) Spectra (b) Kinetics of Hole Transfer

Figure 6.8: PP data of PBDB-T:ITIC on a picosecond to nanosecond timescale when exciting the acceptor molecules: (a) Spectra and (b) population dynamics of initial excited state as extracted with the genetic algorithm. Fitting a sum of exponentially modified Gaussian functions yields two characteristic decay times.

We note that the spectra and kinetics shown here are a representative output of the genetic algorithm. Multiple runs with different start parameters produced similar results. When setting the algorithm to output three species instead of two, it either produced two species that were very similar to each other in both spectra and kinetics, or it produced two species that were compensating each other (Appendix Figure B.2). This is a strong indicator that there are only two significant species present in the data.

To monitor the complete charge generation process we measured the PP signal in the picosecond to nanosecond range (Figure 6.8). To extract the charge transfer kinetics, we again decomposed the PP spectra with the genetic algorithm. The results were consistent with the dynamics described above (Appendix Figure B.3). Again, two spectral species were extracted: the initial singlet excitons and the final charge separated state, with a transition occurring on a timescale of 10 - 100 ps (Figure 6.8b).

To extract the characteristic decay times of the hole transfer, we performed a fit of a sum of exponentially modified Gaussian functions:

$$\sum f_i(x; t_0, \sigma, k_i), \tag{6.1}$$

with

$$f_i(x; t_0, \sigma, k_i) = \frac{1}{2} \exp\left(\frac{k_i}{2}(2t_0 + k_i\,\sigma^2 - 2x)\right) \operatorname{erfc}\left(\frac{t_0 + k_i\,\sigma^2 - x}{\sqrt{2}\sigma}\right),$$

where erfc() is the complementary error function, $t_0$ corresponds to the time when the pump pulse arrives, $\sigma$ is the instrument response (approximately the duration of the pump pulse), and $k_i$ are the decay constants. The exponentially modified Gaussian distribution results from a convolution of an exponential decay $e^{-k_i\,(x-t_0)}$, representing the excited state dynamics, with a Gaussian distribution $\varphi(x, \sigma, t_0)$ with standard deviation $\sigma$ and mean $t_0$, representing the instrument response. It was possible to obtain a good fit with two exponentials (Figure 6.8b). The extracted decay times $t_i = k_i^{-1}$ are 7.6 ps and 140 ps, with the initial decay dominating. This is consistent with Figures 6.6a and 6.7, which show that most of the charge generation occurs on a timescale of 10 ps. The weak slow component of the charge separation could represent diffusion of singlet excitons towards the interface.

### 6.3.2 Electron Transfer Dynamics

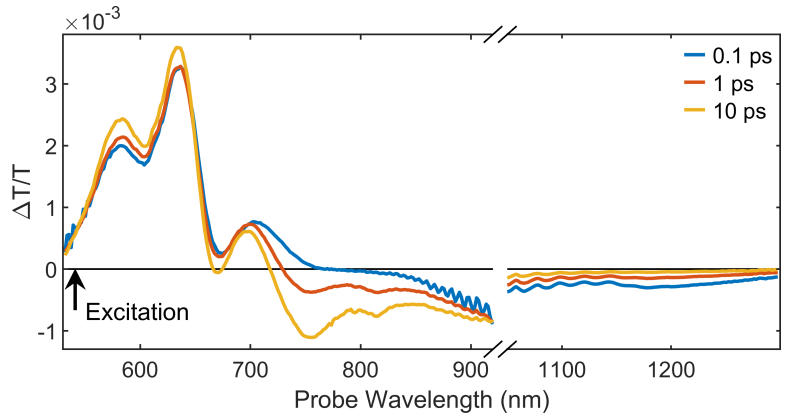


(a) PBDB-T:ITIC after exciting PBDB-T)

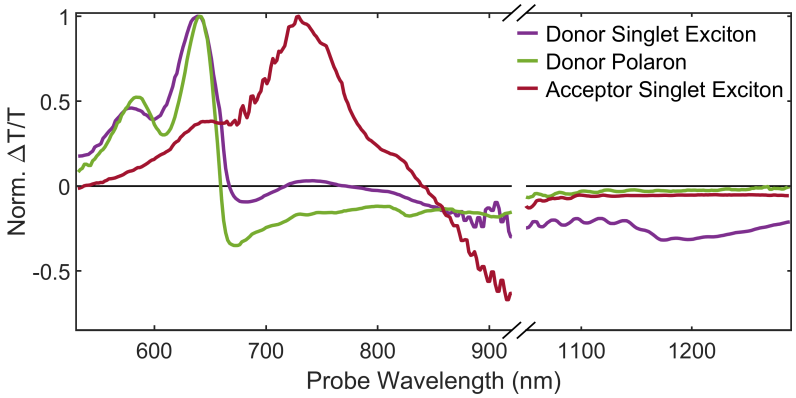


(b) Reference Spectra

Figure 6.9: Electron transfer dynamics. (a) PP spectra of PBDB-T:ITIC blend when predominantly exciting the PBDB-T (donor) phase. (b) Components of the PP spectrum identified previously.

We now turn to the electron transfer dynamics, the second process of charge generation in non-fullerene OPV systems. To investigate this process we use a pump pulse centred around 535 nm ('Excitation 1' in Figure 6.2), predominantly exciting the donor molecules. Figure 6.9a shows the resulting PP spectra. In this case the initial spectrum is dominated by the donor singlet exciton, with contributions from the acceptor singlet. The spectra at later times show a quenching of the singlet exciton features around 1100 - 1200 nm and a growth of the features

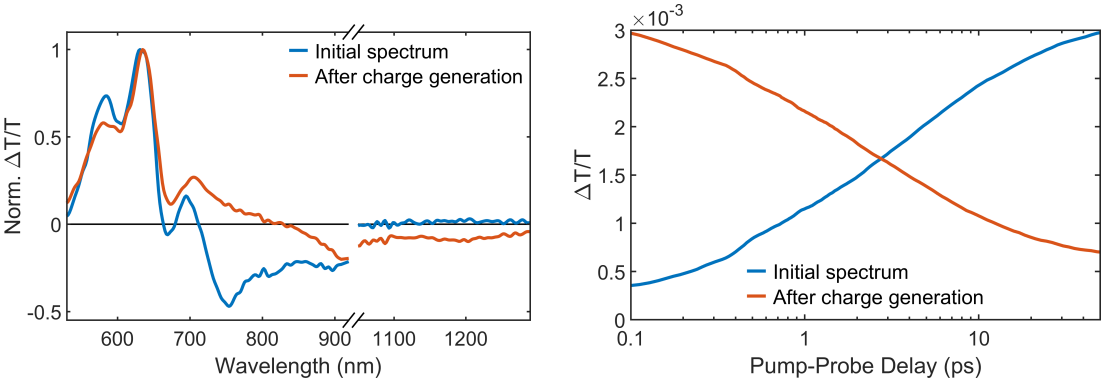


(a) Spectra (b) Kinetics

Figure 6.10: Electron transfer dynamics as extracted via the genetic algorithm.

associated with charge formation (negative signal from 720 - 920 nm). This shows that electron transfer from the donor to the acceptor is occurring on a similar timescale to the hole transfer described above (around 10 ps).

We again extracted the spectra and kinetics of the dominant populations with the genetic algorithm (Figure 6.10). The result is similar to the the result when exciting the acceptor: There is one species that corresponds to the initial state, dominated by donor singlet excitons, and one species that corresponds to charge polarons on both donor and acceptor. The timescale of this electron transfer is similar to the timescale of hole transfer discussed above: 10 ps after the pump most of the charges have transferred.

We also repeated the PP measurement in the picosecond to nanosecond range under donor excitation (Figure 6.11a). In this case the polaron PIA ($>750$ nm) does not change significantly after 10 ps. There is no evidence of a slower component of this process, as it was the case for the hole transfer. This suggests that exciton transport in the polymer is fast enough to not be a limiting factor.

To explore this further we extracted the spectra and kinetics with the genetic algorithm and fitted Equation 6.1. In this case the best fit was obtained with a single exponential (Figure 6.11b), confirming that there is no significant slow component in the electron transfer process. The extracted decay time is 9 ps.

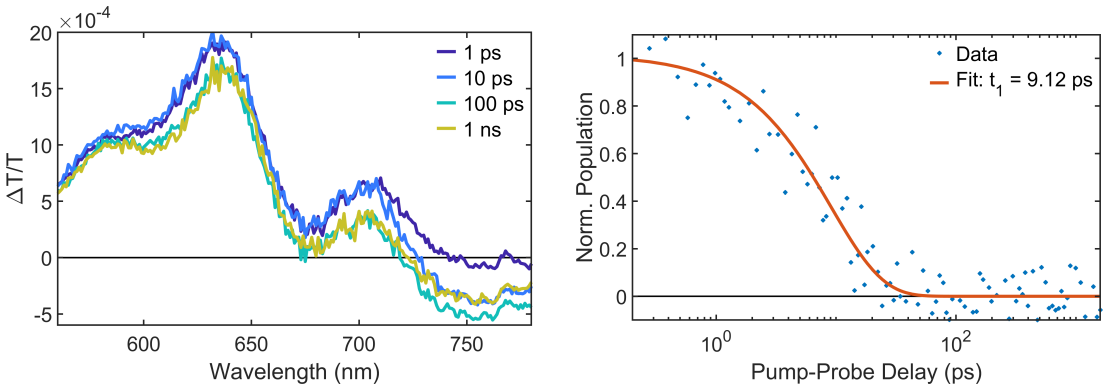


(a) Spectra (b) Kinetics of Electron Transfer

Figure 6.11: PP spectra (a) of PBDB-T:ITIC on a picosecond to nanosecond timescale when exciting the donor polymers, and fit of the kinetics extracted with the genetic algorithm (b). Most of the electron transfer occurs within 10 ps.

We note that the spectrum at 1 ns does not depend on whether we excite the donor or acceptor molecules. This is expected for efficient dissociation of excitons into charges, since after charge transfer there are only holes on the ITIC molecules and electrons on the PBDB-T. There is no evidence for the formation of other excitations before the charge separation occurs.

## 6.4 Charge Recombination Dynamics

The previous sections were concerned with the generation of charges. However, these charges can only be put to use in a solar cell if they are extracted before they recombine and relax to the ground state. Understanding the charge recombination dynamics is therefore crucial for optimising device performance. In this section we present our studies of these dynamics, focusing on fluence dependent PP measurements in the nanosecond to microsecond range.

### 6.4.1 Triplet Formation

A typical loss mechanism in OPV is the formation of triplet excitons, followed by non-radiative recombination (see Section 2.2.5). Triplet formation often occurs

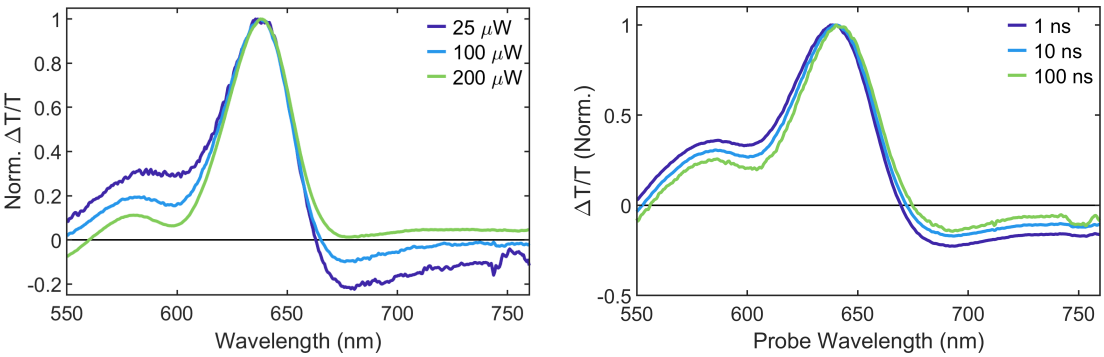


(a) Pure PBDB-T: fluence dependence (b) Doped PBDB-T: time dependence

Figure 6.12: Triplet features in PBDB-T: PP spectra of pristine PBDB-T at 10 ns (a) and PBDB-T doped with PtOEP (b). There is a fluence-dependent shift of the spectum in the pristine sample that matches the time-dependent shift of the doped sample.

via bimolecular pathways, with rates increasing at high population densities. In the case of pure PBDB-T we expect the dominant species to be singlet excitons and therefore triplet generation to occur via singlet-singlet annihilation. Consequently, measuring the signal at different excitation densities is a useful tool to learn about this process [82, 83, 122, 123]. To identify the PP features of triplets in PBDB-T, we measured the PP spectra of a pure film of this material at delays in the ns to $\mu$s range at different excitation densities (Figure 6.12a). We observe a clear difference in the spectra at 10 ns when we normalise to the main GSB signal: With increasing fluence the blue side of the GSB ($<620$ nm) becomes less positive, while the PIA on the red side ($>680$ nm) becomes less negative.

We compared this with the spectra of a film made of PBDB-T molecules doped with PtOEP. The platinum at the core of these porphyrin molecules leads to efficient intersystem crossing [124] and the generated triplets can then transfer into other molecules [125]. To isolate the effects of triplet injection into the PBDB-T molecules while avoiding any bimolecular effects we encapsulated them in a PMMA film. We then measured the PP spectra at different pump-probe delays in the nanosecond to microsecond range, allowing us to track the injection of triplets (Figure 6.12b). With increasing delay we observe an effect very similar to the one observed at increasing fluences in the pristine material: a reduction in signal on both sides of the main GSB peak.

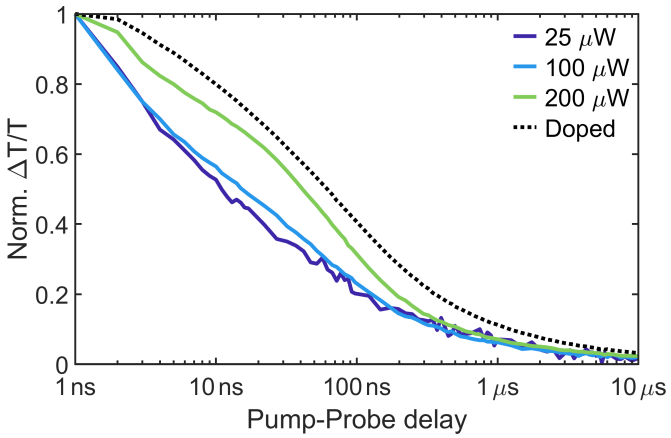


Figure 6.13: Fluence dependence of pure PBDB-T GSB decay (630 - 645 nm) in the ns to $\mu$s range. With increasing excitation fluence the the kinetic becomes similar to the GSB decay in the doped sample (dotted line).

To explore this correlation between the effects of doping and increasing excitation densities, we compare the the lifetime of the excited state population in both cases (Figure 6.13). The lifetime in the undoped sample increases with increasing fluence and becomes more similar to the doped material. Since triplets generally have longer lifetimes than singlets due to the forbidden transition to the ground state, this is consistent with the spectral changes described above. Thus, we observe similar effects in two different conditions that are likely to increase the triplet population: exciting at high fluences, and injection from a material that is known to generate triplets. We can therefore assign this change in the spectrum to triplets.

We note that this implies that a surprisingly long lifetime of part of the singlet population. Typical singlets exciton lifetimes in conjugated polymer films for organic solar cells of the order of tens to hundreds of picoseconds [126], and others have reported a singlet lifetime of 26 ps for PBDB-T [123]. However, a recent study of a pure PBDB-T film found that 10 % of the initial PL intensity was still present at the end of the measurement window of 3 ns [127]. Thus, it is possible that increasing the proportion of triplet population as compared to the singlet population leads to differences in spectra and kinetics on the scale of tens of nanoseconds.

To conclude, we observe strong evidence of triplet formation in the pure polymer sample. This differs from the way triplet formation is usually considered in solar cell materials. Typically, it is described as a loss mechanism that competes with charge separation, as triplets are formed from CTE states at the heterojunction. This has been reported for this PBDB-T:ITIC as well [128]. However, if these triplets are generated in the pure polymer phase, there must be a pathway for triplet generation from singlets in the polymer. To avoid this loss and achieve higher PCE it is therefore important to find ways to reduce this direct triplet generation from singlets, instead of focussing on the triplet generation from CTE states.

### 6.4.2 Recombination Pathways

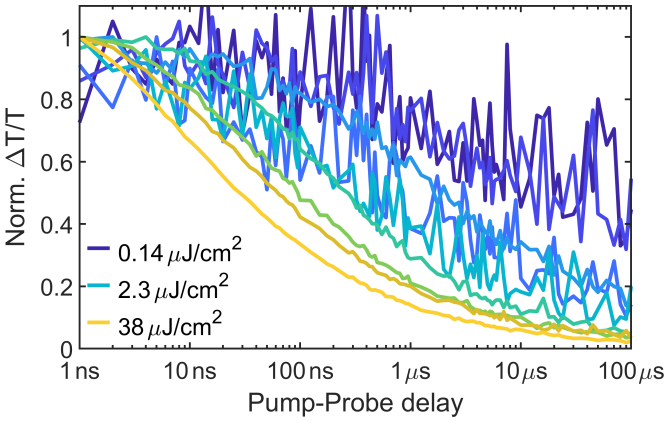


Figure 6.14: Fluence dependence of PBDB-T:ITIC kinetics from 1 ns to 100 $\mu$s (absolute signal intensity integrated from 590 - 760 nm).

To identify the dominant recombination mechanism, we measured the PP signal in a wavelength region that spans the GSB of both donor and acceptor (600 - 760 nm) at different excitation densities. When comparing the kinetics of the absolute signal intensity (Figure 6.14) we observe a clear trend: the higher the fluence of the pump pulse the faster the signal decays. This is to be expected in a solar cell with efficient charge separation. At long times after the pump ($>1$ ns) most of the excited states are separated charges which combine bimolecularly (see Section 2.2.4). The decay rate is therefore proportional to the square of the excited states density. We note that this observation of predominantly bimolecular recombination differs from the observations of others for the PffBT4T-2OD:O-IDFBR blend and other low-offset non-fullerene OPV systems [52, 61]. These previous studies found no fluence dependence of the decay rate and concluded that geminate-recombination of charges that fail to fully separate are a major loss mechanism in these OSCs. This does not seem to be the case for our sample.

We continue our analysis by investigating differences in the decay between the hole and the electron populations. As described in the previous chapter, we can distinguish between excited states on the donor polymers, which result in a ground state bleach at wavelengths shorter than 650 nm, and populations

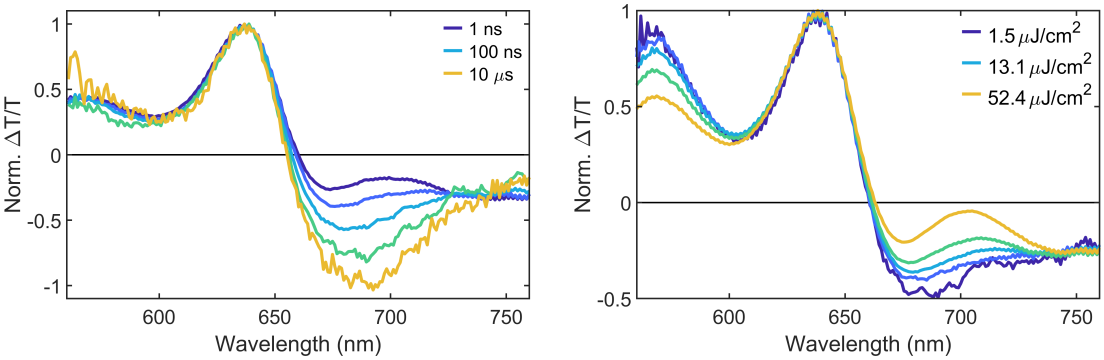


(a) Time dependence ($9.3\,\mu J\,cm^{-2}$) (b) Fluence dependence (1 ns)

Figure 6.15: PP spectra of PBDB-T:ITIC on a 1 ns to 10 $\mu$s timescale.

on the acceptor molecules, which result in a GSB around 700 nm. We observe different lifetimes for these features, with the positive spectral feature around 700 nm decaying faster than the peak at 640 nm (Figure 6.15a). The PP spectrum measured at 1 ns after the pump shows a clear acceptor GSB, while the spectrum at 10 $\mu$s only shows features from the donor. Thus, there must be an additional decay channel for electrons.

To gain further insights into this process we compare the spectra at 1 ns at different excitation densities (Figure 6.15b). At higher excitation densities the electron GSB is still very pronounced, whereas at low fluences it has already disappeared. This slower decay at higher excitation densities is characteristic of a trap assisted process: At higher fluences the traps become saturated, which increases the lifetime of the electrons. These traps could be lower energy sites within the film, such as aggregates, or triplet states at donor-acceptor interfaces. At all fluences the spectral dynamics are similar to the ones described above (Figure 6.16), with the acceptor GSB decaying faster than the donor GSB.

It is important to note that the trap assisted process identified above can not lead to electrons recombining faster than holes, as this would lead to a built-up of charges. One possible explanation for the disappearing acceptor GSB is that the electron transfers back into the PBDB-T phase, repopulating the donor exciton population. However, the LUMO level of the donor is 0.86 eV higher than that of the acceptor (see Figure 6.3). It is therefore unlikely that a significant proportion of electrons can overcome this barrier. Thus, we propose that the

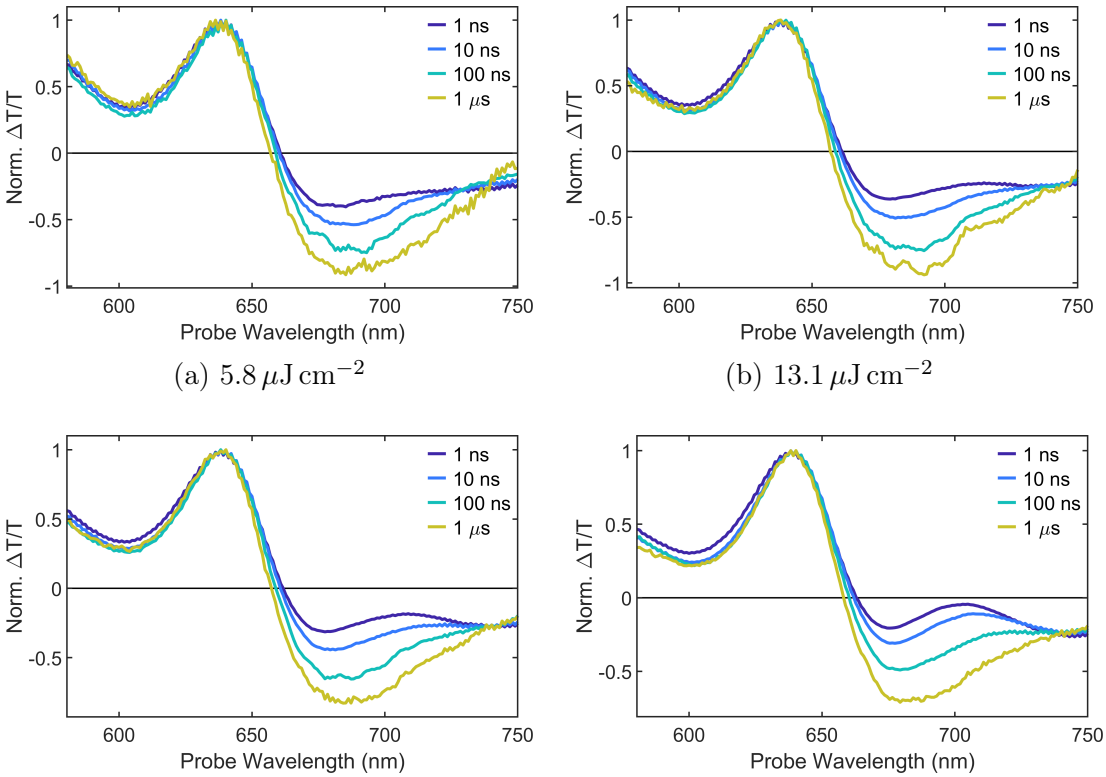


(a) $5.8\,\mu\mathrm{J\,cm^{-2}}$ (b) $13.1\,\mu\mathrm{J\,cm^{-2}}$

(c) $26.2\,\mu\mathrm{J\,cm^{-2}}$ (d) $52.4\,\mu\mathrm{J\,cm^{-2}}$

Figure 6.16: PBDB-T:ITIC spectra on a 1 ns to 1 $\mu$s timescale at excitation densities ranging from $5.8\,\mu\mathrm{J\,cm^{-2}}$ (a), to $52.4\,\mu\mathrm{J\,cm^{-2}}$ (d).

electrons populate dark trap states, states that can not be excited directly. Since these states are not visible in the absorption spectrum of the molecules, and therefore not contribute to the GSB, electrons populating these states would lead to a reduction in the acceptor GSB.

In addition to the disappearance of the acceptor GSB at lower fluences there is a another effect: The lower the fluence the weaker is the second peak of the donor GSB at 579 nm. This could be an indicator of triplet formation, similar to the dynamics shown in Figure 6.12. However, there is no clear weakening of the signal at longer wavelengths, e.g. $>750$ nm. A possible explanation for this is that the disappearing acceptor GSB, which leads to a more negative signal, compensates the weakening of the PIA, which leads to a less negative signal.

## 6.5 Insights from PPP

In an attempt to study the CTE population dynamics in this system, similar to the analysis in the previous chapter, we turned to PPP measurements. The push wavelength was set to 950 nm, where the PP spectra of all states discussed before show a PIA (singlets in PBDB-T and ITIC, as well as hole polarons in PBDB-T, see Figure 6.6b). We chose this wavelength to ensure that we push charges, while avoiding any absorption of the push by the ground state of the ITIC. The pump wavelength was 740 nm, predominantly exciting the acceptor molecules.

We start by presenting measurements of pristine samples with the push arriving directly after the pump, followed by the measurements on PBDB-T:PCBM, and finally the PBDB-T:ITIC blend.

### 6.5.1 Pristine ITIC

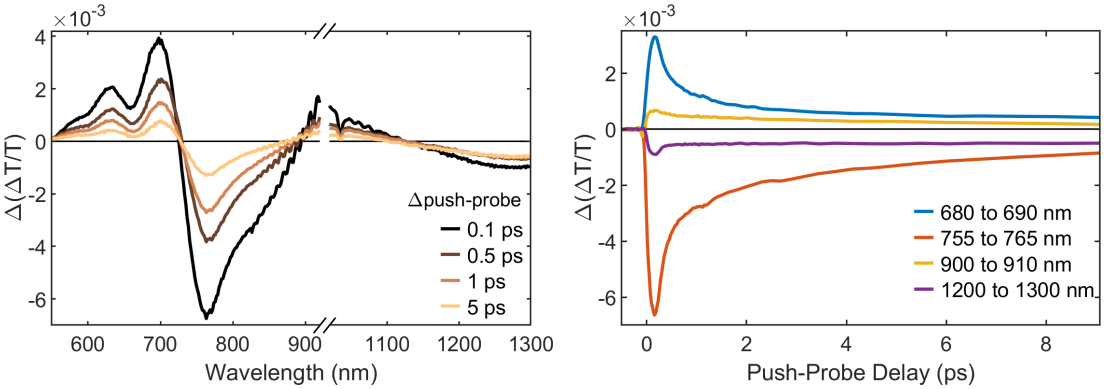


(a) Spectra (b) Kinetics

Figure 6.17: PPP spectra (a) and kinetics (b) of pristine ITIC with a push delay of 0.2 ps.

We began our PPP investigation by measuring a pristine ITIC film (Figure 6.17). Similar to the spectra described in Chapter 5, we observe a long-lived component which is still present at the end of our measurement window 9 ps after the push. However, the spectrum after the initial dynamics still contains a strong contribution from the positive ground state bleach. Overall, the spectrum changes much less than the spectra in the previous chapter (Figure 5.3a and 5.3b). In

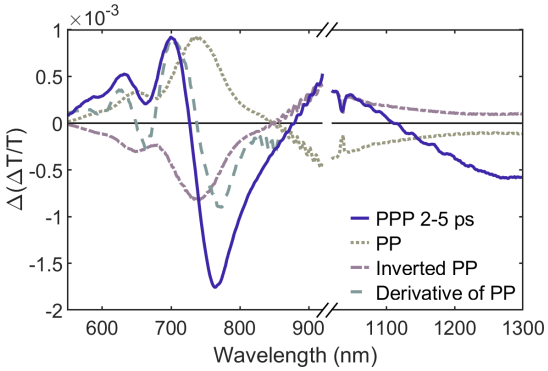


Figure 6.18: Comparison of PPP spectra of pristine ITIC with the PP spectrum and its derivative.

that chapter we attributed the initial spectrum, with its positive GSB, to charges generated by the push. We attributed the long-lasting component, that matched the inverted singlet PP spectrum, to a reduction in the singlet population.

For a similar analysis we compare the PPP spectrum integrated over push delays of 2 to 5 ps with the PP spectrum and the inverted PP spectrum of the same sample (Figure 6.18). Also shown is the derivative of the PP spectrum, which is similar to the EA signal in this material. The positive signal in the PPP spectrum around 900 nm matches the inverted PP spectrum. This indicates that the push again reduces the singlet population. The PPP signal at wavelengths below 850 nm can be explained as the derivative signal overlapped with an additional signal that is positive in the range below 700 nm, and negative signal above 700 nm. The presence of a derivative signal suggests the presence of separated charges. The shape of the overlapping signal is consistent with this: The charge signal of PBDB-T, as identified in Figure 6.6b, also has a negative feature on the low-energy side of the GSB.

The combination of a longer-lived charge signal and a derivative signal, in addition to the inverted singlet signal, suggests the following interpretation: When the push is absorbed by singlets it generates charges. These charges are sufficiently separated to not recombine quickly, and to cause an EA signal. It is not clear why the charges in this material are separated, while they remain in close proximity and recombine within about 1 ps in P3TEA. Investigations into differences in energy levels or morphology could provide additional insights.

### 6.5.2 Pristine PBDB-T

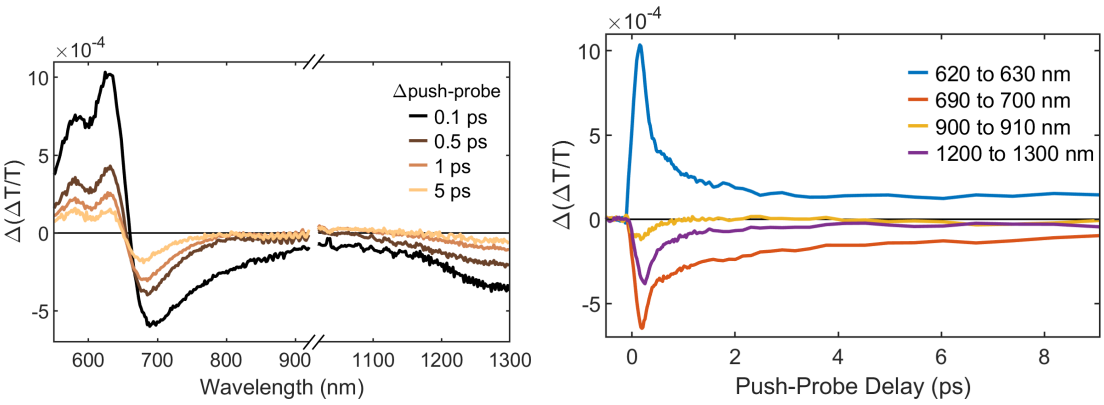


(a) Spectra (b) Kinetics

Figure 6.19: PPP spectra (a) and kinetics (b) of pristine PBDB-T with a push delay of 0.2 ps.

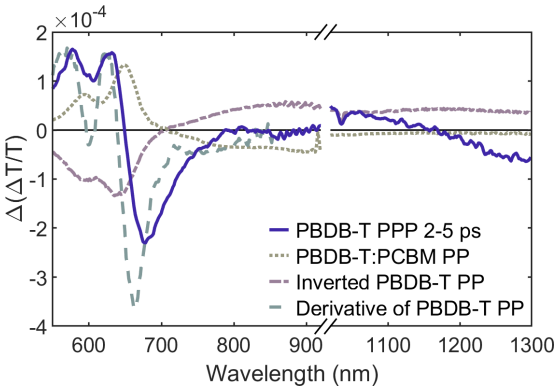


Figure 6.20: Comparison of PPP spectra of pristine PBDB-T with the inverted PP spectrum and its derivative, and the PP spectrum of the PBDB-T:PCBM blend.

As the next step, we measured the PPP response of a pristine PBDB-T film (Figure 6.20). Similar to the ITIC film, the spectral shape remains largely constant and the kinetics show a long-lived component. We again compare the PPP spectrum to the inverted PP singlet spectrum and its derivative (Figure 6.20). Additionally, we compare it to the PP spectrum of PBDB-T:PCBM which is dominated by charges. The spectrum can once more be explained as a combination

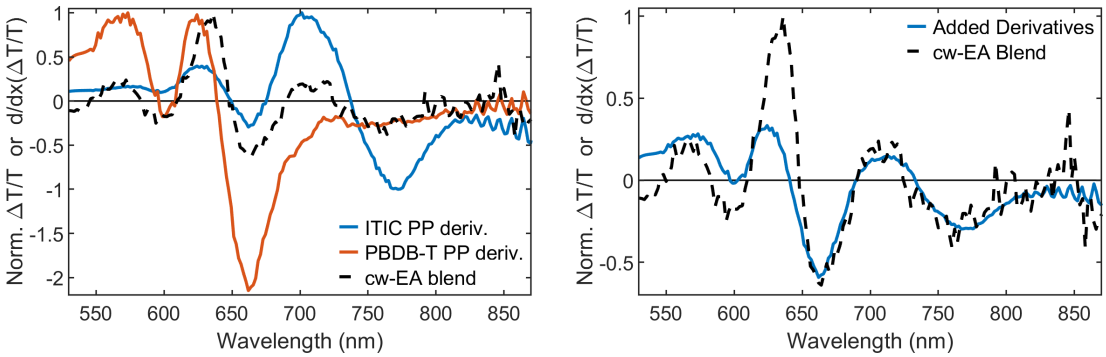


(a) Individual derivatives

(b) Added derivatives

Figure 6.21: Comparison of the device EA signal of PBDB-T:ITIC with the derivatives of the PP signal of pristine ITIC and PBDB-T films.

of these spectra. In this sample we also observe a blue shift of the zero-crossing point around 660 nm. This indicates that the relative contribution of the EA component increases with increasing push-probe delay. A possible explanation for this is that the average separation of charges increases over time, as charges are more likely to recombine when they are closer.

### 6.5.3 Components of the EA Signal

Before continuing the discussion of the PPP signals, we would like to comment on the different components of the EA signal. Figure 6.21a compares the EA signal measured on a device under continuous illumination with the derivatives of the PP signal of the pristine PBDB-T and ITIC films. Figure 6.21b compares the device EA with a linear combination of these derivative signals. The added derivatives match well with the device EA signal, consistent with our explanation in Section 3.1.3. By comparing the PPP signal with the derivatives of the individual components, we can therefore track the movement of charges away from the interface individually for the donor and the acceptor phase of the blend.

### 6.5.4 PBDB-T:PCBM Blend

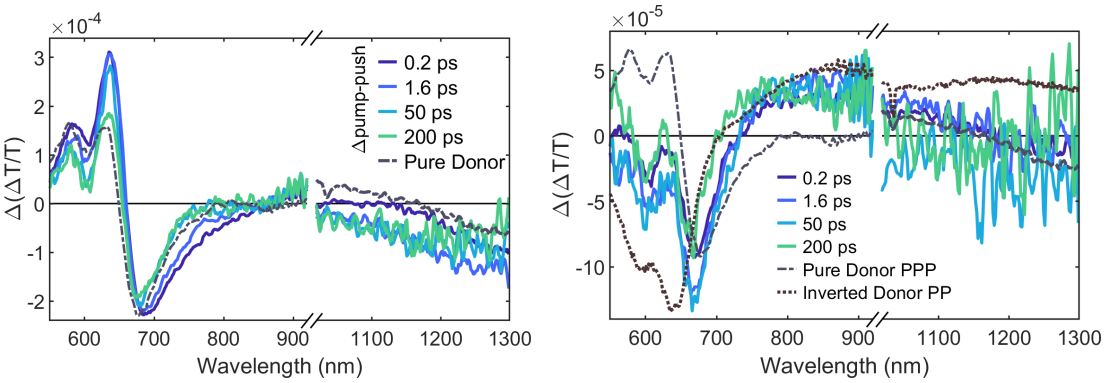


(a) Δpush-probe: 0.2 to 0.3 ps

(b) Δpush-probe: 2 to 3 ps

Figure 6.22: PPP spectra of a PBDB-T:PCBM blend at push delays from 0.2 to 200 ps, with push-probe delays integrated from 0.2 - 0.3 ps (a) and 2 - 3 ps (b) . Also shown are the PPP spectra of the pure donor (black dashed line), and the inverted PP spectrum from the pure PBDB-T film (black dotted line).

Similar to our discussion of our PP data in the previous sections, analysing the PPP spectra of the PBDB-T:PCBM blend allows us to study the spectral features of charges in the donor separated from any features of the acceptor (Figure 6.22). The spectra shortly after the push (Δpush-probe: 0.2 - 0.3 ps, Figure 6.22a) are very similar to the spectra of the pristine PBDB-T film (black line in Figure 6.22a). As discussed in Section 6.5.2, this signal is caused by short-lived charges that are generated when the push is absorbed by singlets on the PBDB-T. However, at longer push-probe delays (2 - 3 ps, Figure 6.22b) the spectra are different from the pure film. Below 720 nm the signal is negative, and from 720 - 1100 nm the signal is positive. The change in spectrum matches with the inverted PP spectrum of the pristine PBDB-T film (dotted line). This suggests that the charges generated by the push recombine faster than in the pure material, similar to the PPP dynamics in P3TEA:SFPDI$_2$ (Chapter 5). Interestingly, the PPP spectra do not change significantly over a large range of push delays. Observing this signal that is related to the singlet population at pump-push delays of 200 ps is surprising, since we do not expect a significant singlet population at this long time after the initial excitation. A possible explanation

for this long-lived singlet signal is that the push is absorbed by trapped singlets that do not separate into charges and are still present 200 ps after the pump. We note that we again normalise all PPP spectra in this chapter to the intensity of the PP PIA near the push wavelength, compensating for changes in the overall population density.

### 6.5.5 PBDB-T:ITIC Blend

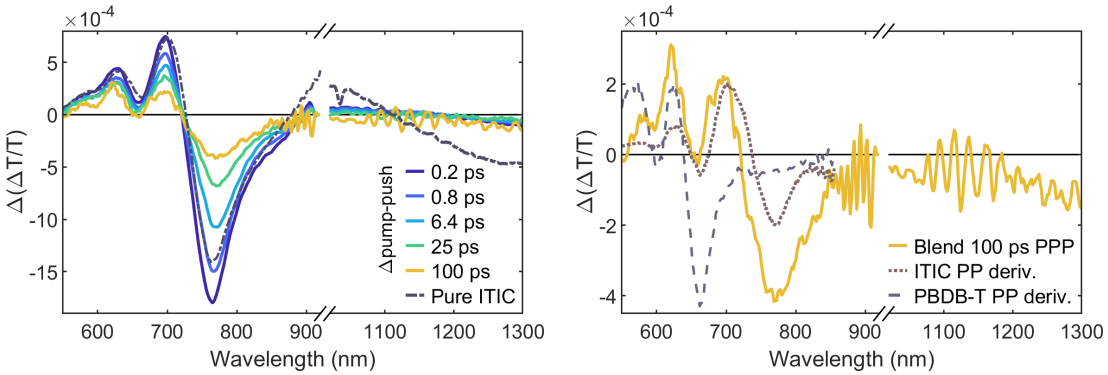


(a) All push delays (b) 100 ps delay only

Figure 6.23: PPP spectra of a PBDB-T:ITIC blend directly after the push (Δpush-probe integrated from 0.2 - 0.3 ps) at pump-push delays from 0.2 - 100 ps (a). Comparison of the spectrum at a push delay of 100 ps with the PP spectrum of pristine ITIC and its derivative (b).

Having discussed the PPP measurements on pristine donor and acceptor samples, we now turn towards the non-fullerene blend PBDB-T:ITIC. The pump was set to 740 nm, predominantly exciting the ITIC molecules. We begin by discussing the PPP spectra at short push-probe delays (Figure 6.23a). In contrast to the PBDB-T:PCBM blend, the initial PPP signal in the PBDB-T:ITIC blend changes significantly with increasing pump-push delay. At short push delays (Δpump-push = 0.2 ps), when the excited state population in the sample mainly consists of singlet excitons on the ITIC, the spectrum is similar to the pristine ITIC film (black line in Figure 6.23a). The main difference is a weaker positive signal from 900 - 1100 nm. In Section 6.5.1 we discussed that this signal indicates a reduced ITIC singlet population. This weaker contribution of this singlet

component therefore suggests that when the push interacts with the singlets, it either creates more charges than in the pristine ITIC sample, or the charges have a longer lifetime. A longer lifetime could be explained by the presence of a heterojunction in the blend. It is also possible that some of the charges are generated from singlets on the PBDB-T. However, the singlet PIA at the push wavelength is much stronger in the ITIC than in the PBDB-T, so that the push is more strongly absorbed by singlets in the ITIC. Additionaly, the pump was tuned to predominantly excite the ITIC molecules. Thus, we expect any contribution arising from interaction of the push with singlets on the PBDB-T to be small.

At longer pump-push delays the spectrum differs to a greater extend from the pristine samples. With increasing push delay the negative signal around 780 nm and the positive signal around 700 nm become weaker. The positive signal from 900 - 1100 nm is also becoming weaker, disappearing completely at a push delay of 100 ps. Comparing the signal at a delay of 100 ps with the derivatives of the PP spectra in the pristine samples (Figure 6.23b), the PPP signal appears to be a combination of both derivatives and no additional components. Thus, at long push delays we observe an EA contribution from both types of molecules, but no indication of a reduced singlet population. This suggests that the push is absorbed by bound charges at the interface, which then increase their separation, giving rise to an EA response as described before. Since we are observing the EA signal from both donor and acceptor, which indicates an increase in electric field in both phases of the heterojunction, it is likely that both holes and electrons move away from the interface after interacting with the push.

As a last step in our analysis, we now discuss the PPP spectra at longer push-probe delays (Figure 6.24). Here the blend spectrum deviates more from the spectrum of the pristine ITIC sample, with a negative signal below 700 nm and a positive signal above 1150 nm. This deviation can be explained by a stronger contribution of the inverted singlet PP signal. Surprisingly, the contribution of this singlet signal increases with increasing pump-push delay. This is especially apparent at push-probe delays integrated from 7 - 8 ps (Figure 6.24b). At these times after the pump there should not be many singlets present in the sample. The reasons for this behaviour are unclear: It is possible that the few remaining singlets are trapped in locations where they can not form charges, so that the only

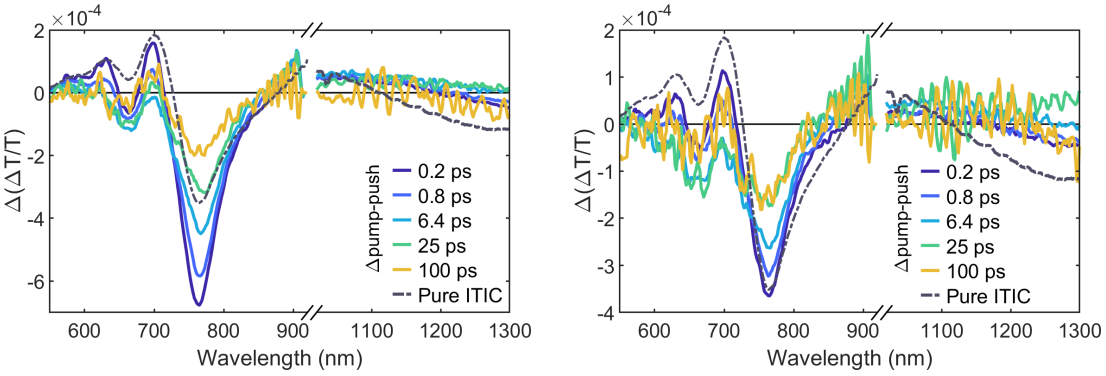


(a) Δpush-probe: 2 to 3 ps (b) Δpush-probe: 7 to 8 ps

Figure 6.24: PPP spectra and kinetics of a PBDB-T:ITIC blend at longer push-probe delays (integrated from 2 - 3 ps (a) and 7 - 8 ps (b)) and push delays from 0.2 to 100 ps.

effect of the push is to increase singlet-singlet annihilation. Another possibility is that the charges generated from these singlets are trapped, so that they recombine faster and have disappeared 7 ps after the push, leading to a stronger relative contribution of the singlet signal.

We can conclude that the effect of the push on the PBDB-T:ITIC blend is complicated and convoluted. The response of the pristine films already contains an EA signal, the charge signal does not disappear quickly so that we can not subtract the singlet component, and the EA and charge signals of donor and acceptor overlap. These factors prevent us from clearly identifying the response of charges bound at the interface, as we were able to do in the P3TEA:SF-$PDI_2$ blend. It is therefore very difficult to use PPP spectroscopy to study the charge dynamics in this materials system.

## 6.6 Conclusions and Outlook

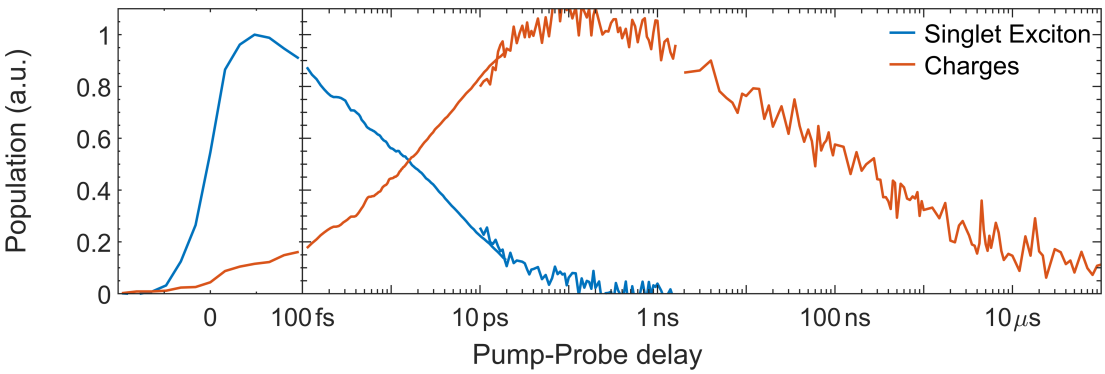


Figure 6.25: Overview of charge generation and recombination kinetics in PBDB-T:ITIC.

To summarise, we have studied the charge generation and recombination process in the efficient non-fullerene OPV system PBDB-T:ITIC. We have observed both electron transfer and hole transfer and extracted transfer times of the order of 10 ps for both processes. This charge generation time is several orders of magnitude slower than in efficient fullerene based photovoltaic materials [49], and approximately an order of magnitude slower than in most non-fullerene acceptor systems reported so far. Similarly slow hole-transfer [129] and electron-transfer [130] has been reported before for devices with lower photoconversion efficiencies. Studying the charge recombination process we were able to extract the lifetimes of charges. Figure 6.25 shows an overview of the charge generation and recombination kinetics in this system. We note that with our methods we are unable to distinguish whether the rate of charge generation is limited by diffusion of excitons to the heterojunction or by the dissociation of excitons at the interface.

Additionally, we found strong evidence for triplet generation in the pristine polymer sample. This shows that triplets can be directly formed from singlet excitons in the donor, not only from CTE states at the donor-acceptor heterojunction. We did not find evidence of significant triplet formation in the PBDB-T:ITIC blend, contrary to a previous report [128], suggesting that efficient charge formation can significantly reduce triplet formation in the polymer. Furthermore,

we found evidence for a trap assisted charge recombination pathway, in addition to the bimolecular recombination.

Using PPP we found that the push pulse generates charges in a similar way to the observations in P3TEA:SF-PDI$_2$ discussed in the previous chapter. However, in the PBDB-T:ITIC blend these initially generated charges separate and have much longer lifetimes. Furthermore, the characteristic features of the PP spectra overlap significantly. This makes it difficult to extract any useful information from these measurements. Potential future measurements could explore the PP and PPP spectral features further into the infrared wavelength region. Finding PIA signals that are specific for charge polarons only, without overlap with the singlet PIA, would allow to selectively excite charges. This would avoid many of of the complications discussed in this chapter.

# Chapter 7

# Summary and Outlook

## 7.1 Summary

In this work we studied the dynamics of charges in non-fullerene organic solar cells (OSCs). We employed a range of established spectroscopic methods, such as optical absorption, photoluminescence (PL), and pump-probe (PP) spectroscopy measurements. Additionally, we continued the development of pump-push-probe (PPP) spectroscopy, an advanced optical technique that allowed us to probe bound charges at the interfaces of donor-acceptor blends. This enabled us to determine the time-scales on which charge generation, separation, and recombination occur in the non-fullerene materials we studied. Importantly, we were able to show that fast charge separation is not necessary for high efficiencies. Based on the population dynamics we observed, we propose that the molecules continuously transition between singlet excitons, charges bound at the interface (charge transfer excitons, CTEs), and free charges, forming a thermodynamic equilibrium. We believe that this has important consequences for the development of future solar cell materials.

The model OSC material we investigated first is P3TEA:SF-PDI$_2$. This system has shown highly efficient generation of photocurrent despite a negligible offset between the molecular energy levels of donor and acceptor. This is contrary to previously expressed beliefs that an 'excess' energy is necessary to drive charge separation. In our PP measurements we found that charges are present at very short times after the pump, within hundreds of femtoseconds. In fact,

we were unable to see a rise time of the corresponding signal, which could be an indication of a hybridisation between the initially excited singlet state and the CTE state. Further evidence for this hybridisation was observed in time-resolved PL studies, where we measured emission from the the donor singlet exciton state following charge recombination. This suggests either back transfer from CTE states to the singlet, or a mixing of these two states. Additional PP measurements revealed evidence for a slower component of exciton dissociation, indicating additional formation of CTE states on a timescale of tens of picoseconds.

Despite this fast initial charge generation, we found that charge separation was slow, occurring on a timescale of $\sim 100\,\mathrm{ps}$. Since vibrational relaxation occurs on a faster timescale ($\sim 1\,\mathrm{ps}$), charges must separate from thermally relaxed CTE states. We concluded that charge separation is a thermally activated process that requires an activation energy to overcome the Coulomb binding energy of the CTE state. This was supported by temperature dependent PP experiments, showing that charges separate slower at lower temperatures.

To explore this further, we turned towards PPP spectroscopy, where a 'push' excites the sample a second time before it is probed. We began by carefully analysing the PPP spectra in a pure donor sample and found that the push creates a temporary charge population and reduces the overall excited state population. After taking into account the spectral features of these effects, we were able to identify a third component in the PPP spectra of the donor-acceptor blend: a derivative-like shape that matches the electroabsorption (EA) spectrum measured on a device. This feature is caused by charges separated by the push and is proportional to the population of CTE states.

The EA signal enabled us to directly monitor the dynamics of the CTE states. We found that the population of these bound charges is only slowly decreasing, even after the population of free charges is not increasing significantly any more. Since the internal quantum efficiency of these devices is $\sim 90\,\%$, these charges must eventually separate. This led us to propose that a thermodynamic equilibrium is formed between these states, where charges continuously recombine and re-separate. In addition, our PPP measurements at lower temperatures showed a reduced amount of CTE states per initially excited singlet state. This shift

of the equilibrium towards bound CTE states is further evidence for a thermal activation of charge separation.

The second low-offset non-fullerene OPV system we studied was PBDB-T:ITIC. Here, our PP spectra showed a clear rise in the charge signal, with a time-constant of $\sim 10$ ps for both electron and hole transfer. Thus, for highly efficient solar cells neither fast charge generation nor fast separation is necessary.

In this material we identified two pathways for non-radiative recombination, a major loss mechanism in OSCs. Firstly, we found strong evidence for triplet generation. Triplets are more likely to undergo non-radiative transitions to the ground state, followed by vibrational relaxation. Secondly, we discovered that trap assisted recombination occurs in this blend, which could also lead to non-radiative recombination.

Our attempts to study the CTE population via PPP spectroscopy were largely unsuccessful, due to the overlapping spectral features and complicated dynamics in this blend, demonstrating the limits of this technique.

The formation of a thermodynamic equilibrium between singlet excitons, CTE states, and free charges indicates new pathways for increasing solar cell performance. Instead of developing systems to drive charge separation via reversible processes, they should be designed to remove all irreversible processes. In particular, the CTE energy should be isoenergetic with the singlet energy of either the donor or the acceptor. This should enable us to reduce voltage losses without sacrificing charge separation efficiency. Device design efforts should then focus on removing non-radiative voltage losses, such as triplet formation and trap assisted recombination. For example, lowering the polymer triplet energy could reduce triplet formation due to the energy gap law, and improving film homogeneity by optimising the sample preparation procedures could remove traps.

## 7.2 Outlook

As mentioned above, we believe that our findings provide a new perspective on the mechanism behind charge separation, with implications for chemists, material scientists, and device physicists. In addition to optimising the absorption spectra

and transport properties of the molecules, design efforts should aim to remove any non-reversible steps from charge generation.

From a spectroscopy perspective there are open questions as well. To begin with, it is still unclear under which conditions efficient charge separation can occur without a driving force. As shown in a recent study, increasing the energy offset of the CTE state increases the quantum efficiency for many non-fullerene systems [52]. However, some donor polymers show a much stronger dependence on the excess energy than others. A systematic PP and PPP study comparing these systems could provide insights into these dynamics.

Additionally, for PPP spectroscopy, finding a way of very selectively exciting charges would greatly facilitate the interpretation of the spectra. This is especially important in blends with overlapping absorption and emission spectra, such as PBDB-T:ITIC. For example, PP measurements in the infrared wavelength region could reveal PIA signals that are specific to charges. Tuning the push to excite these could lead to clearer signals.

Another valuable experiment would be to repeat the temperature dependent PPP measurement with longer push-probe delays. This might enable us to fully extract the kinetic of the CTE population for different temperatures. Furthermore, exploring the influence of pump and push fluence on the CTE kinetic could show how the equilibrium between free charges, CTE states, and singlet excitons depends on the population density. However, PPP measurements are very time-intensive, so this large parameter space has to be explored systematically.

The measures suggested above could allow further increases in OSC efficiencies, exceeding a PCE of 20 %. If current trends continue, future high performance solar cells could be made of abundant, non-toxic organic materials, produced with energy-efficient methods. Optimising scalable industrial processes such as roll-to-roll printing for these new non-fullerene solar cells could enable them to outcompete silicon and perovskite based technologies, and contribute to global efforts against climate change.

# Appendix A

# Supporting Figures for P3TEA:SF-PDI$_2$

## A.1 Supporting Measurements

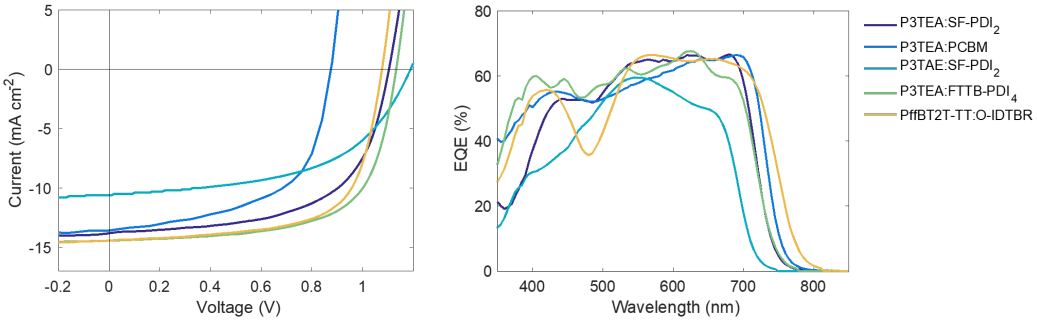


(a) Current - Voltage (b) External Quantum Efficiency

Figure A.1: J-V and EQE curves of P3TEA:SF-PDI$_2$ and other non-fullerene blends. *Measurements and plots by Dr Philip Chow and co-workers, used with permission.*

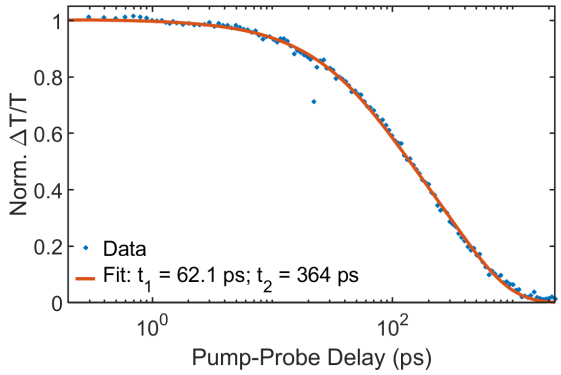


Figure A.2: Fit of PP kinetics of pristine P3TEA film with a sum of exponential decays (see Section 6.3.1 for details).

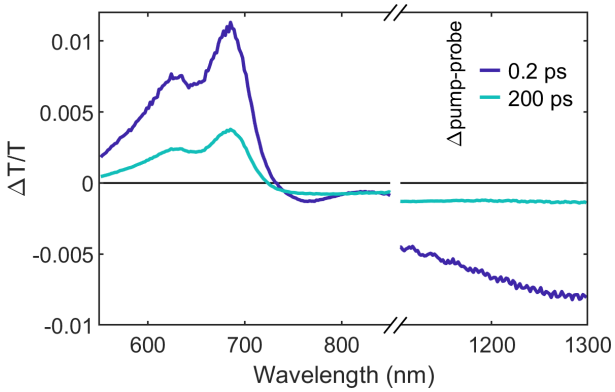


(a) Pristine P3TEA

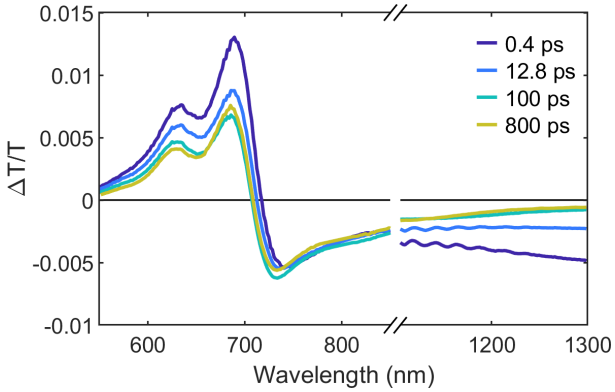


(b) P3TEA:SF-PDI$_2$

Figure A.3: Charge generation and separation: Non-normalised PP spectra of pristine P3TEA (a) and the P3TEA:SF-PDI$_2$ blend (b) at the higher pump fluences used in PPP measurements ($\approx 1\,\mu J/cm^{-2}$)).

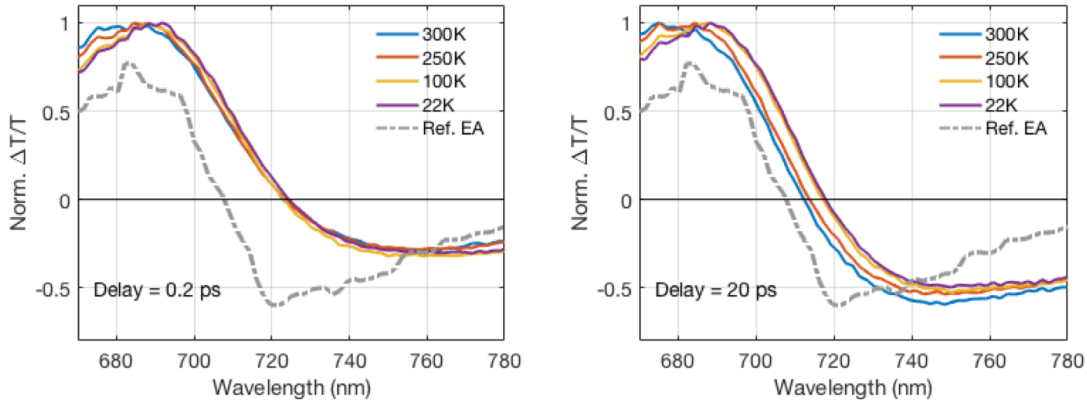


Figure A.4: Temperature dependence of P3TEA:PCBM PP spectra. *Measurements and plots by Dr Philip Chow and co-workers, used with permission.*

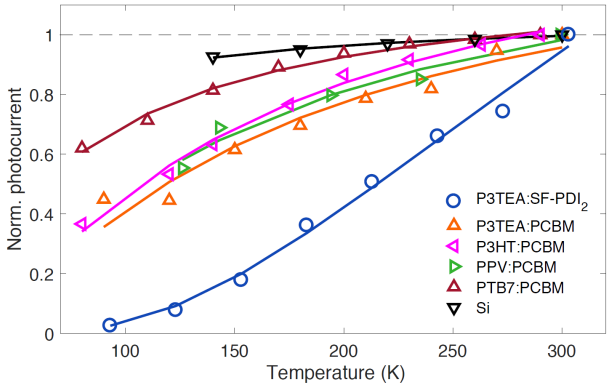


Figure A.5: Temperature dependence of device photocurrent. Data was measured at short-circuit condition. The photocurrent of non-fullerene P3TEA:SF-PDI2 device drops more significantly than P3TEA:PCBM. This is consistent with the temperature dependence found for the spectroscopy data. Data for annealed P3HT:PCBM, MEH-PPV:PCBM, PTB7:PCBM, and Si (reproduced from Reference [110, 112, 113, 131]) are shown for comparison. The devices were under sufficiently low intensity to avoid current drop due to bimolecular recombination, as described in detail by Gao et al. [110], with the exception of PTB7:PCBM (measured under simulated solar illumination). *Measurements, plot, and description by Dr Philip Chow and co-workers, used with permission.*

## A.2 Additional Samples

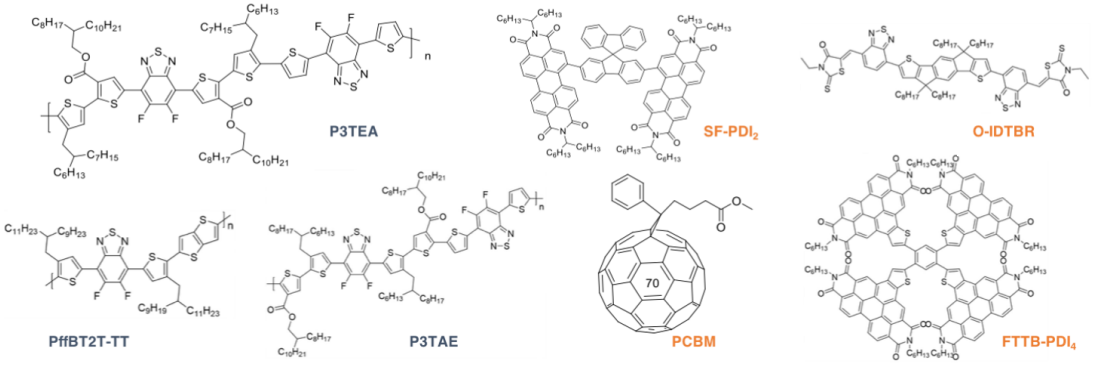


Figure A.6: Chemical structures of electron donor (blue labels) and acceptor molecules (orange labels) used to study the dynamics of CTE states. *Figure by Dr Philip Chow, used with permission.*

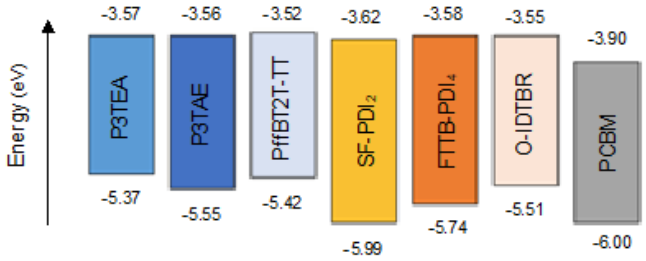


Figure A.7: Energy levels of materials used in study on CTE dynamics as estimated from cyclic voltammetry. *Measurements and plot by Dr Philip Chow and co-workers, used with permission.*

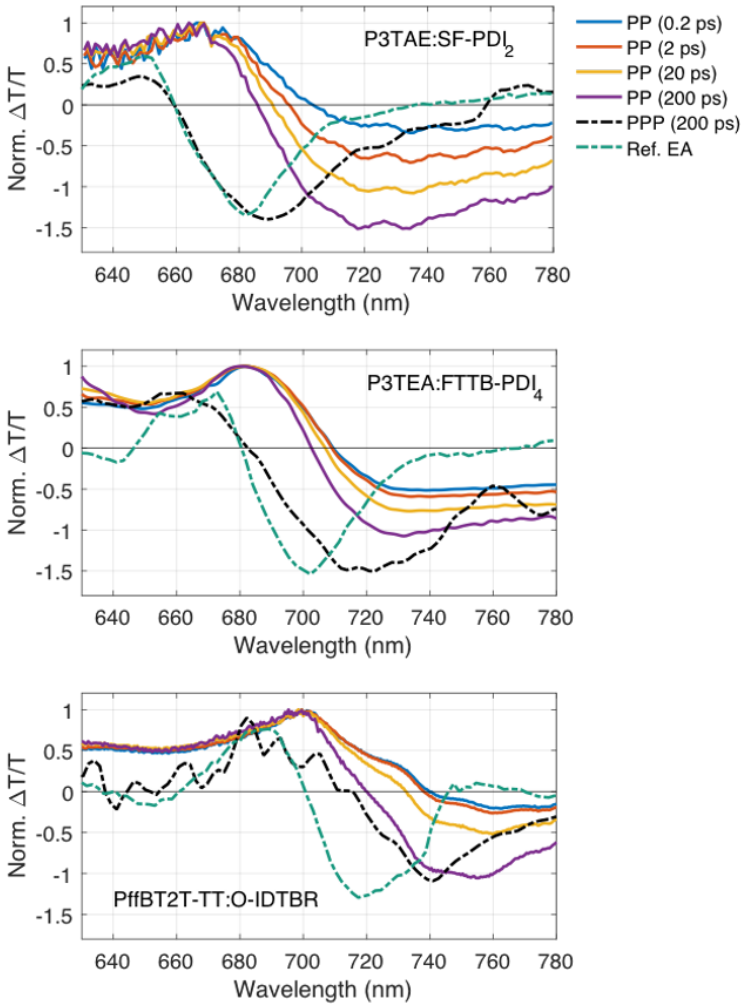


Figure A.8: Comparison of PP and PPP spectra of P3TEA:FTTB-PDI4, P3TAE:SF-PDI$_2$ and PffBT2T-TT:O-IDTBR. *PPP data in bottom panel and all PP and EA data measured by Dr Philip Chow and co-workers. Plot by Dr Philip Chow and co-workers, used with permission.*

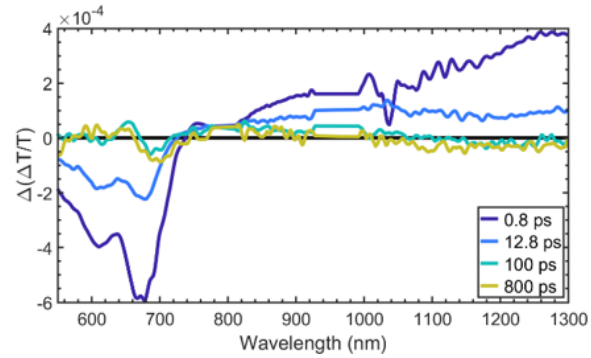


(a) P3TAE:SF-PDI$_2$

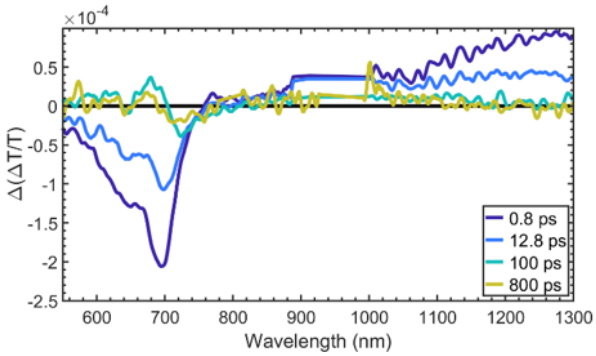


(b) P3TEA:FTTB-PDI$_4$

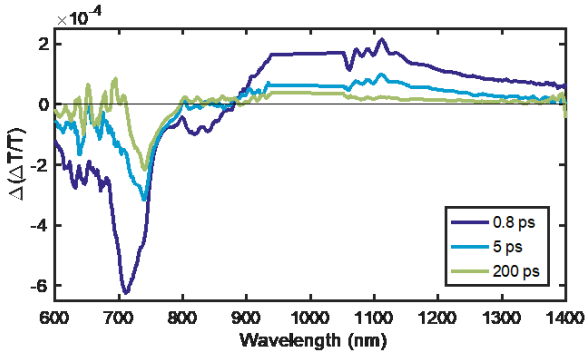


(c) PffBT2T-TT:O-IDTBR

Figure A.9: PPP data of additional samples. *Data in panel (c) measured and plotted by Dr Philip Chow and co-workers.*

# Appendix B

# Supporting Figures for PBDB-T:ITIC

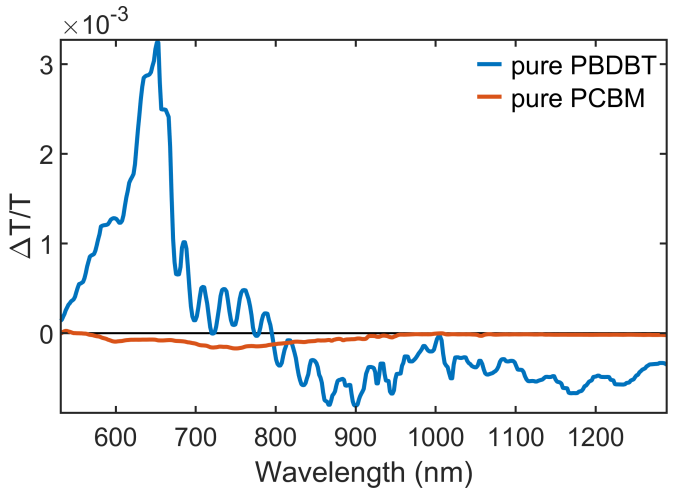


Figure B.1: Comparison of PP signal of pristine PBDB-T and PCBM. The PBDBT film was excited at 520 nm with a 50 $\mu$W beam, the PCBM film at 488 nm with a 70 $\mu$W beam. Despite the higher excitation intensity, the signal of the PCBM film is much weaker.

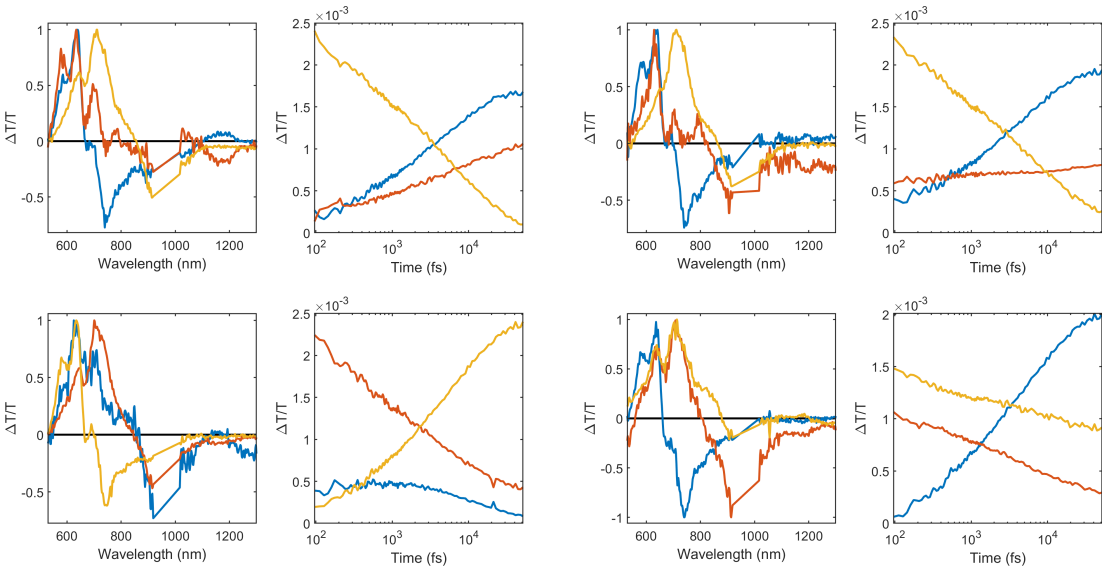


(a) 3 Species

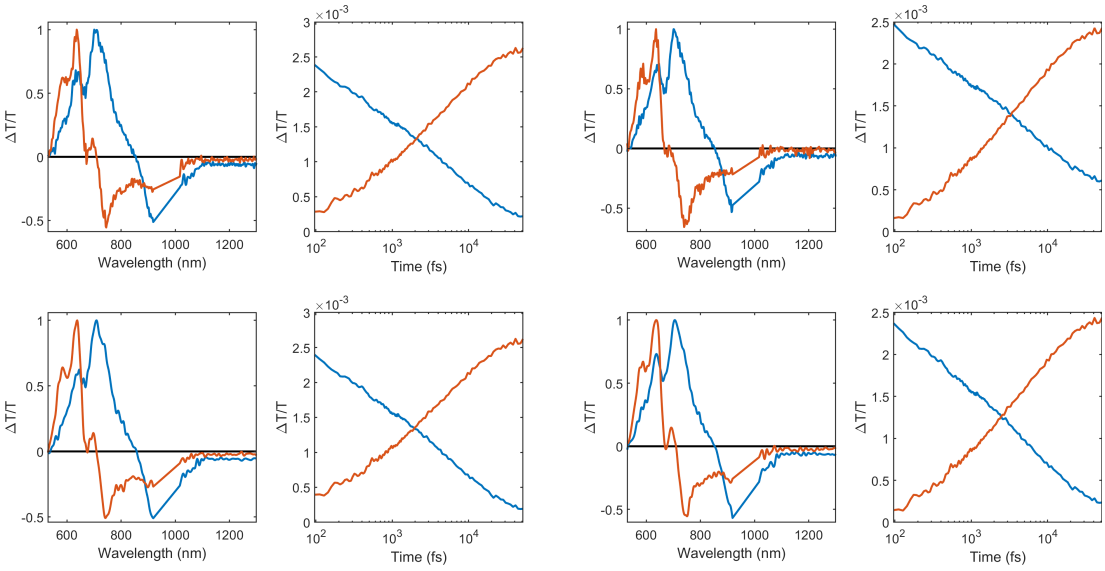


(b) 2 Species

Figure B.2: Examples of different outputs of the genetic algorithm: Species and corresponding kinetics for data showing hole-transfer in PBDB-T:ITIC.

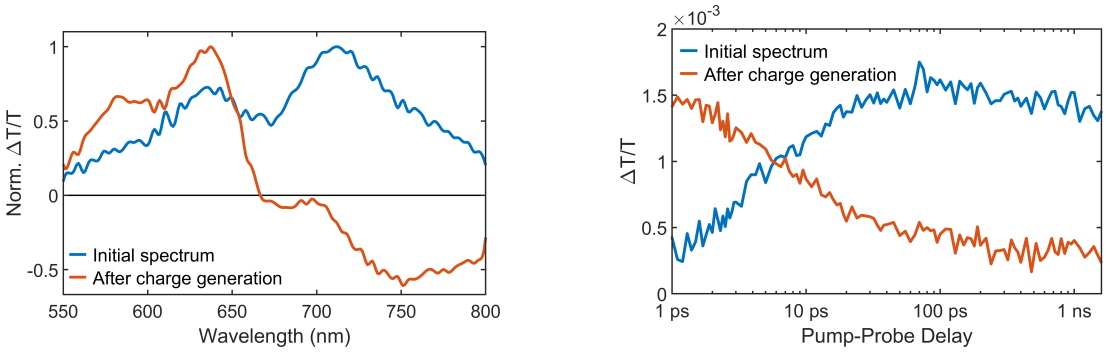


(a) Spectra (b) Kinetics

Figure B.3: Hole transfer dynamics on a picosecond to nanosecond timescale as extracted via the genetic algorithm.

# References


[1] UK Office for National Statistics. "Renewable electricity capacity and generation (et 6.1)", 2019. https://www.gov.uk/government/statistics/energy-trends-section-6-renewables (Accessed on 2019-08-17). 1

[2] Fraunhofer-Institut für Solare Energiesysteme. "Photovoltaics report", 2019. https://www.ise.fraunhofer.de/en/publications/studies/photovoltaics-report.html (Accessed on 2019-08-17). 1

[3] US National Renewable Energy Laboratory (NREL). "Best research-cell efficiency chart", 2019. https://www.nrel.gov/pv/cell-efficiency.html (Accessed on 2019-08-17). 1, 2

[4] Felix Haase, Christina Hollemann, Sören Schäfer, Agnes Merkle, Michael Rienäcker, Jan Krügener, Rolf Brendel, and Robby Peibst. "Laser contact openings for local poly-Si-metal contacts enabling 26.1%-efficient POLO-IBC solar cells" *Solar Energy Materials and Solar Cells*, 186(May):184–193, 2018. 1

[5] Roar R. Søndergaard, Markus Hösel, and Frederik C. Krebs. "Roll-to-Roll fabrication of large area functional organic materials" *Journal of Polymer Science, Part B: Polymer Physics*, 51(1):16–34, 2013. 1

[6] Seok-In Na, You-Hyun Seo, Yoon-Chae Nah, Seok-Soon Kim, Hyojung Heo, Jueng-Eun Kim, Nicholas Rolston, Reinhold H. Dauskardt, Mei Gao, Youngu Lee, and Doojin Vak. "High Performance Roll-to-Roll Produced Fullerene-Free Organic Photovoltaic Devices via Temperature-Controlled Slot Die Coating" *Advanced Functional Materials*, 29(6):1805825, 2019. 1

[7] Yong Cui, Huifeng Yao, Jianqi Zhang, Tao Zhang, Yuming Wang, Ling Hong, Kaihu Xian, Bowei Xu, Shaoqing Zhang, Jing Peng, Zhixiang Wei, Feng Gao, and Jianhui Hou. "Over 16% efficiency organic photovoltaic cells enabled by a chlorinated acceptor with increased open-circuit voltages" *Nature Communications*, 10(1):1–8, 2019. 2

[8] Wenchao Zhao, Deping Qian, Shaoqing Zhang, Sunsun Li, Olle Inganäs, Feng Gao, and Jianhui Hou. "Fullerene-Free Polymer Solar Cells with over 11% Efficiency and Excellent Thermal Stability" *Advanced Materials*, 28(23):4734–4739, 2016. 2, 91, 92, 93, 95

[9] Anna Köhler and Heinz Bässler. "Electronic Processes in Organic Semiconductors" *Wiley*, 2015. 5, 10, 13, 16

[10] Vladsinger. "Wikimedia commons: Orbital hybridization in benzene rings.", 2009. https://commons.wikimedia.org/wiki/File:Benzene_Orbitals.svg (Accessed on 2019-08-11). 6

[11] Anna Köhler and David Beljonne. "The singlet-triplet exchange energy in conjugated polymers" *Advanced Functional Materials*, 14(1):11–18, 2004. 8

[12] Anna Köhler and Heinz Bässler. "Triplet states in organic semiconductors" *Materials Science and Engineering: R*, 66(4-6):71–109, 2009. 8

[13] Mark M. Somoza. "Wikimedia commons: Depiction of franck condon principle in absorption and fluorescence.", 2006. https://commons.wikimedia.org/wiki/File:Franck-Condon-diagram.png (Accessed on 2019-08-08). 12

[14] Mark M. Somoza. "Wikimedia commons: Depiction of absorption and fluorescence progression due to changes in vibrational levels during electronic transition.", 2006. https://commons.wikimedia.org/wiki/File:Vibration-fluor-abs.png (Accessed on 2019-08-08). 12

[15] Robert T. Ross. "Some Thermodynamics of Photochemical Systems" *The Journal of Chemical Physics*, 46(12):4590–4593, 1967. 14, 20

[16] Robert Englman and Joshua Jortner. "The energy gap law for radiationless transitions in large molecules" *Molecular Physics*, 18(2):145–164, 1970. 14

[17] Abraham Nitzan, Shaul Mukamel, and Joshua Jortner. "Energy gap law for vibrational relaxation of a molecule in a dense medium" *The Journal of Chemical Physics*, 63(1):200–207, 1975. 14

[18] Willem Siebrand and Digby F. Williams. "Isotope Rule for Radiationless Transitions with an Application to Triplet Decay in Aromatic Hydrocarbons" *The Journal of Chemical Physics*, 46(1):403–404, 1967. 14

[19] Gregory D. Scholes. "Long-Range Resonance Energy Transfer in Molecular Systems" *Annual Review of Physical Chemistry*, 54(1):57–87, 2003. 15

[20] Jean-Luc Bredas, Joseph E. Norton, Jerome Cornil, and Veaceslav Coropceanu. "Molecular Understanding of Organic Solar Cells: The Challenges" *Acc. Chem. Res.*, 42(11):1691–1699, 2009. 17, 21, 60

[21] Tracey M. Clarke and James R. Durrant. "Charge Photogeneration in Organic Solar Cells" *Chemical Reviews*, 110(11):6736–6767, 2010. 17, 21

[22] Nicola Gasparini, Andrew Wadsworth, Maximilian Moser, Derya Baran, Iain McCulloch, and Christoph J. Brabec. "The Physics of Small Molecule Acceptors for Efficient and Stable Bulk Heterojunction Solar Cells" *Advanced Energy Materials*, 8(12):1703298, 2018. 18, 89

[23] Cenqi Yan, Stephen Barlow, Zhaohui Wang, He Yan, Alex K.-Y. Jen, Seth R. Marder, and Xiaowei Zhan. "Non-fullerene acceptors for organic solar cells" *Nature Reviews Materials*, 3:18003, 2018. 18

[24] Jianquan Zhang, Huei Shuan Tan, Xugang Guo, Antonio Facchetti, and He Yan. "Material insights and challenges for non-fullerene organic solar cells based on small molecular acceptors" *Nature Energy*, 3(9):720–731, 2018. 18

[25] Pei Cheng, Gang Li, Xiaowei Zhan, and Yang Yang. "Next-generation organic photovoltaics based on non-fullerene acceptors" *Nature Photonics*, 12(3):131–142, 2018. 18

[26] Jianhui Hou, Olle Inganäs, Richard H. Friend, and Feng Gao. "Organic solar cells based on non-fullerene acceptors" *Nature Materials*, 17(2):119–128, 2018. 18

[27] Jun Yuan, Yunqiang Zhang, Liuyang Zhou, Guichuan Zhang, Hin-Lap Yip, Tsz-Ki Lau, Xinhui Lu, Can Zhu, Hongjian Peng, Paul A. Johnson, Mario Leclerc, Yong Cao, Jacek Ulanski, Yongfang Li, and Yingping Zou. "Single-Junction Organic Solar Cell with over 15% Efficiency Using Fused-Ring Acceptor with Electron-Deficient Core" *Joule*, 3(4):1140–1151, 2019. 18

[28] Lingxian Meng, Yamin Zhang, Xiangjian Wan, Chenxi Li, Xin Zhang, Yanbo Wang, Xin Ke, Zuo Xiao, Liming Ding, Ruoxi Xia, Hin-Lap Yip, Yong Cao, and Yongsheng Chen. "Organic and solution-processed tandem solar cells with 17.3% efficiency" *Science*, 361(6407):1094–1098, 2018. 18

[29] William Shockley and Hans J. Queisser. "Detailed Balance Limit of Efficiency of p-n Junction Solar Cells" *Journal of Applied Physics*, 32(3):510, 1961. 19

[30] Hans J. Queisser. "Detailed balance limit for solar cell efficiency" *Materials Science and Engineering: B*, 159-160:322–328, 2009. 19

[31] Uwe Rau, Ulrich W. Paetzold, and Thomas Kirchartz. "Thermodynamics of light management in photovoltaic devices" *Physical Review B*, 90(3):035211, 2014. 19

[32] Greg P. Smestad and Harald R. Ries. "Luminescence and current-voltage characteristics of solar cells and optoelectronic devices" *Solar Energy Materials and Solar Cells*, 25(1-2):51–71, 1992. 20

[33] Uwe Rau. "Reciprocity relation between photovoltaic quantum efficiency and electroluminescent emission of solar cells" *Physical Review B*, 76(8):085303, 2007. 20, 90

[34] William H. Miller. "Perspective: Quantum or classical coherence?" *The Journal of Chemical Physics*, 136(21):210901, 2012. 20

[35] Johannes Benduhn, Kristofer Tvingstedt, Fortunato Piersimoni, Sascha Ullbrich, Yeli Fan, Manuel Tropiano, Kathryn A. McGarry, Olaf Zeika, Moritz K. Riede, Christopher J. Douglas, Stephen Barlow, Seth R. Marder, Dieter Neher, Donato Spoltore, and Koen Vandewal. "Intrinsic non-radiative voltage losses in fullerene-based organic solar cells" *Nature Energy*, 2(6):17053, 2017. 20, 90

[36] Jizhong Yao, Thomas Kirchartz, Michelle S. Vezie, Mark A. Faist, Wei Gong, Zhicai He, Hongbin Wu, Joel Troughton, Trystan Watson, Daniel Bryant, and Jenny Nelson. "Quantifying losses in open-circuit voltage in solution-processable solar cells" *Physical Review Applied*, 4(1):014020, 2015. 20, 60

[37] Deping Qian, Zilong Zheng, Huifeng Yao, Wolfgang Tress, Thomas R. Hopper, Shula Chen, Sunsun Li, Jing Liu, Shangshang Chen, Jiangbin Zhang, Xiao Ke Liu, Bowei Gao, Liangqi Ouyang, Yingzhi Jin, Galia Pozina, Irina A. Buyanova, Weimin M. Chen, Olle Inganäs, Veaceslav Coropceanu, Jean-Luc Bredas, He Yan, Jianhui Hou, Fengling Zhang, Artem A. Bakulin, and Feng Gao. "Design rules for minimizing voltage losses in high-efficiency organic solar cells" *Nature Materials*, 17(8):703–709, 2018. 20, 24, 59, 65, 89

[38] S. Matthew Menke, Niva A. Ran, Guillermo C. Bazan, and Richard H. Friend. "Understanding Energy Loss in Organic Solar Cells: Toward a New Efficiency Regime" *Joule*, 2(1):25–35, 2018. 21, 60, 69, 80, 89

[39] Hyojung Cha, George Fish, Joel Luke, Ahmad Alraddadi, Hyun Hwi Lee, Weimin Zhang, Yifan Dong, Saurav Limbu, Andrew Wadsworth, Iuliana P. Maria, Laia Francàs, Hou Lon Sou, Tian Du, Ji-Seon Kim, Martyn A. McLachlan, Iain McCulloch, and James R. Durrant. "Suppression of Recombination Losses in Polymer:Nonfullerene Acceptor Organic Solar Cells due to Aggregation Dependence of Acceptor Electron Affinity" *Advanced Energy Materials*, 9(27):1901254, 2019. 21, 25

[40] Atsuhiko Miyata, Anatolie Mitioglu, Paulina Plochocka, Oliver Portugall, Jacob Tse-Wei Wang, Samuel D. Stranks, Henry J. Snaith, and Robin J. Nicholas. "Direct measurement of the exciton binding energy and effective masses for charge carriers in organic–inorganic tri-halide perovskites" *Nature Physics*, 11(7):582–587, 2015. 21

[41] Jung Hwa Seo, Youngeup Jin, Jacek Z. Brzezinski, Bright Walker, and Thuc-Quyen Nguyen. "Exciton Binding Energies in Conjugated Polyelectrolyte Films" *ChemPhysChem*, 10(7):1023–1027, 2009. 21

[42] Carsten Deibe, Thomas Strobe, and Vladimir Dyakonov. "Role of the charge transfer state in organic donor-acceptor solar cells" *Advanced Materials*, 22(37):4097–4111, 2010. 21

[43] Feng Gao and Olle Inganäs. "Charge generation in polymer–fullerene bulk-heterojunction solar cells" *Physical Chemistry Chemical Physics*, 16(38):20291–20304, 2014. 21

[44] Sheridan Few, Jarvist M. Frost, and Jenny Nelson. "Models of charge pair generation in organic solar cells" *Physical Chemistry Chemical Physics*, 17(4):2311–2325, 2015. 21

[45] Simon Gélinas, Olivier Paré-Labrosse, Colin Nadeau Brosseau, Sebastian Albert-Seifried, Christopher R. McNeill, Kiril R. Kirov, Ian A. Howard, Richard Leonelli, Richard H. Friend, and Carlos Silva. "The binding energy of charge-transfer excitons localized at polymeric semiconductor heterojunctions" *Journal of Physical Chemistry C*, 115(14):7114–7119, 2011. 21

[46] Timothy M. Burke, Sean Sweetnam, Koen Vandewal, and Michael D. McGehee. "Beyond Langevin Recombination: How Equilibrium Between Free Carriers and Charge Transfer States Determines the Open-Circuit Voltage of Organic Solar Cells" *Advanced Energy Materials*, 5(11):1500123, 2015. 21, 25, 60, 84, 89

[47] S. Matthew Menke, Alexandre Cheminal, Patrick Conaghan, Niva A. Ran, Neil C. Greehnam, Guillermo C. Bazan, Thuc-Quyen Nguyen, Akshay Rao, and Richard H. Friend. "Order enables efficient electron-hole separation at an organic heterojunction with a small energy loss" *Nature Communications*, 9(1):277, 2018. 21, 42, 57

[48] Askat E. Jailaubekov, Adam P. Willard, John R. Tritsch, Wai-Lun Chan, Na Sai, Raluca Gearba, Loren G. Kaake, Kenrick J. Williams, Kevin Leung, Peter J. Rossky, and X.-Y. Zhu. "Hot charge-transfer excitons set the time limit for charge separation at donor/acceptor interfaces in organic photovoltaics" *Nature Materials*, 12(1):66–73, 2013. 23

[49] Simon Gélinas, Akshay Rao, Abhishek Kumar, Samuel L. Smith, Alex W. Chin, Jenny Clark, Tom S. van der Poll, Guillermo C. Bazan, and Richard H. Friend. "Ultrafast Long-Range Charge Separation in Organic Semiconductor Photovoltaic Diodes" *Science*, 343(6170):512–516, 2014. 23, 42, 57, 60, 62, 118

[50] Safa Shoaee, Tracey M. Clarke, Chun Huang, Stephen Barlow, Seth R. Marder, Martin Heeney, Iain McCulloch, and James R. Durrant. "Acceptor Energy Level Control of Charge Photogeneration in Organic Donor/Acceptor Blends" *Journal of the American Chemical Society*, 132(37):12919–12926, 2010. 23

[51] Stoichko D. Dimitrov and James R. Durrant. "Materials Design Considerations for Charge Generation in Organic Solar Cells" *Chemistry of Materials*, 26(1):616–630, 2014. 23

[52] Hyojung Cha, Ching-Hong Tan, Jiaying Wu, Yifan Dong, Weimin Zhang, Hu Chen, Sridhar Rajaram, K. S. Narayan, Iain McCulloch, and James R. Durrant. "An Analysis of the Factors Determining the Efficiency of Photocurrent Generation in Polymer:Nonfullerene Acceptor Solar Cells" *Advanced Energy Materials*, 8(32):1801537, 2018. 23, 25, 107, 124

[53] Giulia Grancini, Margherita Maiuri, Daniele Fazzi, Annamaria Petrozza, Hans-Joachim Egelhaaf, Daniele Brida, Giulio Cerullo, and Guglielmo Lanzani. "Hot exciton dissociation in polymer solar cells" *Nature Materials*, 12(1):29–33, 2013. 23

[54] Koen Vandewal, Steve Albrecht, Eric T. Hoke, Kenneth R. Graham, Johannes Widmer, Jessica D. Douglas, Marcel Schubert, William R. Mateker, Jason T. Bloking, George F. Burkhard, Alan Sellinger, Jean M. J. Fréchet, Aram Amassian, Moritz K. Riede, Michael D. McGehee, Dieter Neher, and Alberto Salleo. "Efficient charge generation by relaxed charge-transfer states at organic interfaces" *Nature Materials*, 13(1):63–68, 2013. 23, 60

[55] Heinz Bässler and Anna Köhler. "'Hot or cold': how do charge transfer states at the donor–acceptor interface of an organic solar cell dissociate?" *Physical Chemistry Chemical Physics*, 17(43):28451–28462, 2015. 23

[56] Brett M. Savoie, Nicholas E. Jackson, Lin X. Chen, Tobin J. Marks, and Mark A. Ratner. "Mesoscopic Features of Charge Generation in Organic Semiconductors" *Accounts of Chemical Research*, 47(11):3385–3394, 2014. 23

[57] Guangjun Nan, Xu Zhang, and Gang Lu. "Do 'Hot' Charge-Transfer Excitons Promote Free Carrier Generation in Organic Photovoltaics?" *The Journal of Physical Chemistry C*, 119(27):15028–15035, 2015. 23

[58] Miquel Huix-Rotllant, Hiroyuki Tamura, and Irene Burghardt. "Concurrent Effects of Delocalization and Internal Conversion Tune Charge Separation at Regioregular Polythiophene–Fullerene Heterojunctions" *The Journal of Physical Chemistry Letters*, 6(9):1702–1708, 2015. 23

[59] Nicholas R. Monahan, Kristopher W. Williams, Bharat Kumar, Colin Nuckolls, and X.-Y. Zhu. "Direct Observation of Entropy-Driven Electron-Hole Pair Separation at an Organic Semiconductor Interface" *Physical Review Letters*, 114(24):247003, 2015. 23

[60] Andreas P. Arndt, Marina Gerhard, Aina Quintilla, Ian A. Howard, Martin Koch, and Uli Lemmer. "Time-Resolved Charge-Transfer State Emission in Organic Solar Cells: Temperature and Blend Composition Dependences of Interfacial Traps" *The Journal of Physical Chemistry C*, 119(24):13516, 2015. 23

[61] Yifan Dong, Hyojung Cha, Jiangbin Zhang, Ernest Pastor, Pabitra Shakya Tuladhar, Iain McCulloch, James R. Durrant, and Artem A. Bakulin. "The binding energy and dynamics of charge-transfer states in organic photovoltaics with low driving force for charge separation" *The Journal of Chemical Physics*, 150(10):104704, 2019. 23, 107

[62] Weiwei Li, Koen H. Hendriks, Alice Furlan, Martijn M. Wienk, and René A. J. Janssen. "High Quantum Efficiencies in Polymer Solar Cells at Energy Losses below 0.6 eV" *Journal of the American Chemical Society*, 137(6):2231–2234, 2015. 24

[63] Ke Gao, Lisheng Li, Tianqi Lai, Liangang Xiao, Yuan Huang, Fei Huang, Junbiao Peng, Yong Cao, Feng Liu, Thomas P. Russell, René A. J. Janssen, and Xiaobin Peng. "Deep Absorbing Porphyrin Small Molecule for High-Performance Organic Solar Cells with Very Low Energy Losses" *Journal of the American Chemical Society*, 137(23):7282–7285, 2015. 24

[64] Derya Baran, Thomas Kirchartz, Scot Wheeler, Stoichko Dimitrov, Maged Abdelsamie, Jeffrey Gorman, Raja S. Ashraf, Sarah Holliday, Andrew Wadsworth, Nicola Gasparini, Pascal Kaienburg, He Yan, Aram Amassian, Christoph J. Brabec, James R. Durrant, and Iain McCulloch. "Reduced voltage losses yield 10% efficient fullerene free organic solar cells with >1 V open circuit voltages" *Energy & Environmental Science*, 9(12):3783–3793, 2016. 24

[65] Yongxi Li, Xiaodong Liu, Fu-Peng Wu, Yi Zhou, Zuo-Quan Jiang, Bo Song, Yuxin Xia, Zhi-Guo Zhang, Feng Gao, Olle Inganäs, Yongfang Li, and Liang-Sheng Liao. "Non-fullerene acceptor with low energy loss and high

external quantum efficiency: towards high performance polymer solar cells" *Journal of Materials Chemistry A*, 4(16):5890–5897, 2016. 24

[66] Jing Liu, Shangshang Chen, Deping Qian, Bhoj Gautam, Guofang Yang, Jingbo Zhao, Jonas Bergqvist, Fengling Zhang, Wei Ma, Harald Ade, Olle Inganäs, Kenan Gundogdu, Feng Gao, and He Yan. "Fast charge separation in a non-fullerene organic solar cell with a small driving force" *Nature Energy*, 1(7):16089, 2016. 24, 51, 52, 59, 84

[67] Pei Cheng, Mingyu Zhang, Tsz-Ki Lau, Yao Wu, Boyu Jia, Jiayu Wang, Cenqi Yan, Meng Qin, Xinhui Lu, and Xiaowei Zhan. "Realizing Small Energy Loss of 0.55 eV, High Open-Circuit Voltage >1 V and High Efficiency >10% in Fullerene-Free Polymer Solar Cells via Energy Driver" *Advanced Materials*, 29(11):1605216, 2017. 24

[68] Mordechai Bixon, Joshua Jortner, and Jan W. Verhoeven. "Lifetimes for Radiative Charge Recombination in Donor-Acceptor Molecules" *Journal of the American Chemical Society*, 116(16):7349–7355, 1994. 24

[69] Ya-shih Huang, Sebastian Westenhoff, Igor Avilov, Paiboon Sreearunothai, Justin M. Hodgkiss, Caroline Deleener, Richard H. Friend, and David Beljonne. "Electronic structures of interfacial states formed at polymeric semiconductor heterojunctions" *Nature Materials*, 7(6):483–489, 2008. 24

[70] Koen Vandewal, Kristofer Tvingstedt, and Olle Inganäs. "Polarization anisotropy of charge transfer absorption and emission of aligned polymer:fullerene blend films" *Physical Review B*, 86(3):035212, 2012. 24

[71] Andreas P. Arndt, Marina Gerhard, Martin Koch, Uli Lemmer, and Ian A. Howard. "Identifying Charge-Transfer States in Polymer:Fullerene Heterojunctions by Their Emission Polarization Anisotropy" *The Journal of Physical Chemistry C*, 121(11):6357–6364, 2017. 24

[72] Flurin D. Eisner, Mohammed Azzouzi, Zhuping Fei, Xueyan Hou, Thomas D. Anthopoulos, T. John S. Dennis, Martin Heeney, and Jenny

Nelson. "Hybridization of Local Exciton and Charge-Transfer States Reduces Nonradiative Voltage Losses in Organic Solar Cells" *Journal of the American Chemical Society*, 141(15):6362–6374, 2019. 24

[73] Xian-Kai Chen, Veaceslav Coropceanu, and Jean-Luc Brédas. "Assessing the nature of the charge-transfer electronic states in organic solar cells" *Nature Communications*, 9(1):5295, 2018. 24

[74] Fabian Etzold, Ian A. Howard, Ralf Mauer, Michael Meister, Tae Dong Kim, Kwang Sup Lee, Nam Seob Baek, and Frédéric Laquai. "Ultrafast exciton dissociation followed by nongeminate charge recombination in PCDTBT:PCBM photovoltaic blends" *Journal of the American Chemical Society*, 133(24):9469–9479, 2011. 25

[75] M. Langevin. "Recombinaison et diffusion des ions gazeux" *Journal of Theoretical and Applied Physics*, 4(1):322–333, 1905. 25

[76] L. Jan Anton Koster, Martijn Kemerink, Martijn M. Wienk, Klará Maturová, and René A. J. Janssen. "Quantifying Bimolecular Recombination Losses in Organic Bulk Heterojunction Solar Cells" *Advanced Materials*, 23(14):1670–1674, 2011. 25, 89

[77] Christopher M. Proctor, Martijn Kuik, and Thuc-Quyen Nguyen. "Charge carrier recombination in organic solar cells" *Progress in Polymer Science*, 38(12):1941–1960, 2013. 25

[78] Girish Lakhwani, Akshay Rao, and Richard H. Friend. "Bimolecular Recombination in Organic Photovoltaics" *Annual Review of Physical Chemistry*, 65(1):557–581, 2014. 25

[79] Clemens Göhler, Alexander Wagenpfahl, and Carsten Deibel. "Nongeminate Recombination in Organic Solar Cells" *Advanced Electronic Materials*, 4(10):1700505, 2018. 25

[80] Veaceslav Coropceanu, Jean-Luc Brédas, and Shafigh Mehraeen. "Impact of Active Layer Morphology on Bimolecular Recombination Dynamics in

Organic Solar Cells" *The Journal of Physical Chemistry C*, 121(45):24954–24961, 2017. 25

[81] Maria Hilczer and Masanori Tachiya. "Unified Theory of Geminate and Bulk Electron-Hole Recombination in Organic Solar Cells" *The Journal of Physical Chemistry C*, 114(14):6808–6813, 2010. 25

[82] Akshay Rao, Philip C. Y. Chow, Simon Gélinas, Cody W. Schlenker, Chang-Zhi Li, Hin-Lap Yip, Alex K.-Y. Jen, David S. Ginger, and Richard H. Friend. "The role of spin in the kinetic control of recombination in organic photovoltaics" *Nature*, 500(7463):435–439, 2013. 26, 104

[83] Philip C. Y. Chow, Simon Gélinas, Akshay Rao, and Richard H. Friend. "Quantitative Bimolecular Recombination in Organic Photovoltaics through Triplet Exciton Formation" *Journal of the American Chemical Society*, 136(9):3424–3429, 2014. 26, 104

[84] Johannes Benduhn, Fortunato Piersimoni, Giacomo Londi, Anton Kirch, Johannes Widmer, Christian Koerner, David Beljonne, Dieter Neher, Donato Spoltore, and Koen Vandewal. "Impact of Triplet Excited States on the Open-Circuit Voltage of Organic Solar Cells" *Advanced Energy Materials*, 8(21):1800451, 2018. 26, 89

[85] Johannes Stark. "Beobachtungen über den Effekt des elektrischen Feldes auf Spektrallinien. I. Quereffekt" *Annalen der Physik*, 348(7):965–982, 1914. 29

[86] Árpad Horváth, Heinz Bässler, and Gerhard Weiser. "Electroabsorption in Conjugated Polymers" *Physica Status Solidi (b)*, 173(2):755–764, 1992. 29

[87] Thomas M. Brown. *Electroabsorption Investigations of Polymer Light-Emitting Diodes with Efficient Electrodes*. Ph.D. thesis, University of Cambridge, 2001. 30

[88] Juan Cabanillas-Gonzalez, Giulia Grancini, and Guglielmo Lanzani. "Pump-Probe Spectroscopy in Organic Semiconductors: Monitoring Fundamental Processes of Relevance in Optoelectronics" *Advanced Materials*, 23(46):5468–5485, 2011. 31

[89] Sergey A. Kovalenko, Alexander L. Dobryakov, Jürgen Ruthmann, and Nikolaus P. Ernsting. "Femtosecond spectroscopy of condensed phases with chirped supercontinuum probing" *Physical Review A - Atomic, Molecular, and Optical Physics*, 59(3):2369–2384, 1999. 31

[90] Dario Polli, Daniele Brida, Shaul Mukamel, Guglielmo Lanzani, and Giulio Cerullo. "Effective temporal resolution in pump-probe spectroscopy with strongly chirped pulses" *Physical Review A*, 82(5):053809, 2010. 31

[91] Robert W. Boyd. *Nonlinear Optics*. Academic Press, 2007. 34

[92] Dezhi Tan, Kaniyarakkal N. Sharafudeen, Yuanzheng Yue, and Jianrong Qiu. "Femtosecond laser induced phenomena in transparent solid materials: Fundamentals and applications" *Progress in Materials Science*, 76(March 2016):154–228, 2016. 34

[93] Giulio Cerullo, Mauro Nisoli, Salvatore Stagira, and Sandro De Silvestri. "Sub-8-fs pulses from an ultrabroadband optical parametric amplifier in the visible." *Optics letters*, 23(16):1283–1285, 1998. 35

[94] Daniele Brida, Cristian Manzoni, Giovanni Cirmi, Marco Marangoni, Stefano Bonora, Paolo Villoresi, Sandro De Silvestri, and Giulio Cerullo. "Few-optical-cycle pulses tunable from the visible to the mid-infrared by optical parametric amplifiers" *Journal of Optics*, 12(1):013001, 2010. 35

[95] Giulio Cerullo and Sandro De Silvestri. "Ultrafast optical parametric amplifiers" *Review of Scientific Instruments*, 74(1):1, 2003. 35

[96] Matz Liebel, Christoph Schnedermann, and Philipp Kukura. "Sub-10-fs pulses tunable from 480 to 980 nm from a NOPA pumped by an Yb:KGW source" *Opt. Lett.*, 39(14):4112, 2014. 35

[97] Maximilian Bradler and Eberhard Riedle. "Sub-20 fs $\mu$J-energy pulses tunable down to the near-UV from a 1 MHz Yb-fiber laser system." *Optics letters*, 39(9):2588–91, 2014. 35

[98] Andreas C. Jakowetz, Marcus L. Böhm, Aditya Sadhanala, Sven Huettner, Akshay Rao, and Richard H. Friend. "Visualizing excitations at buried heterojunctions in organic semiconductor blends" *Nature Materials*, 16(5):551–557, 2017. 42, 57, 69, 80

[99] Andrius Devižis, Jelissa De Jonghe-Risse, Roland Hany, Frank Nüesch, Sandra Jenatsch, Vidmantas Gulbinas, and Jacques-E. Moser. "Dissociation of Charge Transfer States and Carrier Separation in Bilayer Organic Solar Cells: A Time-Resolved Electroabsorption Spectroscopy Study" *Journal of the American Chemical Society*, 137(25):8192–8198, 2015. 42, 57

[100] Jiye Lee, Priya Jadhav, Philip D. Reusswig, Shane R. Yost, Nicholas J. Thompson, Daniel N. Congreve, Eric Hontz, Troy Van Voorhis, and Marc A. Baldo. "Singlet Exciton Fission Photovoltaics" *Accounts of Chemical Research*, 46(6):1300–1311, 2013. 42, 57

[101] Simon Gélinas. *Spectroscopic Study of Charge-Separation Dynamics in $\pi$-Conjugated Systems*. Ph.D. thesis, University of Cambridge, 2013. 43

[102] M. Srinivas and L. M. Patnaik. "Adaptive Probabilities of Crossover and Mutation in Genetic Algorithms" *IEEE Transactions on Systems, Man and Cybernetics*, 24(4):656–667, 1994. 45

[103] Philip C. Y. Chow, Ture F. Hinrichsen, Christopher C. S. Chan, David Paleček, Alexander Gillett, Shangshang Chen, Xinhui Zou, Chao Ma, Kam Sing Wong, Richard H. Friend, He Yan, and Akshay Rao. "Endothermic charge separation in efficient non-fullerene organic solar cells" *Under review*, 2019. 50, 68

[104] Jianquan Zhang, Yunke Li, Jiachen Huang, Huawei Hu, Guangye Zhang, Tingxuan Ma, Philip C. Y. Chow, Harald Ade, Ding Pan, and He Yan. "Ring-Fusion of Perylene Diimide Acceptor Enabling Efficient Nonfullerene

Organic Solar Cells with a Small Voltage Loss" *Journal of the American Chemical Society*, 139(45):16092–16095, 2017. 53

[105] Jing Liu, Lik-Kuen Ma, Fu Kit Sheong, Lin Zhang, Huawei Hu, Jing-Xuan Zhang, Jianquan Zhang, Zhengke Li, Chao Ma, Xu Han, Ding Pan, Harald Ade, Wei Ma, and He Yan. "Carboxylate substitution position influencing polymer properties and enabling non-fullerene organic solar cells with high open circuit voltage and low voltage loss" *Journal of Materials Chemistry A*, 6(35):16874–16881, 2018. 53

[106] Shangshang Chen, Yuming Wang, Lin Zhang, Jingbo Zhao, Yuzhong Chen, Danlei Zhu, Huatong Yao, Guangye Zhang, Wei Ma, Richard H. Friend, Philip C. Y. Chow, Feng Gao, and He Yan. "Efficient Nonfullerene Organic Solar Cells with Small Driving Forces for Both Hole and Electron Transfer" *Advanced Materials*, 30(45):1804215, 2018. 53

[107] Sebastian Albert-Seifried and Richard H. Friend. "Measurement of thermal modulation of optical absorption in pump-probe spectroscopy of semiconducting polymers" *Applied Physics Letters*, 98(22):98–101, 2011. 58

[108] Artem A. Bakulin, Akshay Rao, Vlad G. Pavelyev, Paul H. M. van Loosdrecht, Maxim S. Pshenichnikov, Dorota Niedzialek, Jerome Cornil, David Beljonne, and Richard H. Friend. "The Role of Driving Energy and Delocalized States for Charge Separation in Organic Semiconductors" *Science*, 335(6074):1340–1344, 2012. 60, 80

[109] Jean-Luc Brédas, David Beljonne, Veaceslav Coropceanu, and Jérôme Cornil. "Charge-Transfer and Energy-Transfer Processes in $\pi$-Conjugated Oligomers and Polymers: A Molecular Picture" *Chemical Reviews*, 104(11):4971–5003, 2004. 60

[110] Feng Gao, Wolfgang Tress, Jianpu Wang, and Olle Inganäs. "Temperature Dependence of Charge Carrier Generation in Organic Photovoltaics" *Physical Review Letters*, 114(12):128701, 2015. 62, 63, 127

[111] Steffen Tscheuschner, Heinz Bässler, Katja Huber, and Anna Köhler. "A Combined Theoretical and Experimental Study of Dissociation of Charge Transfer States at the Donor–Acceptor Interface of Organic Solar Cells" *The Journal of Physical Chemistry B*, 119(32):10359–10371, 2015. 63

[112] Hans H. P. Gommans, Martijn Kemerink, Jan M. Kramer, and Rene A. J. Janssen. "Field and temperature dependence of the photocurrent in polymer/fullerene bulk heterojunction solar cells" *Applied Physics Letters*, 87(12):122104, 2005. 63, 127

[113] Bernd Ebenhoch, Stuart A. J. Thomson, Kristijonas Genevičius, Gytis Juška, and Ifor D.W. Samuel. "Charge carrier mobility of the organic photovoltaic materials PTB7 and PC71BM and its influence on device performance" *Organic Electronics*, 22:62–68, 2015. 63, 127

[114] Philip C. Y. Chow, Sam L. Bayliss, Girish Lakhwani, Neil C. Greenham, and Richard H. Friend. "In Situ Optical Measurement of Charge Transport Dynamics in Organic Photovoltaics" *Nano Letters*, 15(2):931–935, 2015. 64

[115] Simon Gélinas, Olivier Paré-Labrosse, Colin-Nadeau Brosseau, Sebastian Albert-Seifried, Christopher R. McNeill, Kiril R. Kirov, Ian A. Howard, Richard Leonelli, Richard H. Friend, and Carlos Silva. "The Binding Energy of Charge-Transfer Excitons Localized at Polymeric Semiconductor Heterojunctions" *The Journal of Physical Chemistry C*, 115(14):7114–7119, 2011. 65

[116] Mark E. Ziffer, Sae Byeok Jo, Hongliang Zhong, Long Ye, Hongbin Liu, Francis Lin, Jie Zhang, Xiaosong Li, Harald W. Ade, Alex K.-Y. Jen, and David S. Ginger. "Long-Lived, Non-Geminate, Radiative Recombination of Photogenerated Charges in a Polymer/Small-Molecule Acceptor Photovoltaic Blend" *Journal of the American Chemical Society*, 140(31):9996–10008, 2018. 65

[117] Ignacio B. Martini, Alex D. Smith, and Benjamin J. Schwartz. "Exciton-exciton annihilation and the production of interchain species in conjugated

polymer films: Comparing the ultrafast stimulated emission and photoluminescence dynamics of MEH-PPV" *Physical Review B*, 69(3):035204, 2004. 73

[118] Sascha Ullbrich, Johannes Benduhn, Xiangkun Jia, Vasileios C. Nikolis, Kristofer Tvingstedt, Fortunato Piersimoni, Steffen Roland, Yuan Liu, Jinhan Wu, Axel Fischer, Dieter Neher, Sebastian Reineke, Donato Spoltore, and Koen Vandewal. "Emissive and charge-generating donor–acceptor interfaces for organic optoelectronics with low voltage losses" *Nature Materials*, page 1, 2019. 84

[119] Xian-Kai Chen and Jean-Luc Brédas. "Voltage Losses in Organic Solar Cells: Understanding the Contributions of Intramolecular Vibrations to Nonradiative Recombinations" *Advanced Energy Materials*, 8(9):1702227, 2018. 89

[120] Guangye Zhang, Jingbo Zhao, Philip C. Y. Chow, Kui Jiang, Jianquan Zhang, Zonglong Zhu, Jie Zhang, Fei Huang, and He Yan. "Nonfullerene Acceptor Molecules for Bulk Heterojunction Organic Solar Cells" *Chemical Reviews*, 118(7):3447–3507, 2018. 89

[121] Ture F. Hinrichsen, Deping Qian, Yuming Wang, Alexandre Cheminal, Feng Gao, and Akshay Rao. "Trap-assisted electron recombination in an efficient non-fullerene organic solar cell with low voltage loss" *In preparation*, 2019. 91

[122] S. Matthew Menke, Aditya Sadhanala, Mark Nikolka, Niva A. Ran, Mahesh Kumar Ravva, Safwat Abdel-Azeim, Hannah L. Stern, Ming Wang, Henning Sirringhaus, Thuc-Quyen Nguyen, Jean-Luc Brédas, Guillermo C. Bazan, and Richard H. Friend. "Limits for Recombination in a Low Energy Loss Organic Heterojunction" *ACS Nano*, 10(12):10736–10744, 2016. 104

[123] Omar M. Awartani, Bhoj Gautam, Wenchao Zhao, Robert Younts, Jianhui Hou, Kenan Gundogdu, and Harald Ade. "Polymer non-fullerene solar cells of vastly different efficiencies for minor side-chain modification: impact

of charge transfer, carrier lifetime, morphology and mobility" *Journal of Materials Chemistry A*, 6(26):12484–12492, 2018. 104, 105

[124] Dar'ya Davydova, Alejandro de la Cadena, Stefan Demmler, Jan Rothhardt, Jens Limpert, Torbjörn Pascher, Denis Akimov, and Benjamin Dietzek. "Ultrafast transient absorption microscopy: Study of excited state dynamics in PtOEP crystals" *Chemical Physics*, 464:69–77, 2016. 104

[125] Marc A. Baldo and Stephen R. Forrest. "Transient analysis of organic electrophosphorescence: I. Transient analysis of triplet energy transfer" *Physical Review B*, 62(16):10958–10966, 2000. 104

[126] Stoichko D. Dimitrov, Bob C. Schroeder, Christian B. Nielsen, Hugo Bronstein, Zhuping Fei, Iain McCulloch, Martin Heeney, and James R. Durrant. "Singlet exciton lifetimes in conjugated polymer films for organic solar cells" *Polymers*, 8(1), 2016. 105

[127] Guanqing Zhou, Hong Ding, Lei Zhu, Chaoqun Qiu, Ming Zhang, Tianyu Hao, Wei Feng, Yongming Zhang, Haiming Zhu, and Feng Liu. "Photophysics, morphology and device performances correlation on non-fullerene acceptor based binary and ternary solar cells" *Journal of Energy Chemistry*, 47:180–187, 2020. 105

[128] Omar M. Awartani, Bhoj Gautam, Wenchao Zhao, Robert Younts, Jianhui Hou, Kenan Gundogdu, and Harald Ade. "Polymer non-fullerene solar cells of vastly different efficiencies for minor side-chain modification: impact of charge transfer, carrier lifetime, morphology and mobility" *Journal of Materials Chemistry A*, 6(26):12484–12492, 2018. 106, 118

[129] Yun Liu, Lijian Zuo, Xueliang Shi, Alex K.-Y. Jen, and David S. Ginger. "Unexpectedly Slow Yet Efficient Picosecond to Nanosecond Photoinduced Hole-Transfer Occurs in a Polymer/Nonfullerene Acceptor Organic Photovoltaic Blend" *ACS Energy Letters*, 3(10):2396–2403, 2018. 118

[130] Junqing Shi, Anna Isakova, Abasi Abudulimu, Marius van den Berg, Oh Kyu Kwon, Alfred J. Meixner, Soo Young Park, Dai Zhang, Johannes Gierschner, and Larry Lüer. "Designing high performance all-small-molecule solar cells with non-fullerene acceptors: comprehensive studies on photoexcitation dynamics and charge separation kinetics" *Energy & Environmental Science*, 11(1):211–220, 2018. 118

[131] Curt H. Liebert and Russel E. Jr. Hart. "Solar-cell performance at low temperatures and simulated solar intensities" *NASA Technical Notes*, D-7855, 1969. 127